Investigation of Synthetic Jet Flow Control Parameters for Laminar Boundary Layer Separation Mitigation

by

Mark Feero

A thesis submitted in conformity with the requirements
for the degree of Doctor of Philosophy
Graduate Department of the Institute for Aerospace Studies
University of Toronto

Abstract

Investigation of Synthetic Jet Flow Control Parameters for Laminar Boundary Layer Separation Mitigation

Mark Feero
Doctor of Philosophy
Graduate Department of the Institute for Aerospace Studies
University of Toronto
2017

An experimental study was performed to elucidate the effects of forcing parameters on the mitigation of boundary layer separation on an airfoil at low Reynolds number. Post-stall flow at a Reynolds number of 100,000 and angle-of-attack 12 degrees on a NACA 0025 airfoil served as the baseline for control with a synthetic jet actuator. This baseline flow is characterized by two dominant instabilities: the large scale vortex shedding in the wake of the airfoil, and the roll-up of vortices in the separated shear layer. The forcing parameters that were investigated were the blowing ratio, excitation frequency, and the chordwise forcing location.

The results concerning the effects on aerodynamic performance showed that for both drag reduction and lift increase, once a particular blowing ratio was met the benefits of control saturated. Positioning the slot at the most upstream location resulted in the lowest threshold blowing ratio (defined as being the blowing ratio required for fully attached flow) and produced the largest lift-to-drag ratios. A monotonic increase in threshold blowing ratio and decrease in lift-to-drag was observed as the slot location moved downstream. It was also found that while forcing at a frequency corresponding to the wake instability led to maximum lift increase, forcing in the range of the separated shear layer instability led to maximum drag reduction. High-frequency forcing, where the time scales of control are much larger than those of the flow, was found to be least effective for improving performance.

The saturation in control benefits was generally associated with the mean flow over the airfoil being fully attached, while prior to this the initial lift increase and drag reduction was due to the formation of a laminar separation bubble. The controlled flow dynamics revealed the presence of large vortices passing over the suction surface and highly unsteady flow when forcing at the wake instability frequency, whereas forcing in the range of the shear layer instability led to the production of a larger number of much smaller vortices. Extraction of coherent and turbulent velocity fluctuations showed that the controlled flow was steady in time with high-frequency forcing.

Acknowledgements

I am extremely grateful for the love and support of my parents, Mary and Peter Feero. I have no doubt that my drive to complete graduate school was a direct result of their encouragement in my younger years to strive for more, and their unwillingness to accept any less. Although I may not of understood it at the time, I have come to recognize that the work ethic they instilled in me has been fundamental to this achievement.

I would like to thank my supervisors, Professor Philippe Lavoie and Professor Pierre Sullivan, for their guidance and dedication to this project. It has been a pleasure learning from each of them and I am confident that the skills I have gained through their supervision will be invaluable in future endeavours. I would also like to acknowledge Prof. Zingg and Prof. Ekmekci who served as my Doctoral Examination Committee and provided insightful commentary on this work.

I look back with great fondness on my time spent as part of the FCET lab and the friends I have made along the way. Over the past five years, I have been happy to watch Nicole Houser, Rafik Chekiri, Leon Li, David Sutton and Derrick Chow complete their degrees and move on to new ventures, yet miss their presence in the group. I am incredibly thankful to have spent several years with Dr. Heather Clark and Dr. Jason Hearst, who consistently inspired me and shared their wealth of knowledge with me. I am grateful not only for the example they set as experimentalists, but also for their friendship and the many laughs shared to this day. I am thankful to Dr. Zachary Berger for passing along his knowledge of PIV and aiding in my setup. I am also appreciative of the many thought provoking and helpful discussions with Prof. Serhiy Yarusevych over the years, including his recommendation of a prospective postdoc position.

The financial support provided by the Natural Sciences and Engineering Research Council of Canada, the Ontario Government, Lyon Sachs, and the University of Toronto is gratefully acknowledged.

Contents

List of Figures

List of Tables

Nomenclature

Roman symbols

a	speed of sound in air
b	model spanwise length
c	chord length
C_{B}	blowing ratio
C_{B}^{*}	threshold blowing ratio
C_D	section drag coefficient
C_L	section lift coefficient
C_p	pressure coefficient
d	synthetic jet slot width
E	control signal voltage amplitude
f	frequency
f^+	normalized frequency ($\equiv fc/U_\infty$)
f_{c}	control signal carrier frequency
f_{d}	piezoelectric diaphragm natural frequency
f_{e}	excitation frequency
f_{H}	Helmholtz frequency
f_{m}	control signal modulation frequency
f_{sl}	shear layer frequency
f_{w}	wake frequency
F^+	reduced forcing frequency ($\equiv f_{\mathrm{e}}c/U_\infty$)
h	synthetic jet slot height
H	transfer function
L	synthetic jet slot length
n	number of cycles
N	number of statistically independent samples
N_{r}	number of calibration records
p	static pressure
p_{c}	pressure measured by DPT during calibration
p_{r}	calibration reference pressure
p_∞	mean freestream static pressure
P	power spectral density or cross-spectral density (differentiated by subscripts)
q_∞	mean freestream dynamic pressure

Re_c	chord based Reynolds number ($\equiv U_\infty c/\nu$)
S	swirl strength
S/N	signal-to-noise ratio
t	time
T	total signal length
T_I	integral time scale
u, v	streamwise and transverse components of fluctuating velocity
u_j	synthetic jet axial velocity
$u_\mathrm{s}, u_\mathrm{n}$	wall-tangential and wall-normal components of fluctuating velocity
u_t	fluctuating total velocity as measured by a single-wire hot-wire
U, V	steamwise and transverse components of mean velocity
$U_\mathrm{s}, U_\mathrm{n}$	wall-tangential and wall-normal components of mean velocity
U_e	edge velocity
$\overline{U_\mathrm{j}}$	time-averaged synthetic jet expulsion velocity
U_∞	freestream velocity
U_T	mean velocity magnitude
VR	modulation velocity ratio
$\forall$	synthetic jet cavity volume
x	chordwise coordinate originating at the leading edge
x_j	chordwise location of the synthetic jet slot
x_j^*	chordwise slot location relative to separation ($\equiv (x_\mathrm{j} - x_\mathrm{s})/c$)
x_s	mean chordwise separation point
X, Y, Z	streamwise, transverse and spanwise global coordinates
y	local wall-normal coordinate
y_d	dividing streamline wall-normal location

Greek symbols

α	angle-of-attack
β	local airfoil surface angle in the global frame of reference
χ_1, χ_2, χ_3	fitting parameters for the Dovgal et al. [23] boundary layer curve fit
δ	99% boundary layer thickness
δ^*	displacement thickness
ϵ	transfer function random error
θ	momentum thickness
ν	kinematic viscosity
ϕ	phase angle relative to input signal

Φ	phase offset between synthetic jet velocity and input signal
ρ	density
σ	standard deviation of a given quantity
τ	control signal period
γ	spectral coherence
ω_Z	spanwise vorticity
ξ	synthetic jet slot major axis coordinate

Other symbols and operators

$\cdot'$	turbulent fluctuation
$\tilde{\cdot}$	coherent fluctuation
$\bar{\cdot}$	time-average
$\langle\cdot\rangle$	phase-average
Δ	difference
$\lvert\cdot\rvert$	magnitude (absolute value)
$\angle$	phase angle between real and imaginary parts

Subscripts

ave	spatial average
HW	hot-wire
l	airfoil lower (pressure) surface
max	maximum
o	baseline
PIV	particle image velocimetry
rms	root-mean-square
tot	instantaneous
u	airfoil upper (suction) surface

Chapter 1

Introduction

1.1 Low Reynolds number airfoils

The study of flow over airfoils is a fundamental topic in fluid mechanics and aerodynamics, as this geometry forms the cross-section of lifting bodies used in applications ranging from aircraft to power generating turbines. Proper performance of the airfoil is necessary for the lifting body to function efficiently. The relevant scaling parameter for airfoils is the chord based Reynolds number,

$$Re_c = \frac{U_\infty c}{\nu}, \tag{1.1}$$

where U_∞ is freestream velocity, c is the airfoil chord length, ν is the kinematic viscosity of the fluid in which the airfoil is operating. Aerodynamic performance as characterized by the lift and drag forces, and the lift-to-drag ratio, decreases at low Reynolds number due to the relatively large impact of viscous effects. According to Lissaman [55], the 'low' Reynolds number regime is considered as $Re_c < 1\times10^6$, and in particular $Re_c < 5\times10^5$ as pointed out by Fitzgerald and Mueller [33]. A lower limit exists at $Re_c = 100$, below which viscosity dominates and the airfoil is unlikely to produce lift [55]. Low Reynolds number flow over an airfoil differs from high Reynolds number due to the fact that the boundary layer can remain laminar into the region of adverse pressure gradient, which causes the boundary layer to separate. Depending on where transition occurs in the separated shear layer, there are two possible outcomes: the flow reattaches at some downstream location in the time-averaged sense, a laminar separation bubble (LSB), or the flow remains separated, referred to as stall. Compared with high Reynolds number flow, stall can occur at low angles-of-attack, α [85; 12]. Stall causes a significant decrease in aerodynamic performance, both in terms of lift reduction and drag enlargement. Aerodynamic forces

at low Reynolds number can also experience substantial hysteresis as the angle-of-attack increases above and then returns below the stall angle. Laminar separation bubbles can also be detrimental to aerodynamic performance, even when the bubble is relatively short and spans a small percentage of the airfoil chord [33]. Reynolds number and angle-of-attack have a similar, but inverse effect on the state of the flow, where decreasing Re_c or increasing α reduces the ability of the laminar boundary layer to withstand the adverse pressure gradient. Understanding the behaviour of this flow at low Reynolds number is important as there are an increasing number of relevant applications, particular with recent advances in unmanned aerial vehicles and micro air vehicles. Other useful applications at $Re_c < 10^6$ include human powered aircraft, wind turbine blades and low-speed aircraft. Considerable research has been performed over the last several decades to measure aerodynamic forces [19; 57; 60] and characterize the development of boundary layers with separation bubbles [15; 63; 85].

The stalled flow at low Re_c is of particular interest due its occurrence at relatively low α, and the dramatic reduction in aerodynamic performance. The post-stall separated flow is dominated by two instabilities: the local instability of the separated shear layer, and the global instability that causes large scale vortex shedding in the wake [81]. An excellent visualization of the coherent structures resulting from these two instabilities was performed by Yarusevych et al. [85], Figure 1.1. Large scale von Karman like vortex shedding is observed in the wake, whereas the roll-up of smaller scale vortices can be seen in the separated shear layer (Figure 1.1b). If a normalized frequency $f^+ = fc/U_\infty$ (where f is frequency) is considered, the shear layer layer and wake instabilities correspond to $f^+_{\mathrm{sl}} = \mathcal{O}(10)$ [13; 15] and $f^+_{\mathrm{w}} \approx 1$ [16; 84]. The order of magnitude difference in the frequency of these instabilities follows from conventional scaling arguments, where the characteristic length scale in the shear layer near separation is an order of magnitude smaller than that of the wake [73]. The transition to turbulence in the separated shear layer for stalled flow follows the same process as in the case of a LSB, which has received considerable attention in the literature (e.g. [23; 13]). It has been shown by authors such as Yarusevych et al. [84], Hu and Yang [48] and Burgmann and Schröder [18] that the transition process is governed by the inviscid Kelvin-Helmholtz instability. This causes the spatial amplification of a band of unstable frequencies in the shear layer downstream of separation, where velocity fluctuations grow logarithmically. This amplification over a range of frequencies with a central frequency at $f^+_{\mathrm{sl}} = \mathcal{O}(10)$ was observed in both velocity and wall pressure spectra for flows with LSBs and stalled flows at $Re_c = 100,000$ by Boutilier and Yarusevych [13].

As discussed by Wu et al. [81], the high receptivity of the leading edge separated

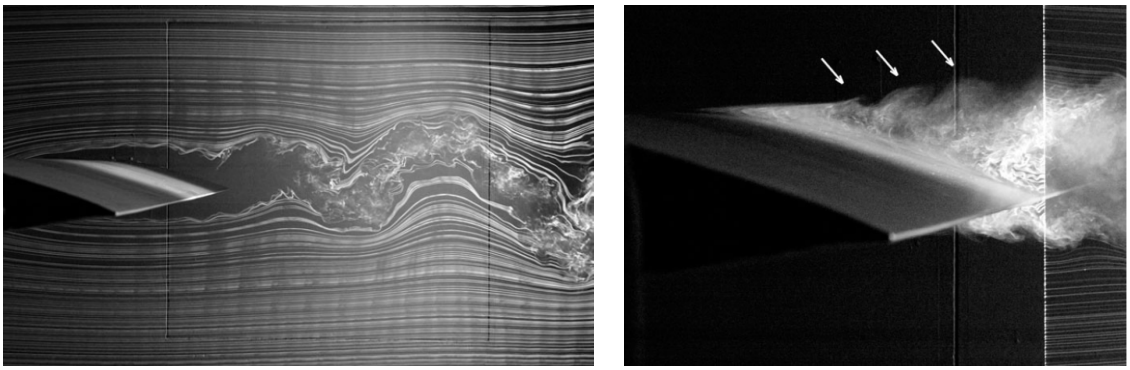

(a) (b)

Figure 1.1: Smoke-wire flow visualization of the flow at $Re_c = 55,000$ and $\alpha = 5°$ on a NACA 0025 airfoil by Yarusevych et al. [85].

shear layer, and the non-linear coupling between the wake and shear layer instabilities natural to the baseline flow suggests that a favourable method for controlling the flow and improving performance is one that is unsteady. The forthcoming section will introduce a method for imposing unsteady control, and the parameters of importance for this type of forcing.

1.2 Zero-net-mass-flux actuation: the synthetic jet

Unsteady forcing implies that the control strategy is classified as *active*. Active flow control differs from *passive* control in that energy is added to the flow and there are operational characteristics that can be adjusted [20]. Passive control typically refers to static geometrical changes, such as roughness strips, or vortex generating tabs. The passive devices can be beneficial, but they also inherently add parasitic drag, and are present even when they are not necessarily required. Active devices can be designed in such a way that they do not add drag, and they can be controlled to provide forcing only when needed.

Within active control, fluidic devices can be considered as a category of actuator types. The most basic examples are steady blowing and suction, where in the former an external fluid is injected at the boundary layer, while in the latter the working fluid is removed at the boundary layer. Another common type of fluidic control is zero-net-mass-flux (ZNMF) actuation, and this is typically accomplished using a device known as a synthetic jet. A synthetic jet is able to transfer linear momentum without adding or removing mass from the flow (i.e. ZNMF) by utilizing the working fluid [71]. Since the

momentum flux at the exit plane is proportional to the axial velocity squared, both the ingestion and expulsion halves of the cycle contribute positively to the momentum flux. A basic synthetic jet configuration is made up of a cavity with one or more oscillating walls and a slot or orifice exposed to the working fluid (Figure 1.2). In the context of flow control, the slot/orifice would be located at the wall where control is desired. Oscillation of the cavity wall(s) creates volume fluctuations, and in turn pressure fluctuations within the cavity. This unsteady pressure causes the working fluid to be alternately ingested and expelled from the cavity. In quiescent conditions, a vortex ring/pair at the orifice/slot edge(s) forms, as shown by the flow visualization in Figure 1.2. Common examples of drivers used to create the volume fluctuations inside the cavity include piston/cylinder arrangements, loudspeakers, and piezoelectric diaphragms. Compared with other fluidic actuators such as unsteady blowing or suction, the distinct advantage of the synthetic jet is that it requires no external fluid source or sink. This is advantageous for flow control applications where the actuator is installed within the aerodynamic body, as no plumbing must be supplied to the synthetic jet.

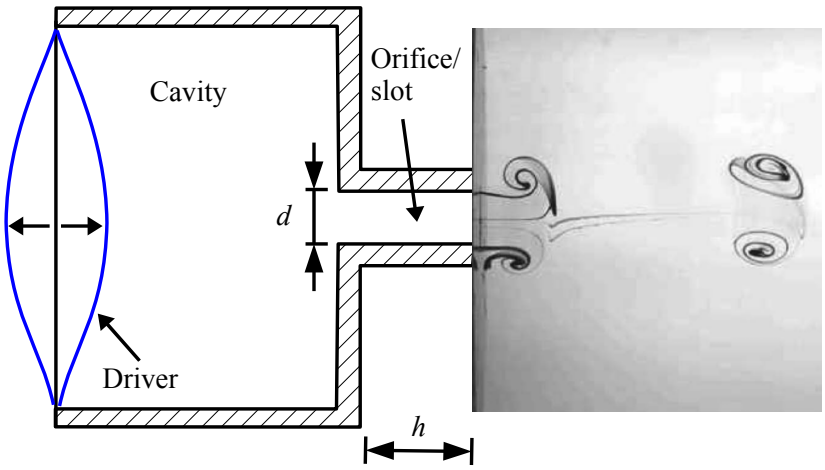

Figure 1.2: Cross-sectional schematic of a basic synthetic jet actuator. The flow visualization of laminar synthetic jet flow is adapted from Shuster and Smith [70].

The ideal velocity profile at a given time at the orifice/slot exit plane is spatially uniform (i.e. a 'top-hat') shape. If the velocity profiles during the ingestion and expulsion halves of the cycle are symmetric, the time-averaged velocity at any location must be zero. Thus, the time-averaged synthetic jet velocity does not provide a useful velocity scale. A velocity scale that is useful in the context of control experiments is defined as:

$$\overline{U_{\mathrm{j}}} = \frac{1}{\tau/2} \int_0^{\tau/2} \langle u_{\mathrm{j}} \rangle \, \mathrm{d}t, \tag{1.2}$$

where τ is the period of the excitation cycle and $\langle u_j \rangle$ is the phase-averaged jet velocity (see Section 2.8 for the definition of phase averaging). This expression implies that expulsion occurs over $0 \leq t \leq 0.5\tau$ and the expulsion velocity profile has a top-hat shape. This definition of a mean velocity over the expulsion half of the cycle is similar to the definition of a mean expulsion momentum used in the seminal work of Amitay et al. [3]. Often due to time or experimental constraints, a top-hat velocity profile is assumed and $\overline{U_j}$ is obtained from the velocity at the center of the exit plane (e.g., [42; 16]).

A synthetic jet actuator represents a coupled electromechanical-acoustic system, where electrical input to a driver creates mechanical motion, which creates pressure fluctuations inside the cavity. An important feature of any actuator is the frequency response that dictates the output quantity of interest to a sinusoidal input signal. In the case of a synthetic jet, the frequency response of the jet velocity is controlled by the cavity/orifice geometry, fluid properties, and driver properties [45]. Piezoelectric diaphragms, which behave smilarily to a voice coil, are a common driver used for synthetic jets in flow control applications as they are thin and do not occupy a large volume. Gallas et al. [36] used lumped element modelling to show that a piezoelectric driven synthetic jet behaves as a fourth-order coupled oscillator, with one oscillator being the cavity operating as a Helmholtz resonator, and the other is the piezoelectric diaphragm itself. This system therefore has two resonant frequencies, which are bounded by the Helmholtz frequency of the cavity, and the natural frequency of the piezo. Depending on the proximity of the Helmholtz and diaphragm frequencies, which is a measure of the system 'coupling', the response of synthetic jet velocity may have two distinct resonant peaks (low coupling ratio), or a single merged peak (high coupling ratio). Gallas et al. [36] demonstrated both numerically with the lumped element model and experimentally that a synthetic jet with high coupling ratio results in a single resonant peak in $\overline{U_j}$ that is larger in magnitude than a case with low coupling ratio. The same dependence of the jet velocity resonant frequencies on the coupling between the two oscillators was also shown by de Luca et al. [22]. The fact that the SJA velocity frequency response is dominated by strong resonant peaks represents a shortcoming of this actuator, as an ideal actuator would have a flat response over a large frequency range. The bandwidth over which acceptable velocity magnitudes can be achieved is often limited to frequencies near resonance, which may not be ideal for a flow control application. However, this shortcoming may be alleviated by modulating the harmonic control signal (e.g. [58; 39; 65]).

1.3 Periodic control of low Reynolds number airfoils

The unwanted effects of laminar boundary layer separation can be mitigated by implementing active control strategies to promote flow reattachment. Over many years, researchers have demonstrated the use of periodic excitation applied locally at the surface can achieve flow reattachment and improve aerodynamic performance (e.g., [16; 5; 42]). The effectiveness of control in mitigating boundary separation depends on a number of parameters related both to the flow itself and the control input. A review of the literature by Greenblatt and Wygnanski [44] highlighted the following important control parameters for a 2D airfoil: excitation frequency, amplitude, streamwise location and slot/orifice orientation. The excitation frequency is often presented non-dimensionalized as a reduced frequency,

$$F^+ = \frac{f_e c}{U_\infty}, \tag{1.3}$$

where f_e is the the excitation frequency. In some studies F^+ is defined using the length of the separated region rather than c, however these length scales are nearly equivalent for leading edge separation on an airfoil, and here c will be used as it permits easier comparison between different studies. In a 2D configuration, the amplitude of a SJA may be quantified by the blowing ratio,

$$C_B = \frac{\overline{U_j}}{U_\infty}. \tag{1.4}$$

The blowing ratio C_B will be used to quantify the excitation amplitude in this study, however it can also be related to the momentum coefficient defined by Amitay et al. [3], which uses the time-averaged *momentum* during the expulsion portion of the cycle. In a 3D control configuration, the momentum coefficient may be more appropriate as it incorporates the ratio of actuator slot/orifice area to a reference area of the aerodynamic body. Unfortunately, there is presently no agreed upon standard for which parameter more appropriately describes excitation amplitude. Blowing ratio has been used in a number of studies in the literature rather than the momentum coefficient to quantity the excitation amplitude where the control is essentially 2D (i.e. 2D baseline flow and control applied over the whole span) [9; 10; 64; 76; 81].

Greenblatt and Wygnanski [44] concluded that the majority of investigations using periodic excitation on airfoils described an optimum dimensionless frequency of $0.3 < F^+ < 4$. Excitation of the separated shear layer at frequencies near $F^+ = 1$ has proven to be effective by exploiting the global wake instability at $f_w^+ \approx 1$. However, flow

reattachment and performance improvement on a stalled airfoil for both $F^+ = \mathcal{O}(1)$ and for excitation frequencies an order of magnitude larger, $F^+ = \mathcal{O}(10)$, has been demonstrated [26; 38]. For F^+ that is $\mathcal{O}(1)$, large vortical structures are formed and convect downstream near the airfoil surface, leading to unsteady reattachment and time-periodic variations in circulation [2; 1]. More recently, Buchmann et al. [16] showed that the fully reattached flow at $Re_c = 30,000$ due to forcing at $F^+ = 1.3$ was the result of coherent vortices convecting over the surface and causing a net entrainment of high momentum fluid towards the wall. Control at $F^+ \geq \mathcal{O}(10)$ may be considered essentially time invariant relative to the flow if F^+ is much larger than f^+_{sl}. Amitay et al. [3] described this type of 'high-frequency' control as a local modification of the apparent aerodynamic shape of the flow surface, thereby changing the pressure gradient and suppressing flow separation. However, in the work by Amitay and Glezer [2] where the effect of control over a wide range of F^+ was investigated, the range of frequencies associated with f^+_{sl} was not identified and thus it was unclear when control may have been targeting this instability. A recent study by Yarusevych and Kotsonis [83] considered the effect of control for $2 \leq F^+ \leq 10$ and $F^+ = 100$ on a LSB occurring at $Re_c = 1.3 \times 10^5$. The results showed that the most significant effect on the mean reduction in LSB size was achieved for $F^+ = 6$, which corresponded to the most amplified disturbances of the separated shear layer. Similarily, Bernardini et al. [9] used external acoustic forcing on a NACA 64_3-618 at $Re_c = 64,000$ to show that forcing at $F^+ = 9.6$ near f^+_{sl} was most effective for fully separated flow. It is clear that for post-stall flows where f^+_{w} and f^+_{sl} are present, a large range of F^+ covering several orders of magnitude is expected to be effective for control. In terms of the effects of excitation amplitude, for both flow reattachment and separation delay, it has been observed that once a threshold amplitude has been achieved, further momentum input has little effect on the attached flow. This effect is well documented as a saturation of the lift coefficient increase with excitation amplitude for both steady (e.g., [64]) and unsteady (e.g., [68]) excitation. Saturation of the drag coefficient reduction was also observed by Feero et al. [26] for $F^+ = 0.84$, 9.9 and 58. The effect of excitation location, however, is not as clear.

It is typically assumed that in order for control to be effective, excitation should be applied as close as possible to the separation point, as stated by Greenblatt and Wygnanski [44]. While reasons for this were not specified, it is likely the result of well known linear instability theory which predicts that boundary layer profiles having inflection points, i.e. those found in the region of adverse pressure gradient near separation, are convectively unstable. However, depending on where separation occurs relative to the beginning of the adverse pressure gradient, positioning the actuator as close to separation as possible may

not be ideal. For example, Dovgal and Kozlov [24] showed that for an airfoil with an LSB operating at low Re_c and α, the receptivity of the flow upstream was more important than that at the separation point. The statement 'as close to separation as possible' also makes no distinction in the location of control *relative* to separation. It remains unclear whether upstream or downstream of separation is more beneficial as no definitive study has been performed. Furthermore, varying the slot location while maintaining a constant injection angle relative to the airfoil surface presents a signifiant challenge in experimental work. In a study by Hsiao et al. [47], the chordwise forcing location using ZNMF excitation was varied over 1.25% – 13.75% chord for post-stall flow on a NACA 63_3-018 airfoil ($Re_c = 300,000$). As shown in Figure 1.3, the authors found that the largest lift coefficient (C_L) enhancement occurred when the slot was at its most upstream location. However, the angle of the slot relative to the surface was not maintained constant, nor was the separation point indicated. Due to the relatively large angles-of-attack in excess of 18°, separation likely occurred very near the leading edge. As shown by the inset in Figure 1.3, the angle of the slot relative to the surface varied from approximately 90° to 45° from 13.75% to 1.25% chord. Thus, it is difficult to be conclusive based on the results of this study, as two potentially important parameters were varied simultaneously. In contrast, Amitay et al. [3] applied synthetic jet control to a modified NACA airfoil that used a cylinder as the leading edge section at $Re_c = 310,000$. With the synthetic jet slot housed in the cylinder, rotation of the cylinder allowed the chord location of the slot to be varied while maintaining the angle normal to the surface. The authors concluded that positioning the slot closest to separation was most effective for $5° \leq \alpha \leq 25°$, however the jet location relative to the separation point was not specified. Brehm et al. [14] performed a computational study on a NACA 63_3-018 airfoil at $Re_c = 64,000$, where the forcing location using wall-normal unsteady blowing was varied over approximately 2% to 40% chord. At $\alpha = 8.6°$ where a LSB was present, the authors found that forcing at 2% chord for $F^+ = 5$ was most effective, rather than forcing just upstream of separation.

1.4 Objectives and outline

The goal of the present study is to provide further understanding of the effects of control parameters on flow reattachment and performance improvement using synthetic jet control, with a focus on the effect of the slot location relative to separation. Previous work by the author focused on the effects of excitation frequency and amplitude on flow reattachment and subsequent drag reduction [25]. It was found that compared with high-frequency excitation ($F^+ = 58$), a lower threshold forcing amplitude was achieved

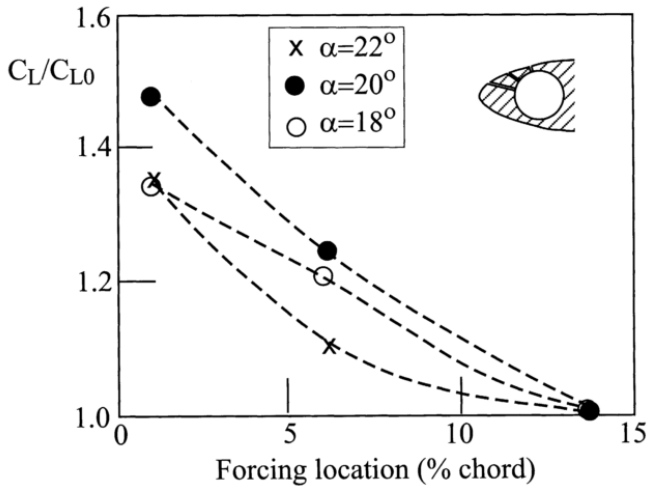

Figure 1.3: Variation in lift coefficient relative to the baseline case with chordwise forcing location from Hsiao et al. [47], adapted by Greenblatt and Wygnanski [44]. The inset shows the geometry of the three different slots near the leading edge.

for low-frequency excitation. In particular, excitation of the shear layer instability required the lowest excitation amplitude to steadily reattach the flow, while excitation of the global wake instability lead to unsteady reattachment. These measurements were performed with the actuator downstream of the separation point. The question remains; as the excitation location varies relative to the separation point, how will the threshold forcing amplitude vary for different excitation frequencies? In particular, is upstream or downstream forcing more effective? Finally, practical feedback sensing that could be used in a closed-loop control strategy will be developed and implemented. Closed-loop control, which is a complex topic requiring its own dedicated effort, would allow the energy input to be optimized while providing a more robust control strategy. The implementation of useful feedback sensing for a low Reynolds number experiment is a non-trivial precursor to closed-loop control.

The objectives for this thesis are as follows:

1. Perform a detailed characterization of the baseline flow field. Identify frequencies associated with the post-stall instabilities to guide selection of forcing frequencies for open-loop control. Ensure that the flow can be considered two-dimensional over a the majority of the model span.
2. Continue the investigation of excitation frequency and amplitude while adding excitation location as an additional control parameter. Quantify the global effect of

these parameters using lift and drag measurements. For varying excitation location, both upstream and downstream of separation, investigate whether a threshold amplitude is required for reattachment and how this behaviour may vary with excitation frequency/location.

3. Investigate the manner in which blowing ratio, excitation frequency and location affect the controlled flow using boundary layer and global flow-field measurements.

4. Use the open-loop control results to determine suitable quantities to be measured for feedback in a closed-loop control system. Implement sensors to perform the desired measurements.

The organization of this thesis is as follows. Chapter 2 describes experimental details of the wind tunnel facility, airfoil model, synthetic jet actuator, and the instrumentation used for measurements of velocity, pressure, etc. The baseline flow is discussed in Chapter 3, including the mean and temporal characteristics of the flow, two-dimensionality and the mean separation point. The effect of model end conditions on the two-dimensionality of the baseline flow is the subject of a paper in the proceedings of the *25th Canadian Congress of Applied Mechanics* [27]. Chapter 4 addresses characterization of the synthetic jet velocity frequency response, the uniformity of the velocity profile for the very high aspect ratio slot, and the technique for modulation of the control signal. Chapters 3 and 4 provide the fundamental information deemed necessary for a robust study of control parameters, which is detailed in Chapter 5. The first section in this chapter that highlights the effects of C_{μ}, F^{+} and x_{j}^{*} on aerodynamic performance is also the subject of an *Experiments in Fluids* publication [31]. This chapter also discusses the effects of control parameters on the mean flow and the dynamics of the controlled flow. A portion of this work appeared in the proceedings of the *10th International Symposium on Turbulence and Shear Flow Phenomena* [30]. Three-dimensionality of the controlled flow is the topic of Chapter 6, which is investigated using flow visualization and quantitative measurements. The flow visualization results appeared in a *Journal of Visualization* publication [32]. Chapter 7 summarizes the main results of this thesis and provides recommendations for future work on this project. Appendix A discusses the selection and implementation of sensors that could be used for feedback sensing in closed loop control. The apparatus developed for the dynamic calibration of the selected pressure sensors is the subject of a manuscript submitted to *AIAA Journal* [29].

Chapter 2

Experimental Methods

2.1 Wind tunnel facility

Experiments were performed in a low-speed, low-turbulence recirculating wind tunnel located in the Department of Mechanical and Industrial Engineering at the University of Toronto. The octagonal test section is 5 m long, 0.91 m wide and 1.22 m tall at the inlet. The corners have a constant angle but decrease in width along the test section length to increase the cross-sectional area and compensate for boundary layer growth. One of the side walls and the ceiling have clear acrylic inserts to allow optical access for flow visualization and optical based measurements. The flow enters the test section after passing through seven screens and a 12:1 contraction. Turning vanes guide the flow around the four 90° corners of the wind tunnel. The flow is driven by a six bladed axial fan, which in turn is belt driven by a motor located outside the wind tunnel on an isolating concrete pad. The fan housing is connected to the rest of the wind tunnel by flexible couplings such that potential vibrations from the fan are not transferred the the tunnel structure.

The freestream velocity in the test section is adjustable from approximately 2.5 m/s to 18 m/s and was monitored using a pitot-static tube located at the test section inlet. The freestream turbulence intensity at the center of the empty test section over a range of U_∞ is shown in Figure 2.1a (measured using hot-wire anemometry). The turbulence intensity is defined as u'_{rms}/U, where U and u'_{rms} are the mean and root-mean-square (RMS) of the streamwise velocity. The velocity signals were high-pass filtered at 0.5 Hz to remove large period oscillations that are not considered 'turbulence', but rather unsteadiness of the mean flow. The results demonstrate that over a range of freestream velocities, the mean turbulence intensity is 0.08% over a frequency bandwidth of $f = 0.5$ Hz – 10 kHz. The power spectral density of the streamwise velocity fluctuations, P_{uu}, for

the same values of U_∞ in Figure 2.1a are given in Figure 2.1b. These spectra indicate the background noise in velocity for a particular U_∞. Note that peaks at 120 Hz and all harmonics of this frequency are due to electrical line noise in the hot-wire anemometer.

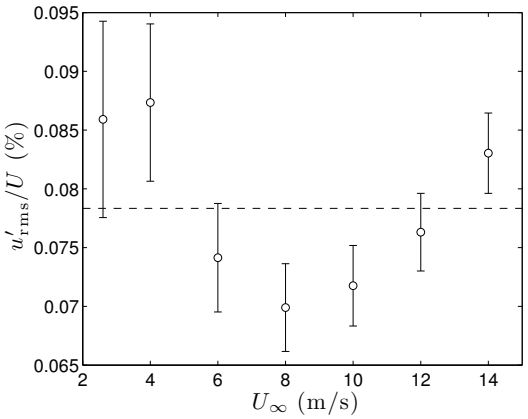

(a) Freestream turbulence intensity. The dashed line indicates the mean value.

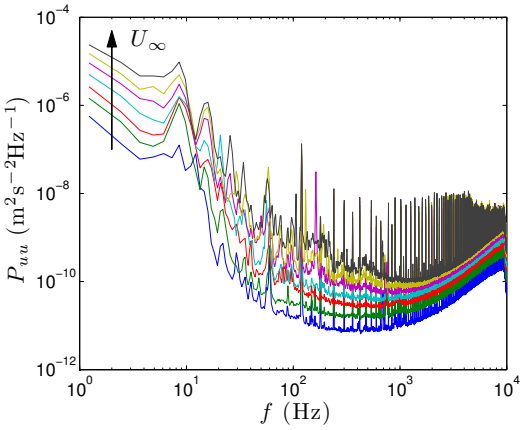

(b) Power spectral density of streamwise velocity fluctuations.

Figure 2.1: Characterization of the centerline velocity in the empty test section over a range of U_∞. The power spectra in (b) are for the same values of U_∞ shown in (a).

The uniformity of the flow at the test section inlet was assessed for several freestream velocities using two-component hot-wire velocity measurements. The details and results of this measurement are given in Appendix B.

2.2 Airfoil model

An airfoil model with a NACA 0025 profile was designed and manufactured for the experiments in this work. Compared to a model used in previous work [82; 40; 25], the new model was designed to easily implement various sensors and actuators. An exploded schematic of the model in Figure 2.2 shows the five main components of the model assembly. All components were CNC machined from aluminium. A particular goal of this model was the ability to employ synthetic jet control over approximately 1/3 of the model span. As such, the 375 mm long center section of the model is hollow and consists of three components: top and bottom halves, and an insert within the top half that covers 5% – 78% chord. The center section was created in two halves to facilitate the machining of 64 pressure taps at midspan distributed evenly between the upper and lower surfaces. The pressure taps are 0.5 mm in diameter and 2 mm long, and are normal to the surface at each location. Counterbores on the inner surface of the model allow the

connection 2.4 mm outer diameter plastic tubing to the static pressure taps using epoxy. The insert in the top half of the center section serves several purposes: access to the inside of the model when it is fully assembled, and the housing of actuators/sensors. The present experiments use this insert to house the synthetic jet (Section 2.3) and pressure sensors (discussed in Appendix A), but it is designed as a modular component that could be replaced for future experiments with different requirements.

The center section section of the model is joined to two solid outer section that are 255 mm in length. A 45 mm $\times$ 25 mm channel passes through the outer sections to allow routing of pressure tubing and wires to the inside of the model. Each outer section is joined to the center section using four M10 screws and two 4 mm dowel pins are used for alignment. With the model fully assembled, the surface was sanded to remove tool marks and create a smooth transition between the five mating parts. The model is designed for rotation about quarter-chord and the outer sections include bores for mounting shafts at this location.

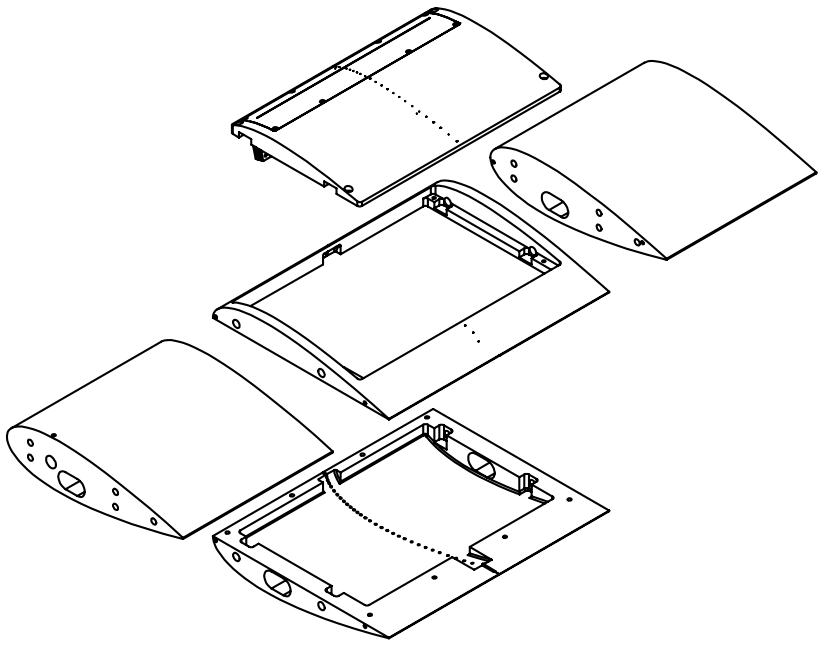

Figure 2.2: Exploded view of the NACA 0025 airfoil model.

The model was installed spanning the width of the test section with its leading edge approximately 400 mm downstream of the test section inlet. A top view of the model as installed in the wind tunnel is shown in Figure 2.3. The airfoil has a chord length $c = 300$ mm and a spanwise length of $b = 885$ mm, giving an aspect ratio $b/c \approx 3$. The model is supported at each spanwise end by a shaft passing through a ball bearing. The

shaft on the bottom side (as viewed from above in Figure 2.3) is supported by a bearing housing mounted to the clear acrylic test section wall, which allows optical access. On the opposite end, a mechanism is included that allows the pitch angle of the model to be fixed and also provides a flat reference surface for measuring the angle of rotation (denoted 'rotation lock' in the schematic). Aerodynamic $\alpha = 0°$ was established by adjusting the model pitch until a symmetric pressure distribution was measured at midspan. The angle-of-attack relative to 0° was set using an digital inclinometer with an accuracy of $\pm 0.05°$.

Circular end plates are fixed to each end of the model to improve the spanwise uniformity of the baseline flow, which is discussed in Section 3.1. There was no gap between the model and the end plates. The end plates were designed according to the Boutilier and Yarusevych [11], who surveyed the literature and designed their end plates specifically for low Reynolds number airfoil studies. The end plates are $2.25c$ in diameter and extend $0.8c$ upstream of the leading edge. The plates are chamfered at 30° to avoid flow separation at the end plate leading edge. The end plate on the bottom is made from 4.5 mm thick clear acrylic for optical access, while the upper one is 2.3 mm thick aluminium. The end plates add an additional 0.5% solid blockage to the model. In addition to removing effects of the gap between the model ends and the tunnel walls, the end plates also prevent the boundary layer on the tunnel walls from growing onto the model. A measurement at the location of the end plate leading edge showed that the boundary layer on the tunnel was approximately 12 mm thick. The end plates are approximately 15 mm from the tunnel wall on each side and are thus outside the boundary layer.

The coordinate systems used for data presentation are defined in Figure 2.4. The global coordinates $[X, Y, Z]$ are fixed at quarter-chord (the model rotation axis) and define the streamwise, transverse and spanwise directions, respectively. Two other coordinate systems are employed: surface attached coordinates (i.e., wall-normal and tangential), and local airfoil coordinates (i.e., chord and thickness). However, only the chordwise direction x (with $x = 0$ at the leading edge) and the wall-normal direction y are used when presenting data. The chordwise coordinate is used rather than the wall-tangential distance (i.e., the arc length from the leading edge) as it is convenient to define positions along the airfoil surface over the range $x/c \in [0, 1]$. The use of the chordwise coordinate x is standard for the presentation of data such as surface pressure distributions and boundary layer velocity profiles.

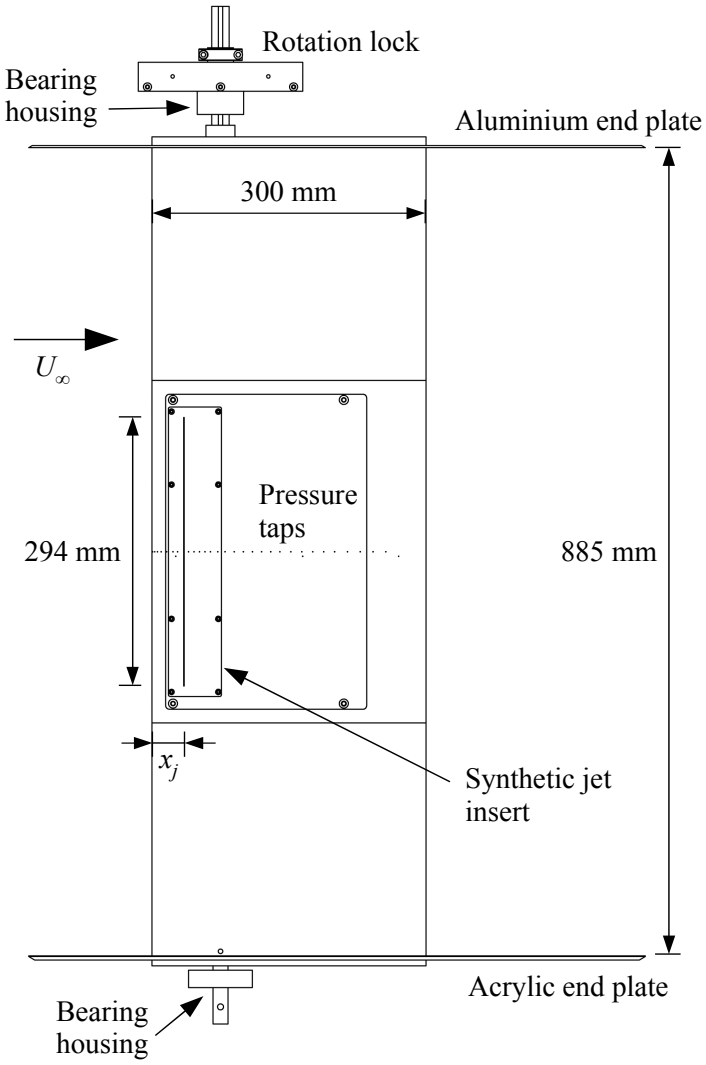

Figure 2.3: Top view of the experimental setup in the wind tunnel including the airfoil model, end plates and mounting hardware (tunnel walls not shown).

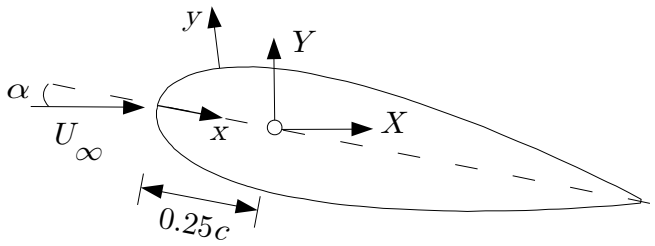

Figure 2.4: Description of the coordinate systems.

2.3 Synthetic jet

A synthetic jet actuator was designed to provide spanwise uniform forcing over approximately 1/3 of the model span and allow the chordwise location of forcing to be varied. This was accomplished by a synthetic jet with a single slot that is 0.5 mm wide and 294 mm long, as shown in Figure 2.5. A cross-sectional schematic of the SJA installed in the airfoil model is also provided in Figure 2.6. The synthetic jet is driven by 16 piezoelectric diaphragms that are 30 mm in diameter. Eight diaphragms are installed along each of the two walls parallel to the slot. Thus, the direction in which the piezo diaphragms oscillate is normal to the direction of the flow through the slot. The synthetic jet is made up of two main components: the cavity assembly and the slot insert. To vary the chordwise location of the slot while maintaining an angle normal to the surface, the slot was accurately cut using wire electrical discharge machining out of a modular insert that matches the airfoil profile. A new insert was created for each slot location. The slot insert is joined to the cavity assembly, which is made up of four plates that clamp the piezoelectric diaphragms and form the cavity. The slot insert also contains pressure taps at midspan, with a small gap in the taps to accommodate the slot. At the interface between the slot insert and the cavity assembly, vacuum grease was used as a seal. All parts were made from aluminium, except for the outer two clamping plates that were made of Delrin for electrical isolation of the piezo diaphragms. Plastic inserts were also added to the inner aluminium plates for electrical isolation.

Four different slot inserts were created such that two forcing locations upstream, and two downstream of the mean separation point could be tested. The locations are: $x_\mathrm{j}/c = [0.087, 0.117, 0.143, 0.173]$. The location $x_\mathrm{j}/c = 0.087$ represents the most upstream location where the synthetic jet could feasibly be installed within the airfoil model. The selection of the other slot locations was based on the chord location of the mean separation point under the flow conditions of interest, discussed in Section 3.3.

2.4 Flow visualization

Surface flow visualization techniques were used to investigate the three-dimensionality of the reattached flow due to forcing with a long, but finite length synthetic jet slot. Two surface visualization techniques were employed: tuft and oil film.

Tuft visualization requires attaching a number of short segments of string/thread to the surface. Tufts approximately follow the instantaneous motion of the flow and highlight regions of unsteadiness. For the tuft flow visualization studies, yarn tufts of

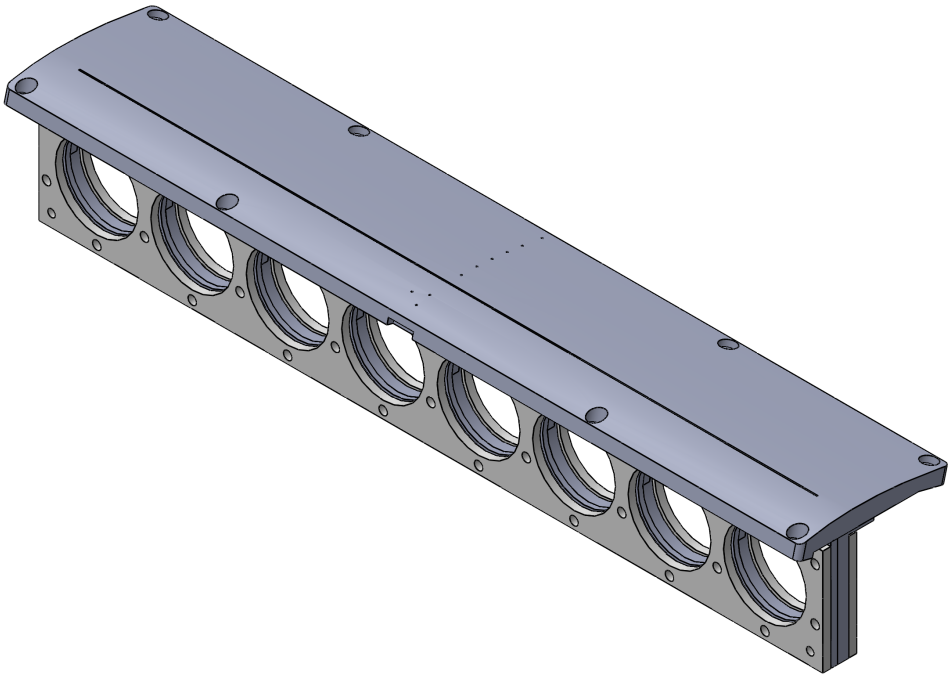

Figure 2.5: Solid model of the synthetic jet actuator. One of four slot inserts is shown as part of the assembly.

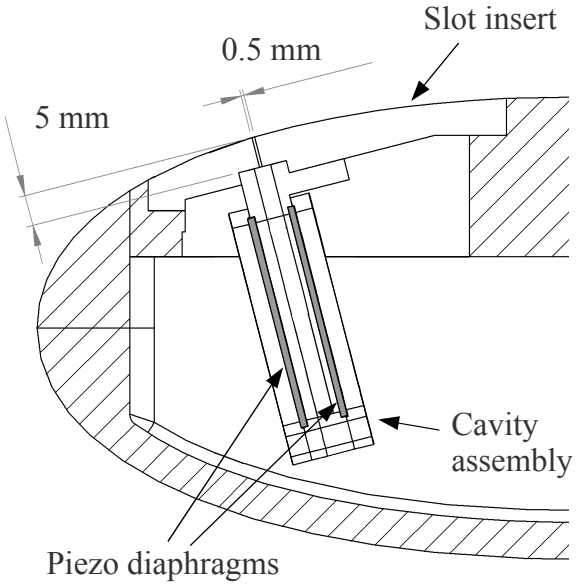

Figure 2.6: Cross-sectional schematic of the synthetic jet actuator installed in the airfoil model.

approximately 0.75 mm in diameter and 25 mm in length were fixed to the surface in four spanwise rows at $x/c = 0.3$, 0.47, 0.63 and 0.85. Tufts were not placed further upstream to avoid interfering with the flow. The tufts were attached to the surface using tape that was approximately 0.04 mm thick. The spanwise spacing between tufts was approximately 25 mm, except at $x/c = 0.85$ where they were spaced by 37.5 mm to avoid tufts tangling due to increased unsteadiness near the trailing edge.

The oil film technique was used to visualize time-averaged surface streamlines. The oil mixture used for the present study was a light mineral oil combined with lampblack pigment in a ratio of approximately 10:1 by volume. Prior to applying the oil with a foam brush, a portion of the model surface was covered with a white adhesive plastic film that was 0.05 mm thick. The purpose of the film was two-fold: to protect the pressure taps from clogging and to provide better contrast with the black pigment. Photographs were taken after 15 minutes of run time. Through repeated trials it was determined that this was a sufficient amount of time for the pigment streaks to form. For each of the two visualization techniques, a camera mounted on a tripod above the test section was used to capture images.

2.5 Instrumentation

Mean pressures were measured using differential pressure transducers. Two *MKS Baratron* 226A transducers were used: one with a bidirectional range of $\pm$26.7 Pa, and another with a range of 267 Pa. The accuracy of the former is $\pm$0.08 Pa (0.3% of full-scale), while the latter is $\pm$0.3% of-reading. The 267 Pa transducer was connected to a static-pitot probe used to measure the freestream velocity at the test section inlet. The 26.7 Pa bidirectional transducer was used in conjunction with a 64 channel *Scanivalve* multiplexing unit for the measurement of airfoil surface pressures. The same transducer was also used with a static-pitot probe to measure mean velocity in the airfoil wake.

Hot-wire anemometry was used to measure time resolved velocity in wind tunnel experiments concerning the airfoil and bench-top synthetic jet experiments. A *Dantec* 56C01 constant temperature anemometer (CTA) was used to operate single-wire probes with 5 µm diameter and 1 mm sensing length (wire aspect ratio of 200). Hot-wires were operated at an overheat ratio of 1.6. At typical measurement velocities, a square wave response showed a cut-off frequency of approximately 70 kHz for the hot-wire/CTA system. For wind-tunnel experiments, hot-wire calibration was performed *in situ* using a static-pitot probe as reference. A *Dantec* calibration jet was used to calibrate probes for for synthetic jet measurements, where it was necessary to calibrate over a larger velocity

range. The calibration jet apparatus has a built in pressure transducer that serves as reference with an accuracy that is ±1% of-reading. Conversion of voltage to velocity was performed using a King's Law curve fit to the calibration data such that velocities below the calibration range could be interpreted. The minimum calibration velocity in the wind tunnel was $\sim$ 2.5 m/s, and $\sim$ 1.5 m/s for the calibration jet. For measurements taken over the course of an hour or more, the temperature correction technique of Hultmark and Smits [49] was employed. This temperature correction method requires measurement of the ambient temperature, which was acquired using a T-type thermocouple. The effect of ambient pressure was assumed to be negligible compared to temperature and a constant value was used.

Input signals used to drive the synthetic jet's piezoelectric diaphragms were created using a *Rigol* DG1022 function generator. The function generator signal was amplified by two *Mide* QPA3202 power amplifiers with a voltage gain of 50:1. Each amplifier was used to drive half of the piezoelectric disks to avoid reaching the amplifier's peak current limitation at high voltages. The piezo disks were operated at voltages up to 200 V peak-to-peak.

Velocity measurements in the wake of the airfoil were performed using either hot-wire or a static-pitot tube. The probes were positioned using a three-axis traverse located downstream of the model in the test section. This traverse covers a measurement volume that is 4 m $\times$ 0.5 m $\times$ 0.5 m in the $[X, Y, Z]$ directions with a spatial resolution of approximately 0.3 mm.

2.5.1 Particle image velocimetry

Planar particle image velocimetry (PIV) was used for the measurement of velocity fields in the streamwise-transverse plane. The goal of the PIV measurements was to measure the global flow field over the airfoil suction surface for baseline and control cases. This presents a challenge due to the size of the measurement domain given $c = 300$ mm. While it would be possible to image this domain with one camera, the required distance of the camera from the measurement plane and the camera resolution would severely limit the spatial resolution of the vector field. A second option with a single camera would be to move the camera and capture smaller fields of view, and then stitch the results together in post processing. This solves the issue of spatial resolution, but would be time consuming for a large number of test cases. Since two PIV cameras were available, the desired measurement plane was captured simultaneously using two overlapping fields of view (FOV), as shown in Figure 2.7a. The cameras were offset in the streamwise direction such that there was an overlap of approximately 40%. As shown in Figure

2.7a, each camera window is approximately 218 mm × 184 mm in the streamwise and transverse directions, respectively. The size of the resulting measurement domain is 335 mm × 184 mm and covers the range $X/c \in [-0.30, 0.81]$ and $Y/c \in [-0.16, 0.44]$. For select control cases, measurements in the XY plane were performed at four spanwise locations over $-0.49 \leq Z/c \leq 0$ to investigate the three dimensional effects of control. The spanwise planes were spaced by $\Delta Z/c = 0.17$ (50 mm), as shown in Figure 2.7b. Both the cameras and laser optics above the test section were mounted on rails that allowed manual positioning along Z.

The flow field was imaged by two *LaVision Imager* sCMOS cameras with 2560 pixel × 2160 pixel resolution. Mounted to the cameras were 60 mm *Nikon* lenses with a minimum f-stop of 2.8. Using this camera and lens combination at the appropriate viewing distance, the pixel scale was approximately 11 pixels/mm. The flow was seeded using sebecate particles created by a *LaVision* aerosol generator. The particles were illuminated by a *Quantel EverGreen* dual pulsed Nd-YAG 532 nm laser with a pulse energy of 200 mJ and a maximum repetition rate of 15 Hz. A series of optical lenses were used to spread the laser beam into a thin sheet with a divergence angle of approximately 15° such that the entire measurement domain was illuminated. As shown in Figure 2.8a, the laser beam was directed above the ceiling of the test section using mirrors before being spread into a sheet that entered the test section through an acrylic panel. The model was spray painted matte black but due to the presence of pressure taps at midspan and the synthetic jet slot, no further anti-reflective coating (e.g., rhodamine) was applied. A custom calibration target that covered the majority of the measurement domain, shown in Figure 2.8b, was created using 6 mm dots on a 12 mm square pitch. The target was adhered to a flat piece of 19 mm thick MDF panel. Rotation of the target about X and Y was carefully adjusted to ensure it was oriented in the streamwise-transverse plane. In addition to camera calibration, the target was used to adjust the cameras such that they were aligned with the $[X, Y]$ coordinates.

The acquired images were processed using *LaVision DaVis* software. Prior to PIV processing, a sliding average filter was applied to minimize background light and improve signal-to-noise. The first 2 mm from the airfoil surface had to be masked due to overwhelming laser reflections in this area. Velocity vectors were computed using a sequential cross correlation algorithm that performed a single pass with 32 × 32 interrogation windows, followed by two passes with 16 × 16 windows with 50% overlap. The time between laser pulses varied from 90 µs to 100 µs to give a maximum pixel shift of approximately 8 pixels, which is in accordance with a maximum shift that is 1/4 of the initial interrogation window size [54]. Image pairs were acquired at 5 Hz and can be considered statistically

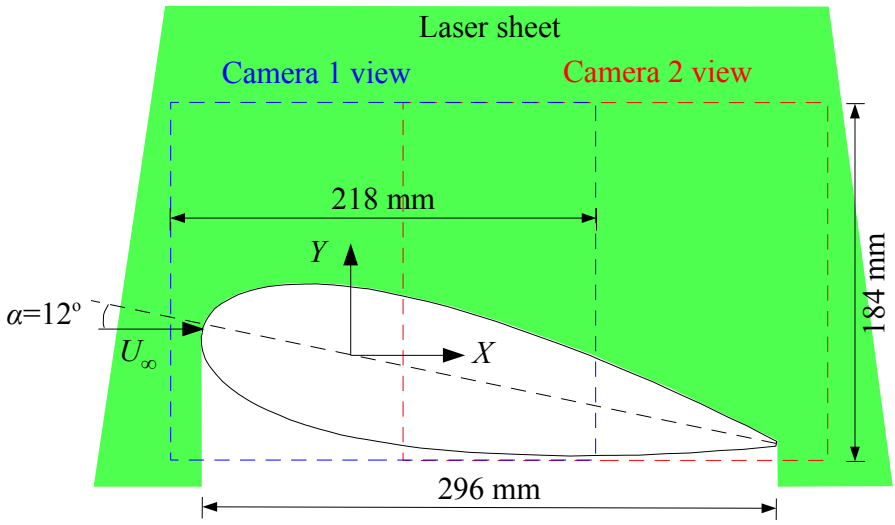

(a) Camera FOV and laser sheet configuration in the streamwise-transverse plane for $\alpha = 12°$.

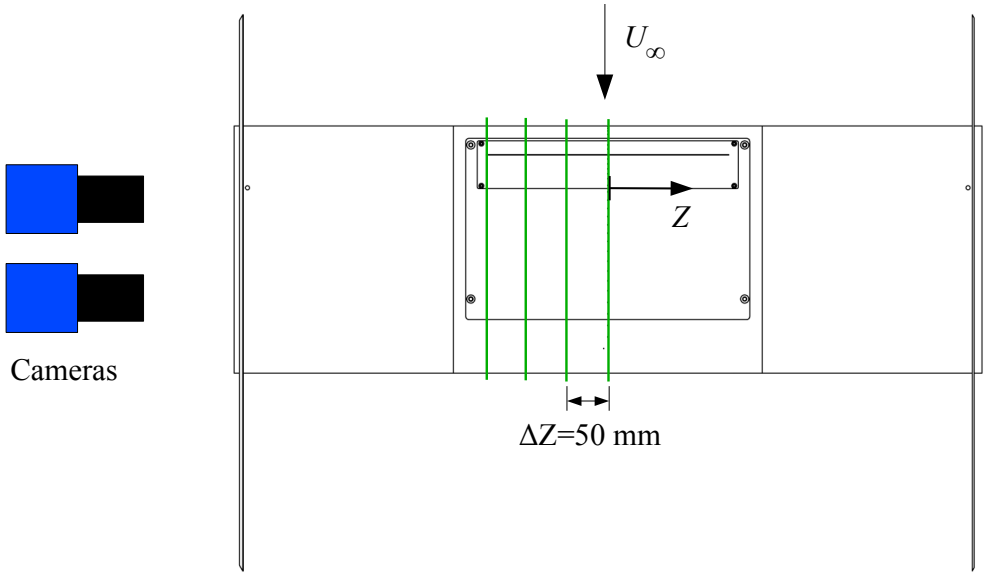

(b) Laser sheet spacing for measurements at spanwise locations over the controlled region.

Figure 2.7: PIV laser sheet and camera configuration for capturing the global flow field over the suction surface.

independent (see Section 2.7). Time- and phase-averaged quantities were computed from 500 image pairs. In the overlapping region of the two fields of view (Figure 2.7a), a linear weighted average was employed to stitch the velocity fields from each camera together. The resulting velocity field contains 490 × 265 vectors with a spatial resolution of approximately $\Delta X/c = \Delta Y/c = 0.0023$. An example of instantaneous transverse velocity fluctuations, v', is shown in Figure 2.9. Included in the figure are the weighting func-

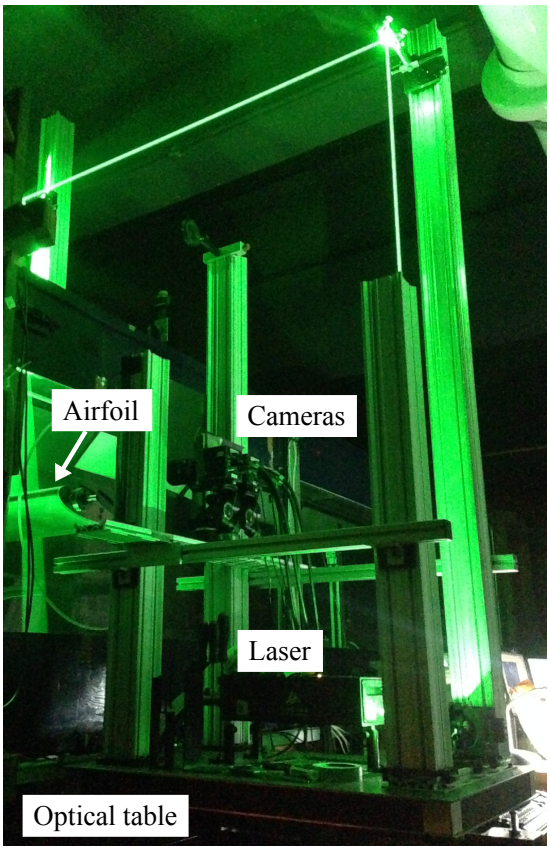

(a) Photo of the PIV system during operation.

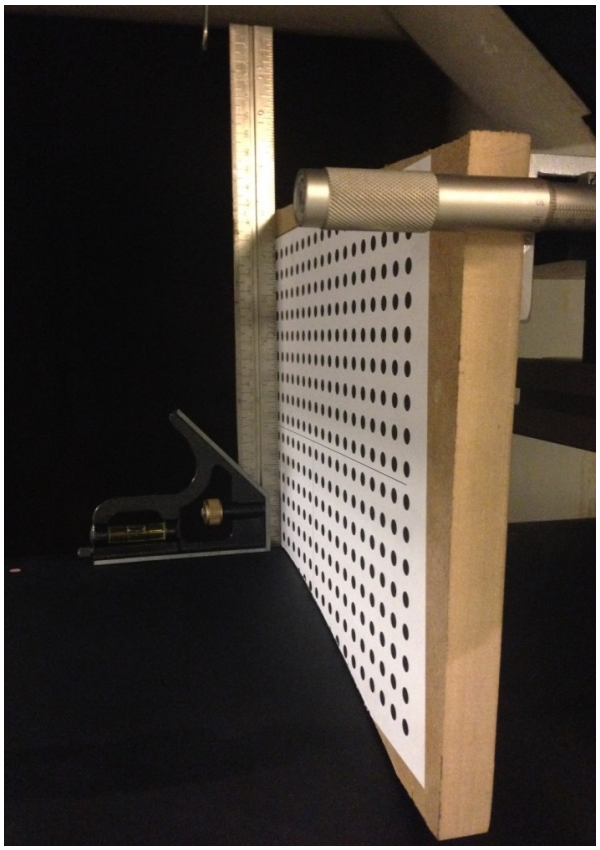

(b) Custom calibration target above the airfoil surface. A square is shown being used to ensure the target was normal to the surface.

Figure 2.8: PIV setup photos.

tions applied to the velocity vectors from each camera. The figure demonstrate that no noticeable artifacts were introduced into the velocity field by the stitching process.

2.6 Boundary layer traverse

A traverse system was designed and constructed specifically to accommodate velocity measurements in the airfoil boundary layer/separated shear layer using hot-wire anemometry. The three-axis traverse used for wake measurements has several limitations precluding its use for boundary layer measurements: relatively large solid blockage (12%), insufficient spatial resolution and insufficient rigidity. Boutilier and Yarusevych [11] showed that for low Reynolds number airfoil flow and traverse blockages between 4% – 8%, positioning a traverse near the model could change the surface pressure distribution con-

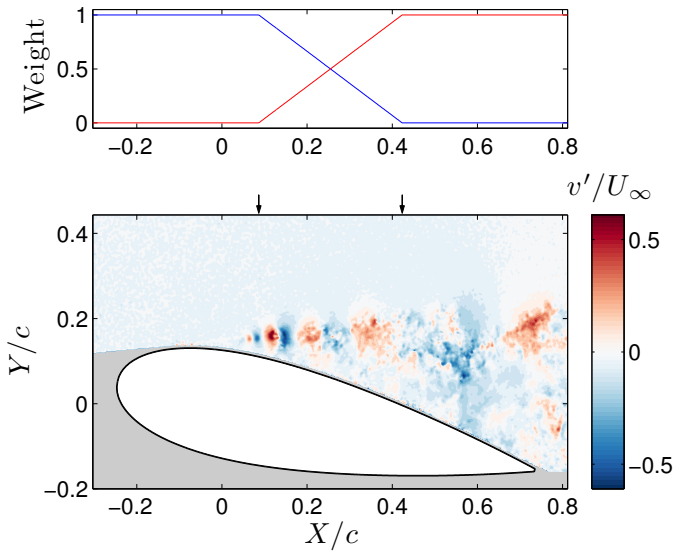

Figure 2.9: Typical instantaneous fluctuating transverse velocity field measured by PIV. Arrows on the top axis denote the overlap region between the two camera views. The weighting functions applied to cameras 1 and 2 for stitching are shown in the upper plot in blue and red, respectively.

siderably depending on the flow conditions (i.e., pre-stall separation bubble, incipient stall, post-stall). Therefore, the goal was to design a traverse with minimal blockage that could be positioned near the airfoil to maintain rigidity in the arm holding the hot-wire probe. As shown in Figure 2.10, this was accomplished by a traverse with the linear stages located outside of the wind tunnel and an arm that enters the test section through a slot in the ceiling. The traverse has three degrees of freedom: two translational (streamwise and transverse), and one rotational (pitch angle of the hot-wire arm). The rotary stage (with 0.02° resolution) controls the pitch of the 12.5 mm diameter hot-wire arm such that the angle relative to the local surface tangent is maintained under 10° [15]. Two stepper motor driven linear stages with 5 µm resolution are bolted to a 9.5 mm thick steel plate mounted to the test section ceiling. The plate is slotted such that a 1.0 m long, 51 mm × 13 mm steel arm (referred to here as 'main arm') extending into the test section can move in the streamwise direction. The slot in the test section is equipped with a zipper system that is self-sealing as the traverse moves along X. The main arm is covered by a 3D printed sleeve that has a NACA 0015 profile (19.5 mm maximum thickness) to minimize flow-induced vibrations of the traverse. With a hot-wire installed, the hot-wire probe tip is located 400 mm from the axis of rotation. The spanwise position of the hot-wire can be varied manually using the setup shown in Figure 2.10, or a third linear stage with smaller cross-section (relative to the streamwise/transverse stages) can be installed to

automate this movement. The traverse was typically not equipped with this third linear stage. As the traverse moves in the transverse direction, its solid blockage varies from 1.6% to 2.2% and therefore produces negligible disturbance to the flow over the model. Repeatability of the traverse motion within ±5 μm and ±0.05° was verified using a dial indicator for the linear and rotary stages, respectively. For the measurement of a boundary layer profile, the location of the surface ($y = 0$) was found by establishing electrical contact between the hot-wire probe and the model. This technique is advantageous in that it can be done remotely without stopping the tunnel, unlike optical based surface finding techniques. The uncertainty in y locations is ±12.5 μm ($4.2 \times 10^{-5}c$) based on the size of the steps taken while approaching the surface and locating $y = 0$. Backlash in the linear stages was accounted for when moving to the first measurement point away from the surface.

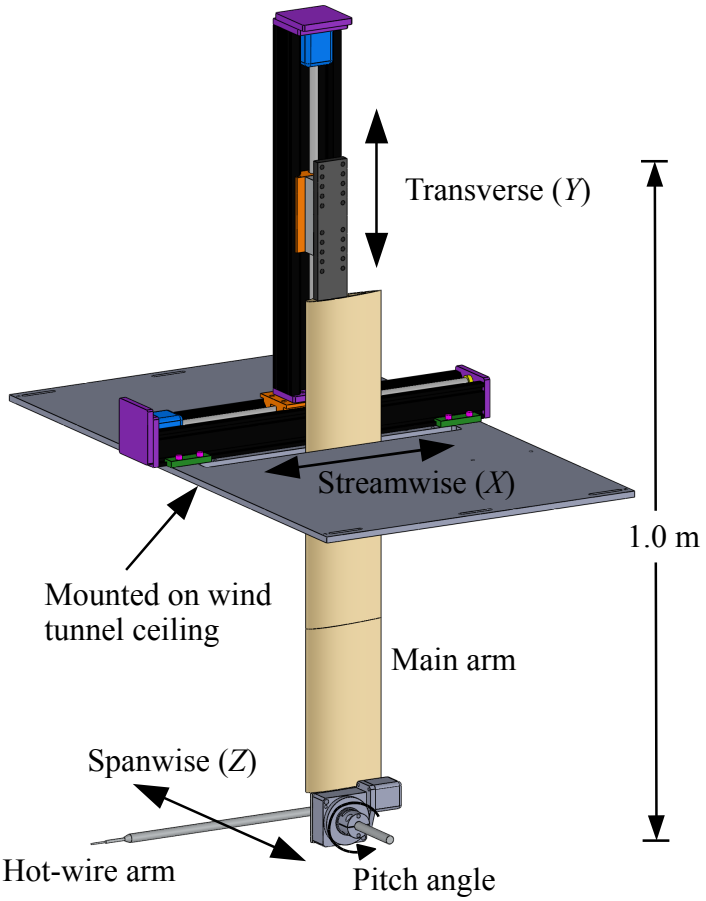

Figure 2.10: Solid model of the boundary layer traverse.

2.7 Measurement uncertainty

The total measurement uncertainty is due to the contributions of bias errors and random errors. Bias errors are fixed and affect the measurement in a constant way, while random errors are due to small errors from multiple sources that affect the measurement in an unpredictable way [72]. For the purpose of this study, it is assumed that bias errors supplied with measurement instruments are at the 95% confidence interval. All uncertainties will be given at this confidence interval. Random errors in mean quantities were computed as $\pm 2\sqrt{\sigma^2/N}$, where σ^2 is the variance of a particular quantity and N is the number of independent samples. According to George et al. [37], a statistically independent sample occurs every $2T_\mathrm{I}$, where T_I is the integral time scale. While T_I is strictly defined based on the autocorrelation of a signal, it may be estimated as the convection time of the largest scales in the flow [75]. The integral time scale was estimated as $T_\mathrm{I} \approx c/U_\infty$ by assuming the largest scales are on the order of the airfoil chord. Based on this definition, samples acquired at rates below approximately 9 Hz are statistically independent for $U_\infty = 5.2$ m/s ($Re_c = 100,000$). A bootstrap resampling algorithm [7] was used to estimate the random error in RMS quantities. Data was down-sampled at a rate of $(2T_\mathrm{I})^{-1}$ prior to resampling such that successive samples in the time series were statistically independent.

Sources of bias errors in hot-wire measurements include calibration equipment, calibration data reduction, probe orientation, wire geometry, and others. However, bias errors due to calibration are known to dominate [53]. Bias errors in velocity measured by hot-wire were computed according to the methodology of Yavuzkurt [86], who showed that the relative bias error due to calibration is equivalent for instantaneous, mean and RMS velocities. This technique accounts for bias errors in the calibration equipment (i.e., pressure transducer, thermocouple, etc.) and the error in the curve fit to the calibration data. The bias error for *in situ* calibration of hot-wires in the wind tunnel was estimated to be less than 0.5% due to the 0.3% of-reading accuracy of the reference pressure transducer. To account for effects of the hot-wire alignment relative to the reference pitot tube, a conservative total bias error of 1% was assumed.

Representative values of bias, random and total errors for primary measurement quantities (i.e., velocities and pressures) are given in Table 2.1. The total error is obtained by adding the bias and random error in quadrature. The freestream velocity was derived from measurements of mean dynamic pressure ($q_\infty = 1/2\rho U_\infty^2$), temperature and atmospheric pressure. All other velocities in Table 2.1 were obtained by hot-wire. Other than U_∞, details of the measurement from which the errors were obtained are given in the table footnotes. While the bias error in velocity for a hot-wire measurement is a relative

quantity obtained by the methodology of Yavuzkurt [86], for boundary layer profiles it is misleading to express the random and total error as relative quantities. This is due to the fact that the mean and RMS velocity both go to zero at certain locations, but the random error does not necessarily follow the same trend. The same is true of mean surface pressures on the airfoil and phase-averaged synthetic jet velocities, which have values that cross and approach zero, respectively. Therefore, errors are given as absolute values where appropriate and the maximum value of each quantity for the example measurement is given for scale.

Table 2.1: Representative measurement uncertainties in primary quantities.

		Error (±)		
	Max	Bias	Random	Total
q_∞	-	0.3%	~ 0	0.3%
U_∞	-	0.23%	~ 0	0.23%
Mean velocity [a]	5.8 m/s	1.0%	0.01 – 0.17 m/s	0.01 – 0.18 m/s
RMS velocity [b]	1.1 m/s	1.0%	0.03 – 0.11 m/s	0.03 – 0.11 m/s
Mean pressure [c]	15.2 Pa	0.08 Pa	0.02 – 0.15 Pa	0.08 – 0.17 Pa
Phase-averaged velocity [d]	8.9 m/s	1.6%	0.001 – 0.008 m/s	0.02 – 0.14 m/s

[a] Boundary layer velocity profile measured by hot-wire at $x/c = 0.4$ for the baseline flow at $Re_c = 100,000$ and $\alpha = 12°$

[b] Same as *a*

[c] Surface pressure distribution for the baseline flow at $Re_c = 100,000$ and $\alpha = 12°$

[d] Hot-wire measurement at the jet exit plane for $f_e = 1000$ Hz and 60 V input amplitude

Uncertainty quantification for PIV is inherently difficult due to the number of variables affecting the computed velocity fields and remains a topic of active research. In recent years, the 'uncertainty surface' method of Timmins et al. [74] was implemented into LaVision's DaVis software. This is a correlation based algorithm that considers the errors due to four sources: particle displacement, particle image diameter, particle image density and shear. The DaVis software outputs a single uncertainty field for each instantaneous velocity component, which is considered to be the instantaneous bias error. The errors in velocity statistics were computed using the error propagation methodology described by Wilson and Smith [80]. Figure 2.11 shows a representative example of the bias, random and total error in the mean total velocity (i.e. mean velocity magnitude) for the baseline flow at $Re_c = 100,000$ and $\alpha = 12°$. The total error in the PIV measurements is dominated by the correlation based bias error, with the random error being less than $0.03U_\infty$ in this case. As expected, the bias and total error are largest in the region close to the airfoil surface due to reduced correlation levels from laser reflections.

The propagation of error from directly measured quantities (i.e. velocity, pressure,

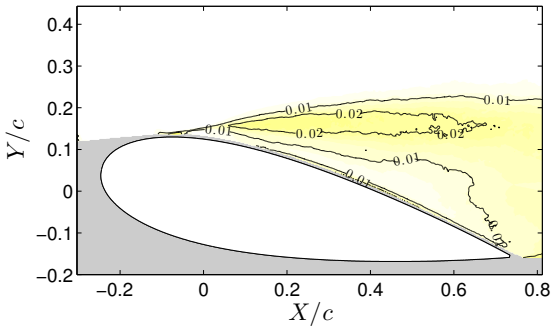

(a) Random error

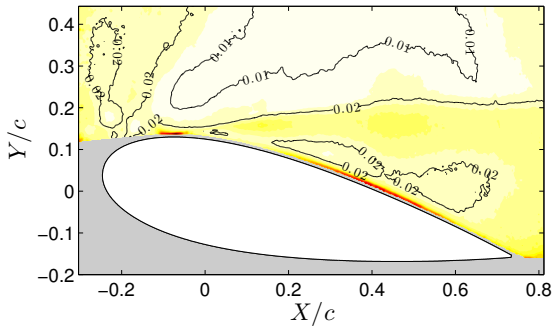

(b) Bias error

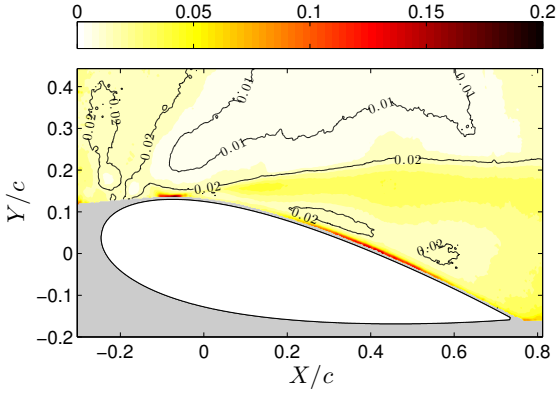

(c) Total error

Figure 2.11: Filled contours of random, bias and total error in the mean total velocity measured by PIV for the baseline flow at $Re_c = 100,000$ and $\alpha = 12°$. Errors are presented as a fraction of U_∞. Contours at $0.01U_\infty$ and $0.02U_\infty$ are shown for reference and grey indicates the masked area.

temperature, etc.) into derived quantities was accomplished using both analytical and simulation based approaches. The analytical approach was applied to quantities having relatively simple functional relationships with measured quantities (e.g., U_∞ from q_∞ measured by pitot-static tube) using the conventional Taylor series expansion methodology. For derived quantities with more complex functional relationships, a Monte Carlo simulation based approach was used. A large number of realizations of the derived quantity were computed from measured quantities that were randomly generated within the appropriate error bounds. The uncertainty in a simulated quantity was taken as twice the standard deviation of the realizations, which assumes the quantity follows a normal distribution.

2.8 Phase averaging and triple decomposition

Phase-averaging is a technique that can be used to extract the organized part of a signal that contains both coherent and random fluctuations. When a flow is excited periodically, the excitation signal can be used as a reference to extract the coherent fluctuations. A time-varying instantaneous quantity $g_{\text{tot}}(t)$ can be decomposed using a triple decomposition according to Hussain and Reynolds [51]:

$$\begin{aligned} g_{\text{tot}}(t) &= G + g(t), \\ g_{\text{tot}}(t) &= G + \tilde{g}(t) + g'(t), \end{aligned} \tag{2.1}$$

where

$$G = \overline{g} = \lim_{T\to\infty} \frac{1}{T} \int_0^\infty g_{\text{tot}}(t)\, \mathrm{d}t \tag{2.2}$$

is the time-average of $g_{\text{tot}}(t)$ and T is the total signal length. The total, coherent and turbulent fluctuations are defined as $g(t)$, $\tilde{g}(t)$ and $g'(t)$, respectively. Note that for baseline flows without forcing, we define $\tilde{g}(t) = 0$ and therefore, $g'(t) = g(t)$. The phase-average is defined as:

$$\langle g_{\text{tot}} \rangle(t) = \frac{1}{n} \sum_{i=0}^{n} g(t + i\tau), \tag{2.3}$$

where n is the number of cycles. The coherent and turbulent fluctuations can be extracted from the instantaneous signal by:

$$\tilde{g}(t) = \langle g_{\text{tot}} \rangle(t) - G, \text{ and} \tag{2.4}$$

$$g'(t) = g_{\text{tot}}(t) - \langle g_{\text{tot}} \rangle(t). \tag{2.5}$$

In practice, the excitation and/or trigger signal from the function generator were used as reference for phase-averaging. The excitation signal acquired simultaneously with time resolved measurements (e.g., hot-wire) was used in post-processing to compute phase-averaged cycles. For PIV measurements acquired slowly at 5 Hz, the trigger signal was input to the timing unit to synchronize measurements at a particular phase angle. A time delay between the trigger and PIV acquisition was adjusted to change the phase angle.

2.9 Summary

This chapter has discussed the experimental facilities, instrumentation and techniques used in this investigation. The primary measurements were of surface pressure on the airfoil and velocity at various locations measured using hot-wire anemometry, pitot-tube or PIV. The measurement uncertainty range of primary measured quantities was also given for representative cases.

Chapter 3

Baseline Flow

3.1 Two-dimensionality

The spanwise length of the model was originally $b = 895$ mm to span the 920 mm width of the test section. This left a gap of approximately 7.5 mm, or $0.025c$, between the model and the tunnel wall on either end. It was speculated that with a sufficiently small gap, two-dimensional flow could be produced without the use of end plates. This would have reduced the overall complexity of the design and not hindered optical access to $[X, Y]$ planes in any way. To access the two-dimensionality of the flow, measurements of the mean streamwise velocity, U, were performed $2c$ downstream of the trailing edge in the $[Y, Z]$ plane by traversing a static-pitot tube. The results of such a measurement for $\alpha = 10^\circ$ and $Re_c = 100,000$, where the flow was known to be stalled (by surface pressure measurements), are shown in Figure 3.1. The contour plot of U demonstrates that over only the center 67% of the model span, not only is the flow non-uniform along Z, but the flow is not symmetric about midspan. In fact, the presence of the gap on the $Z/c = 1.5$ end appears to cause large enough disturbances that the flow becomes quasi-attached. Also shown in this figure are transverse profiles of U at $Z/c = 0$ and $Z/c = 1$. The fact that the profile of U at $Z/c = 1$ is not smooth despite the long sampling time suggests that the flow is highly unsteady and is 'flapping' between states of stall and attached flow. Thus, gaps of only $0.025c$ at an aspect ratio $b/c = 3$ are large enough to cause the flow to be highly non-uniform at this Reynolds number.

In an effort to improve the spanwise uniformity of the flow, 6.35 mm thick end caps with the same airfoil profile were machined and fixed to the model ends. This reduced the gaps to approximately 1.2 mm ($0.003c$). A measurement at $\alpha = 10^\circ$ and $Re_c = 100,000$ was again perfomed for this configuration and the results are given in Figure 3.2. In this case, the spanwise uniformity of the flow is improved, but still is not symmetric about

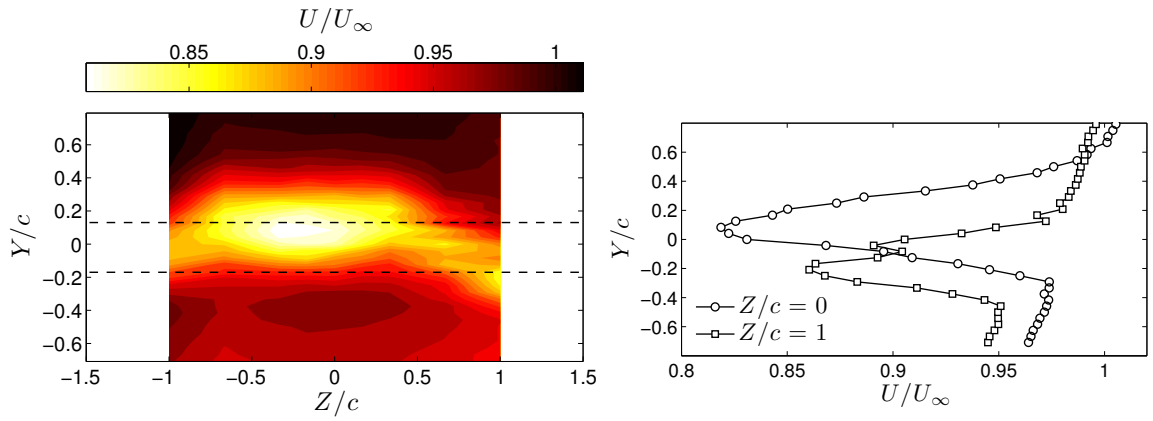

(a) (b)

Figure 3.1: Variation of U over a ZY plane in the wake for $\alpha = 10°$ and $Re_c = 100,000$ with gaps between the model ends and the tunnel walls of $0.025c$. The measurement plane is located $2c$ downstream of the trailing edge and the dashed lines indicate the outline of the model. Select transverse profiles are shown in (b).

midspan. The flow is now stalled over the entire measurement domain, however the wake on the $Z/c = -1.5$ end is shifted down relative to midspan.

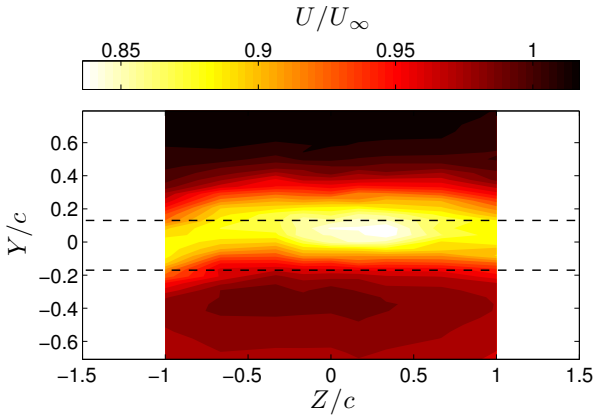

Figure 3.2: Streamwise velocity in the wake with $0.003c$ gaps at the model ends.

These non-uniformities in flow along the span due to the presence of gaps at the ends of the airfoil model motivated the use of the end plates described in Section 2.2. If properly positioned, end plates also allow the model to be isolated from the boundary layers on the wind tunnel walls. A measurement of the boundary layer profile on the tunnel wall at the location corresponding the end plate leading edge showed that the boundary layer was 12 mm thick at $U_\infty = 5.2$ m/s. Therefore, the spanwise length of the model was altered to

$b = 885$ mm such that end plates could be fixed to the ends of the model and positioned 15 mm from the tunnel walls, outside the tunnel boundary layer. The alteration in length was small enough that the aspect ratio remained $b/c = 3$. The spanwise uniformity of the flow was again assessed using measurements of U in the $[Y, Z]$ plane at the same X location, with a larger measurement range covering $-1.3 \leq Z/c \leq 1.3$. The wake velocity was measured for two angles-of-attack at $Re_c = 100,000$, $\alpha = 0°$ and $12°$, where the former corresponds to flow that is attached with an LSB and the latter is a case with stalled flow (determined from midpsan pressure distributions). The results are presented in Figures 3.3 and 3.4. For each α, the use of end plates leads to flow that is relatively uniform along Z and is symmetric about midspan. To quantify the spanwise uniformity, included in each figure is the percent difference in U relative to the midspan profile, $U_{Z=0}$. Despite the corner effects that are observed at the model ends, the difference in U relative to midspan is less than 8% over the entire measurement domain for each case. The stalled flow at $\alpha = 12°$ and $Re_c = 100,000$ will receive further attention throughout this chapter as it will serve as the baseline flow for the control studies. The results in Figure 3.4 show that over the spanwise extent covered by the synthetic jet slot, $-0.49 \leq Z/c \leq 0.49$, the deviation in U relative to midspan is less than 4%.

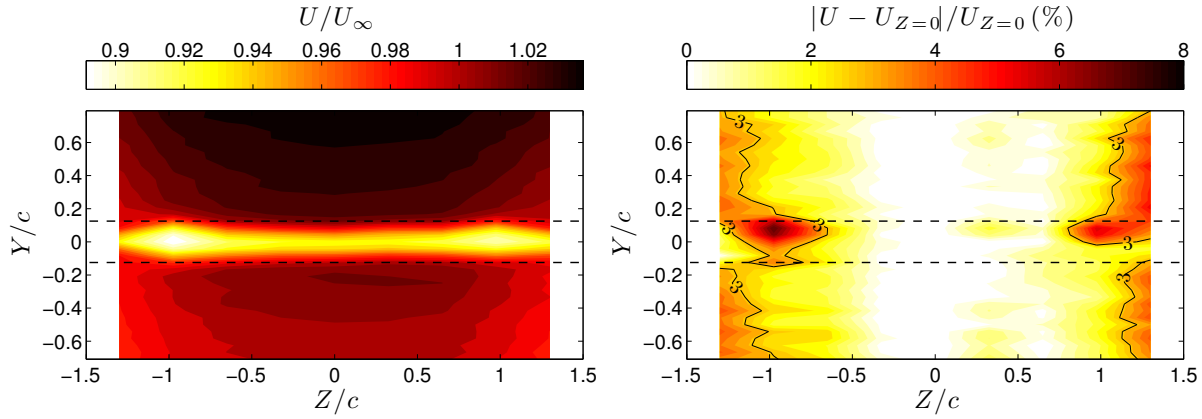

(a) (b)

Figure 3.3: Variation of U over a ZY plane in the wake for $\alpha = 0°$ and $Re_c = 100,000$ with end plates. Contours in (b) show the percent difference in U relative to the profile at midspan, $U_{Z=0}$.

The section lift coefficient at midspan, C_L, was measured over a range of α for the three different end configurations described above; $0.025c$ gaps, $\sim 0.003c$ gaps, and end plates. The section lift coefficient is given by:

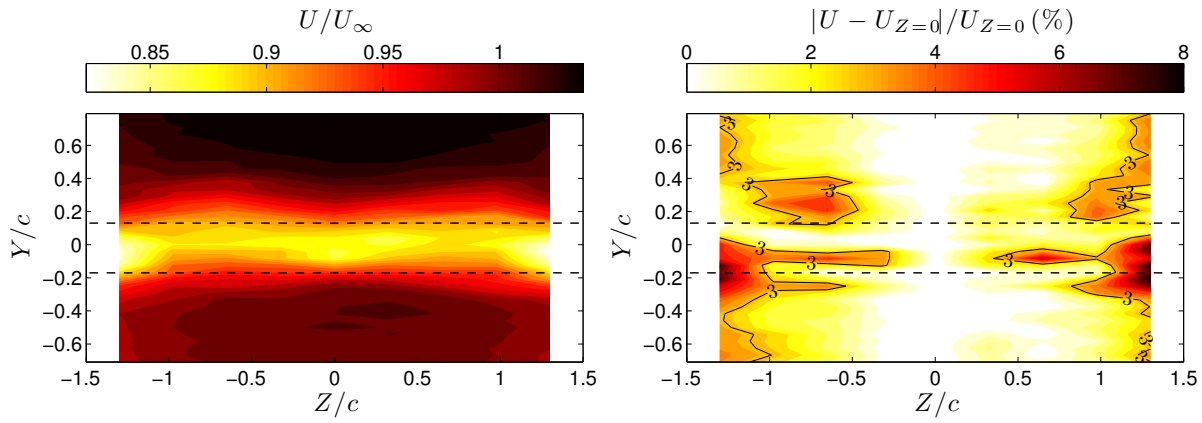

(a) (b)

Figure 3.4: Variation of U over a ZY plane in the wake for $\alpha = 12°$ and $Re_c = 100,000$ with end plates. Contours in (b) show the percent difference in U relative to the profile at midspan, $U_{Z=0}$.

$$C_L = \int_0^c (C_{p,\mathrm{l}} - C_{p,\mathrm{u}})\,\mathrm{d}x, \tag{3.1}$$

where C_p is the pressure coefficient (subscripts 'l' and 'u' indicate the lower and upper, or pressure and suction, sides of the airfoil, respectively),

$$C_p = \frac{\overline{p} - p_\infty}{q_\infty}, \tag{3.2}$$

p is the static surface pressure on the airfoil surface, and p_∞ is the mean freestream static pressure. The freestream static pressure was measured from the static side of the pitot tube used to measure q_∞ at the test section inlet. The C_L results presented in Figure 3.5, with the thin airfoil prediction $C_L = 2\pi\alpha$ included for reference. No wind tunnel corrections were applied since the drag force was not measured, and standard corrections are not considered valid in the post-stall regime. Over $\alpha = 0° - 20°$, the solid blockage based on the projected frontal area varies from 6% to 10%. The case with end plates will be considered as reference. In this case, a maximum C_L of 0.85 is reached at $\alpha = 9°$ prior to stall occurring at $\alpha = 10°$. A plateau in C_L is evident prior to stall. Included in Figure 3.5 is data from Boutilier and Yarusevych [12] at the same Reynolds number on a NACA 0015 airfoil with geometrically similar end plates and an aspect ratio $b/c = 2$. These measurements were performed in a wind tunnel with a freestream turbulence intensity of 0.2%. The results show a similar behaviour of a plateau in C_L prior to stall, however

stall is less severe for this thinner airfoil. A linear increase in C_L at low α is not observed for the NACA 0025 airfoil and is likely a viscous effect due to the low Reynolds number. This is further evidenced by the fact that C_L increases above the thin airfoil prediction over $5° \leq \alpha \leq 7°$.

When gaps are present, the airfoil stalls abruptly at lower angle-of-attack relative to the end plate case. This premature stall occurs at $\alpha = 9°$ for $0.003c$ gaps, and at $\alpha = 6°$ for $0.025c$ gaps and is accompanied by a dramatic reduction in the maximum C_L. These results demonstrate that not only do the gaps cause a spanwise variation in the flow, the disturbances propagate to midspan and cause the flow to prematurely stall. This result is not unexpected due to the highly sensitive nature of the laminar separation bubble present on the suction surface at pre-stall angles-of-attack. These results demonstrating the appreciable effect of model end conditions on the flow are consistent with prior observations of airfoils at low Reynolds number that showed notable sensitivity to experimental conditions [59; 62].

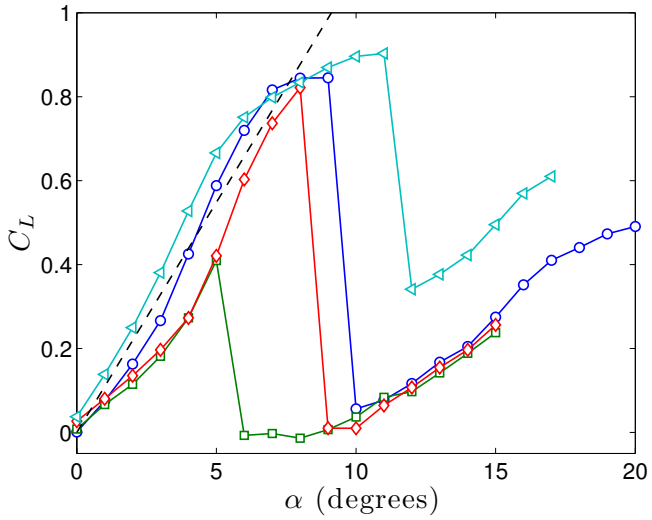

Figure 3.5: Lift polars at $Re_c = 100,000$ for different model end conditions. (○) end plates, (□) $0.025c$ gaps, (◇) $0.003c$ gaps, (◁) data from Boutilier and Yarusevych [12] for a NACA 0015 airfoil with geometrically similar end plates. The dashed line indicates $C_L = 2\pi\alpha$.

The two-dimensionality of the baseline flow with end plates attached was also investigated by measuring the boundary layer variation at $x/c = 0.1$ for $\alpha = 12°$ and $Re_c = 100,000$ (Figure 3.6). The quantity $u'_{\mathrm{t,rms}}$ is defined as the root-mean-square (RMS) magnitude of the velocity fluctuations. This location is upstream of the mean separation point in the laminar boundary layer, as will be discussed in Section 3.3. This

measurement was performed using a single hot-wire that was traversed over the boundary layer height and $-0.5 \leq Z/c \leq 0.5$ with spanwise increments of $\Delta Z/c = 0.017$. The wall-normal increment was $\Delta y/c = 2.5 \times 10^{-4}$. A hot-wire is useful for this type of measurement given its high spatial and temporal resolution, however the primary limitation of a single-wire probe is that it senses the magnitude of the velocity in the plane normal to the sensor. At a given instant, the velocity measured by the hot-wire is:

$$u_{\mathrm{t,tot}}(t) = \sqrt{u_{\mathrm{tot}}(t)^2 + v_{\mathrm{tot}}(t)^2} = \sqrt{u_{\mathrm{s,tot}}(t)^2 + u_{\mathrm{n,tot}}(t)^2} \tag{3.3}$$

where $[u_{\mathrm{tot}}, v_{\mathrm{tot}}]$ is the instantaneous velocity vector in the global coordinate system. This can can also be expressed in wall-attached coordinates as $[u_{\mathrm{s,tot}}, u_{\mathrm{n,tot}}]$, where $u_{\mathrm{s,tot}}$ and $u_{\mathrm{n,tot}}$ are the wall-tangential and wall-normal velocity components. Note that equation (3.3) is valid for a single-wire probe with the wire aligned along the spanwise direction; the velocity component parallel to the wire axis contributes negligibly to the total cooling. The lack of directional sensitivity is an important aspect of single-wire hot-wire measurements and is particularly relevant in regions of separated flow where $U_{\mathrm{t}} \neq U_{\mathrm{s}}$ due to potentially non-negligible mean wall-normal velocity, U_{n}. However, when the flow is attached, such as at $x/c = 0.1$ in Figure 3.6, $U_{\mathrm{t}} \approx U_{\mathrm{s}}$ is a valid approximation. The same cannot be said for the fluctuations measured by the hot-wire, u_{t}, which contains contributions from velocity fluctuations in each direction; that is, the assumption $u'_{\mathrm{t,rms}} \approx u'_{\mathrm{s,rms}}$ is not necessarily valid. The results in Figure 3.6 demonstrate that, consistent with the wake velocity results (Figure 3.4), the boundary layer is uniform along the span both in terms of mean and RMS velocity. The errors in the mean and RMS components in this figure are typically within $\pm 0.02 U_\infty$ and $\pm 0.004 U_\infty$, respectively.

The spanwise variation in boundary layer thickness, δ (where $U_{\mathrm{s}}(\delta) = 0.99 U_{\mathrm{e}}$ and U_{e} is the local edge velocity), displament thickness, δ^*, and momentum thickness, θ, for the flow shown in Figure 3.6 are given in Figure 3.7. The $0.99 U_{\mathrm{e}}$ location for δ was determined by evaluating a spline fit to U_{s}. The displacement and momentum thickness are given by

$$\delta^* = \int_0^\delta \left(1 - \frac{U_{\mathrm{s}}}{U_{\mathrm{e}}}\right) \mathrm{d}y \tag{3.4}$$

and

$$\theta = \int_0^\delta \frac{U_{\mathrm{s}}}{U_{\mathrm{e}}} \left(1 - \frac{U_{\mathrm{s}}}{U_{\mathrm{e}}}\right) \mathrm{d}y. \tag{3.5}$$

The results show that while a minimum near midspan in the integral boundary layer parameters is observed, the variation in each parameter is primarily within $\pm 5\%$ of

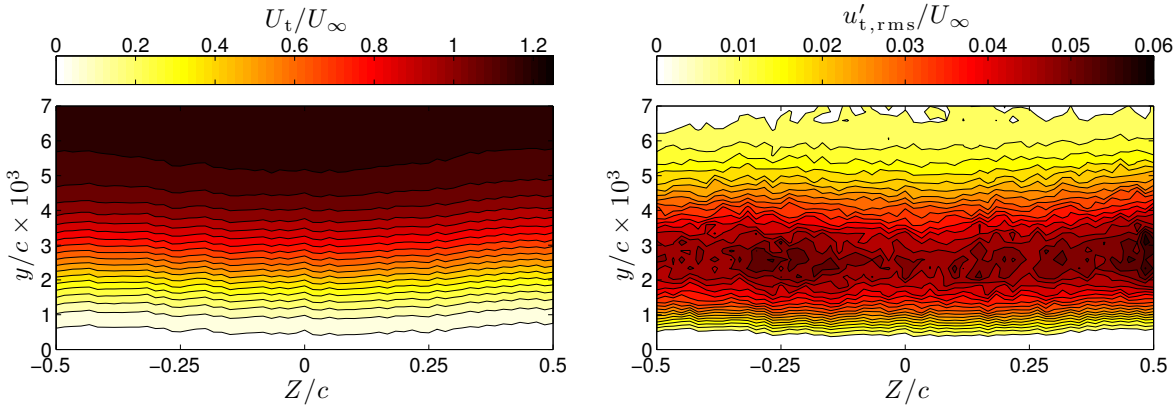

Figure 3.6: Contours of mean and RMS velocity measured by hot-wire in the spanwise/wall-normal plane at $x/c = 0.1$ for $\alpha = 12°$ and $Re_c = 100,000$. The y axes are presented at 70:1 scale for clarity.

the respective spanwise average. The velocity measurements along the span both in the boundary and in the wake presented in this section provide confidence in the two-dimensionality of the baseline flow for subsequent control experiments.

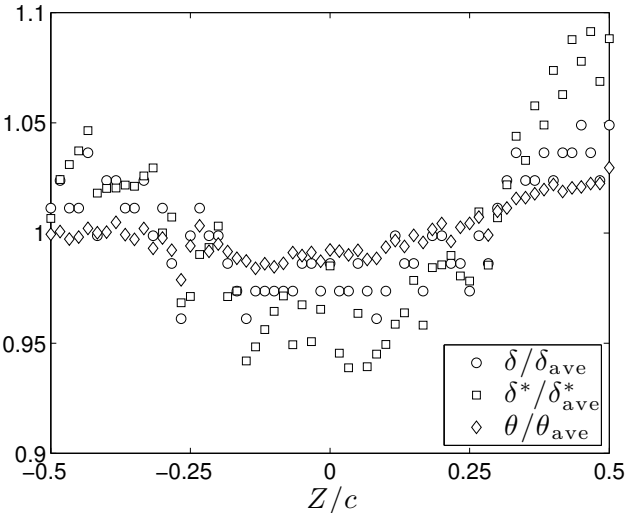

Figure 3.7: Spanwise variation in boundary layer integral parameters for the same conditions as Figure 3.6. The subscript 'ave' indicates a spanwise average. $\delta_{ave}/c = 5.8 \times 10^{-3}$, $\delta^*_{ave}/c = 2.3 \times 10^{-3}$, $\theta_{ave}/c = 7.1 \times 10^{-4}$.

3.2 Midspan: mean flow

This section will describe the features of the time-averaged baseline flow at $\alpha = 12°$ and $Re_c = 100,000$ that was the subject of synthetic jet control experiments. Measurements of surface pressure, boundary layer/separated shear layer velocity using hot-wire, and the global velocity field using PIV were performed.

Figure 3.8 shows the C_p distribution for the baseline flow, where stall is evident by the region of approximately constant pressure on the suction surface that extends from a location after the suction peak to the trailing edge. Details regarding the determination of the mean separation point are discussed in Section 3.3. Relative to a flow that is attached (with or without a LSB), the magnitude of the suction peak is reduced substantially for stalled flow.

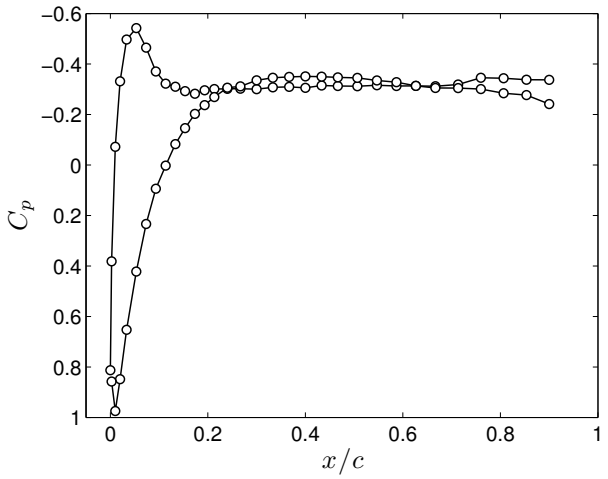

Figure 3.8: Pressure coefficient distribution at midspan for the baseline flow.

Figure 3.9 describes the mean and fluctuating velocity at midspan. Due to the nature of the stalled flow field over the curved airfoil surface at $\alpha = 12°$, the flow has significant contributions from both the streamwise and transverse velocity throughout measurement domain. As such, the magnitude of the mean flow is described by the mean total velocity,

$$U_{\mathrm{T}} = \sqrt{U^2 + V^2}, \tag{3.6}$$

and the fluctuations by the Reynolds shear stress, $\overline{uv}$. As shown in Figure 3.9, the stalled flow is associated with laminar boundary layer separation occurring near the leading edge and the formation of a separated shear layer over the remainder of the airfoil chord. The separated shear layer forms a large region of recirculating flow over the suction surface,

above which the higher velocity outer flow moves in the downstream direction. The Reynolds shear stress shows a rapid growth of fluctuations downstream of separation and reaches a peak of approximately $\overline{uv}/U_\infty^2 = -0.04$ prior to decreasing in the downstream direction at a lower rate.

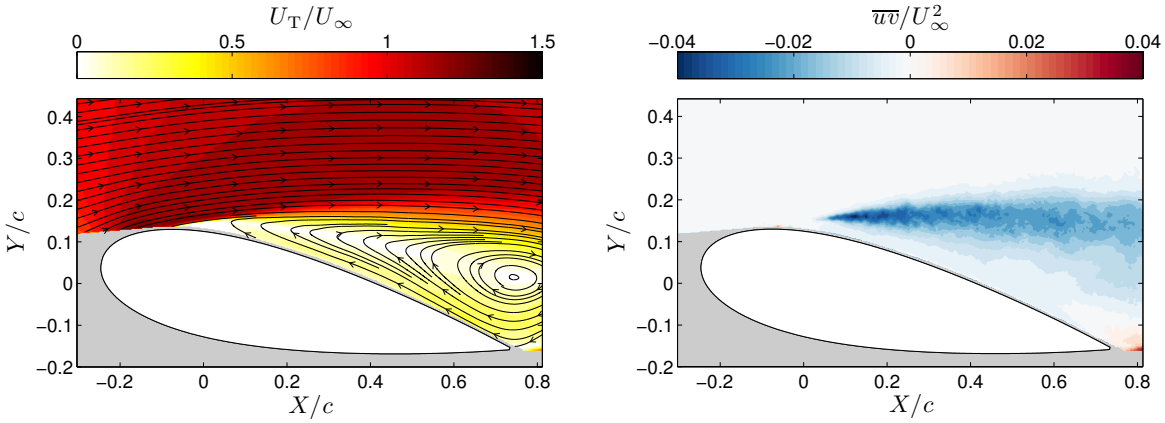

(a) (b)

Figure 3.9: Contours of (a) mean total velocity with mean streamlines overlaid and (b) Reynolds shear stress at midspan for the baseline flow.

Velocity profiles in the separated shear layer from both PIV and hot-wire measurements are shown in Figure 3.10. The wall-normal increment for hot-wire measurements was approximately $\Delta y/\delta = 0.03$ at each chord location, with the first five points having a finer resolution of $\Delta y/\delta = 0.015$. The first velocity vector away from the wall in the PIV velocity fields was at $y/c = 0.008$ ($y = 2.5$ mm). The mean velocity measured the hot-wire, U_t, is a measure of the total velocity, however it is important to note that $U_\mathrm{T} \neq U_\mathrm{t}$. If one takes the time-average of equation (3.3), for the general case this is not equivalent to equation (3.6) due to rectification of velocity fluctuations. The mean velocity components in surface attached coordinates were obtained by transforming U and V measured by PIV:

$$U_\mathrm{s} = U\cos\beta - V\sin\beta, \tag{3.7}$$

$$U_\mathrm{n} = U\sin\beta + V\cos\beta, \tag{3.8}$$

where β is the local surface angle in the global frame of reference. Close agreement between U_t and U_s in the outer part of the boundary layer is observed at $x/c = 0.2$ and

0.3 prior to a substantial change in the shape of U_s occurring at $x/c = 0.4$. Outside of the region of reversed flow, the velocity profiles show similar trends but U_t is consistently larger than U_s for $x/c \geq 0.4$ due to non-negligible wall-normal velocity being measured by the hot-wire. The location of minimum velocity moves closer to the wall as the near wall velocity gradient increases, which is likely indicative of the flow having transitioned to turbulence. The profiles at all chord locations demonstrate that near the region where the flow changes direction, i.e. where U_s crosses zero, U_t does not exhibit the correct shape and appears as a region of approximately constant, low velocity. This is due to U_n, u'_n, u'_s and natural convection effects contributing to U_t. While hot-wire is beneficial for its near wall spatial resolution and high temporal resolution, the inability of a single-wire to resolve velocity components is a significant disadvantage. A cross-wire type probe can be used for measuring two components of velocity, however several factors preclude its use in this experiment: a measurement volume that is too large due to probe orientation, and a valid angular range between velocity components of typically only $\pm 45°$ (i.e. not valid in the presence of reversed flow).

The boundary layer thickness, δ, and integral boundary layer parameters (δ^* and θ) were determined at locations along the airfoil chord from profiles of both U_t (hot-wire) and U_s (PIV). Errors in the quantities determined from PIV were estimated by propagation of the uncertainty in U_s. Since velocity rectification in U_t was expected to have a larger impact than the measurement uncertainty in U_t, errors in the boundary layer parameters determined by hot-wire are evaluated relative to the parameters from PIV. The results in Figure 3.11 show that good agreement is observed in δ determined from U_t and U_s. The displacement thickness follows the same trend for the two measurement techniques, however δ^* determined from U_t is consistently overestimated. Consistent overestimation by 10%–20% in δ^* while following the correct trend has previously been observed in studies of laminar separation bubbles using hot-wire measurements [15; 33]. The chordwise variation in θ shows a significant difference not only in magnitude, but also the trend along x. The momentum thickness from U_t shows constant growth along x, while θ from U_s increases up to a peak at approximately $x/c = 0.7$ before decreasing. The larger error in θ relative to δ^* determined from hot-wire measurements is not surprising since $\delta^* \propto U_s$, while $\theta \propto U_s^2$. This error increases in the downstream direction as the magnitude of the reversed flow increases. Therefore, hot-wire measured velocity profiles can be used to estimate δ^*, but not θ in the presence of highly reversed flow. The error ranges for the boundary layer quantities in Figure 3.11 determined from hot-wire relative to PIV are summarized in Table 3.1.

A shape factor can be defined using the displacement and momentum thicknesses as

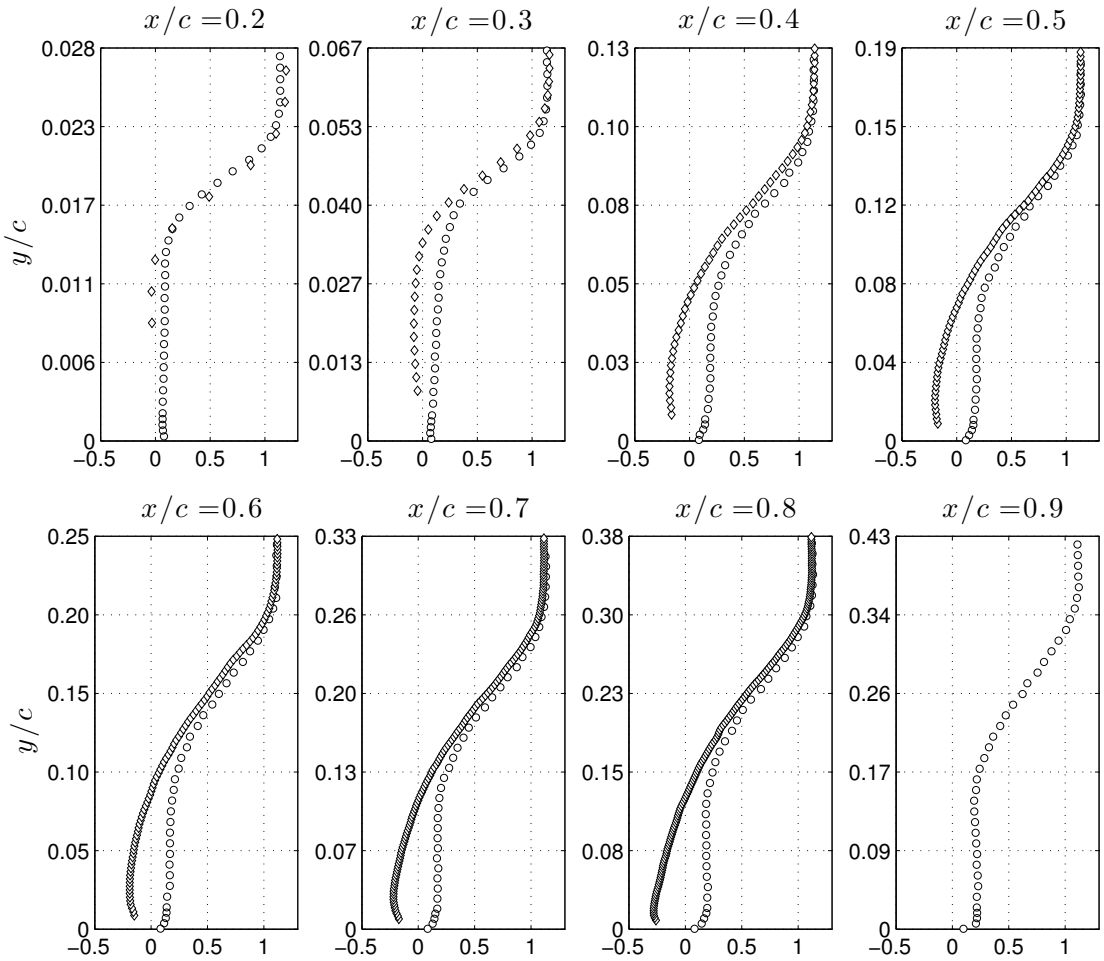

Figure 3.10: Comparison of baseline boundary layer velocity profiles from (○) hot-wire and (◇) PIV measurements at midspan. (○) U_t/U_∞, (◇) U_s/U_∞. The y limit of each plot is fixed at 1.2δ.

Table 3.1: Error in boundary layer quantities computed from U_t (hot-wire) relative to those computed from U_s (PIV) as shown in Figures 3.11 and 3.12. For example, the error in δ is given by $(\delta_{HW} - \delta_{PIV})/\delta_{PIV}$, where the subscripts indicate measurement by hot-wire (HW) and PIV.

	Error range (%)
δ	-7 – -3
δ^*	-22 – -8
θ	87 – 629
δ^*/θ	-89 – -51

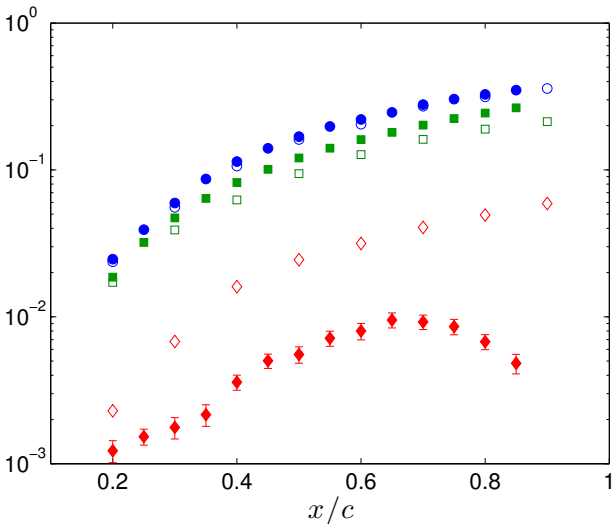

Figure 3.11: Comparison of boundary layer parameters along the airfoil chord determined from U_t (open symbols) and U_s (closed symbols). ($\circ$) δ/c, ($\square$) δ^*/c, ($\diamond$) θ/c. Errors in δ/c and δ^*/c determined from U_s are approximately $\pm 1\%$ or less.

δ^*/θ. This quantity is compared for the hot-wire and PIV boundary layer profiles in Figure 3.12. As expected, there is significant discrepancy both in the magnitude and trend of δ^*/θ determined from U_t. The shape factor from hot-wire initially decreases before reaching a constant value for $x/c \geq 0.4$ due to θ inaccurately following the same trend as δ^*. The proper trend in δ^*/θ determined from U_s shows substantially larger values with δ^*/θ initially increasing to a peak at $x/c = 0.35$. Downstream of this peak, δ^*/θ plateaus over $0.45 \leq x/c \leq 0.65$ before increasing towards the trailing edge. The error range in δ^*/θ determined from hot-wire measurements is included in Table 3.1.

3.3 Midspan: separation point

The four chordwise locations of the synthetic jet slot, discussed in Section 2.3, were selected such that there were two locations upstream, and two downstream of the mean separation point. Symmetric forcing locations about separation were desired and due to model constraints on the most upstream location that was feasible, the slot varies over a range of approximately $0.1c$. As such, accurate knowledge of the relative slot locations requires accurate determination of the mean separation point, x_s. For 2D flow, separation/reattachment points are defined as locations where the wall shear stress is zero. However, wall shear stress is a fundamentally challenging quantity to measure experimentally. This section will discuss several techniques used to estimate x_s without

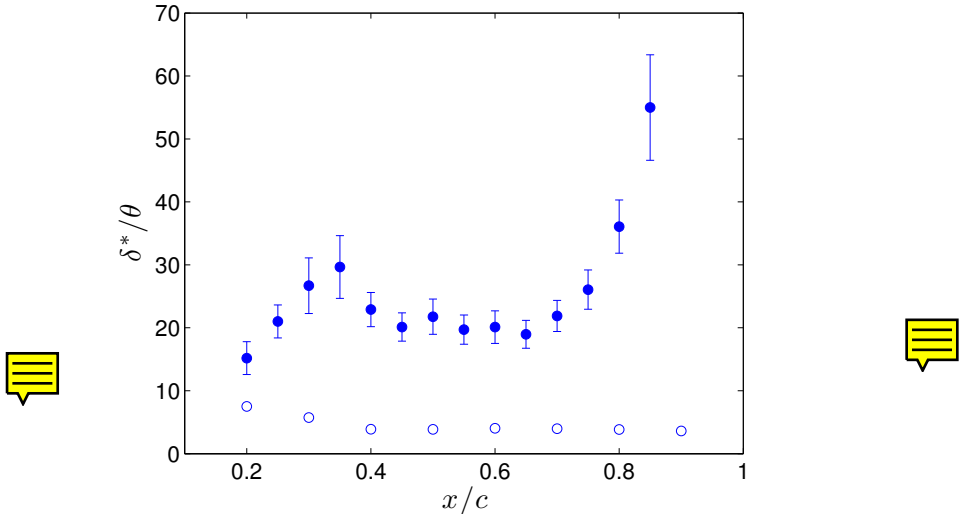

Figure 3.12: Comparison of shape factor along the airfoil chord determined from U_t (open symbols) and U_s (closed symbols).

knowledge of the wall shear stress distribution.

The simplest method used for the estimation of the mean separation point was to identify the beginning of the region of constant pressure on the suction surface from the C_p distribution. Identifying locations where the C_p distribution changes shape is a common method for estimating points of separation, transition, and reattachment (e.g. [63; 12]). Figure 3.13a describes graphically the method used to estimate x_s for the baseline flow at $\alpha = 12°$. The location where $\partial C_p/\partial x \approx 0$ is identified manually and linear fits are applied to several points upstream and downstream of this location. The intersection of these lines is the estimated separation point. The main sources of error in this methodology are the spatial resolution of the pressure taps, and the heuristic choice of the location where C_p is considered to be 'flat'. This method was applied over a range of α, as shown in Figure 3.13b. The plot demonstrates that within uncertainties, x_s follows a smooth trend with increasing α to which a 3rd-order polynomial was fit. From this curve fit, the separation point at $\alpha = 12°$ is estimated as $x_s = 0.13 \pm 0.01$.

Boundary layer velocity profiles measured by hot-wire with $\Delta x/c = 0.01$ spacing were used to estimate the separation point with finer chordwise resolution. Figure 3.14 shows the profiles of U_s/U_e measured over $x/c = 0.1$–0.15. Since the flow is either attached or close to separation, the approximation $U_t \approx U_s$ is considered valid. To overcome the limitation of hot-wire measurements in detecting velocity direction, a curve fit from Dovgal et al. [23] relevant to laminar velocity profiles with an inflection point was applied to the data:

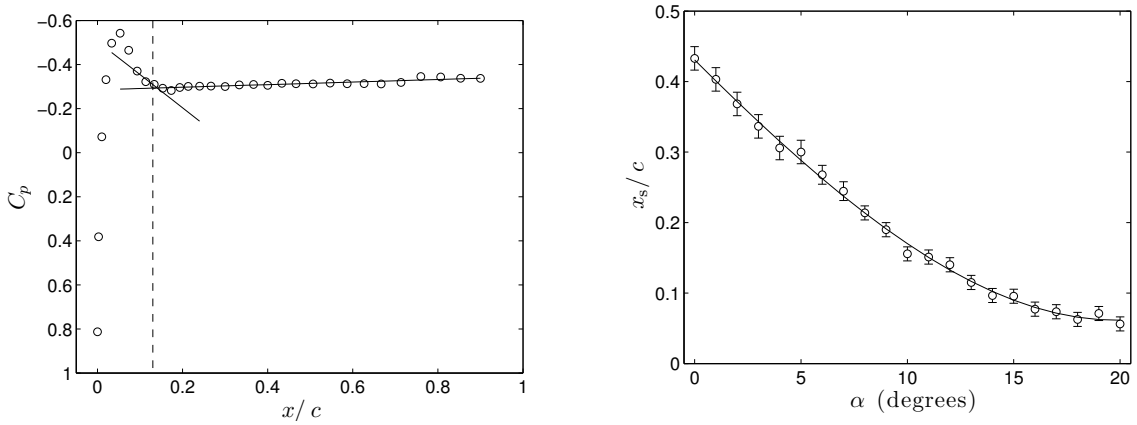

(a) Suction surface C_p distribution at $\alpha = 12°$. The dashed line indicates $x/c = 0.13$.

(b) Separation point variation with α at $Re_c = 100,000$. The line indicates a 3rd-order polynomial fit to the data.

Figure 3.13: Separation point estimation from surface pressure distributions.

$$\frac{U_\mathrm{s}}{U_\mathrm{e}} = \frac{\tanh[\chi_1(y-\chi_2)] + \tanh(\chi_1\chi_2)}{1+\tanh(\chi_1\chi_2)} + \chi_3 \frac{y}{\chi_2} \exp\left[-1.5\left(\frac{y}{\chi_2}\right)^2 + 0.5\right], \tag{3.9}$$

where χ_1, χ_2 and χ_3 are the fit parameters. The $\chi_3 \in [-\infty, 0]$ parameter allows for reversed flow, where $\chi_3 = 0$ without reversed flow. Since data in the region of reversed flow is not correctly measured by the hot-wire (it appears as a region of approximately constant, positive velocity), these points were not included in the fit and these neglected points are indicated in the figure. In addition to this, velocity profiles upstream of separation show the velocity not approaching zero at the wall. This non-physical effect is attributed to radiative heating of the hot-wire due to wall proximity (the first measurement point for each profile was at $y = 100$ μm). Velocities near the wall showing the incorrect trend were omitted. The black lines in Figure 3.14 show the curve fits. From this, at $x/c = 0.13$ the gradient near the wall is observed to be very near zero, and reversed flow is present once $x/c = 0.14$ is reached. Therefore, the mean separation point was estimated as $x_s/c = 0.13 \pm 0.005$, where this uncertainty is due to the spatial resolution of the velocity profiles.

An additional method was employed as an independent validation of the surface pressure and hot-wire methods for determining x_s discussed above. This method defines separation as the location where the mean dividing streamline intersects with the airfoil surface. In a time-averaged sense, this streamline divides the region of recirculating fluid

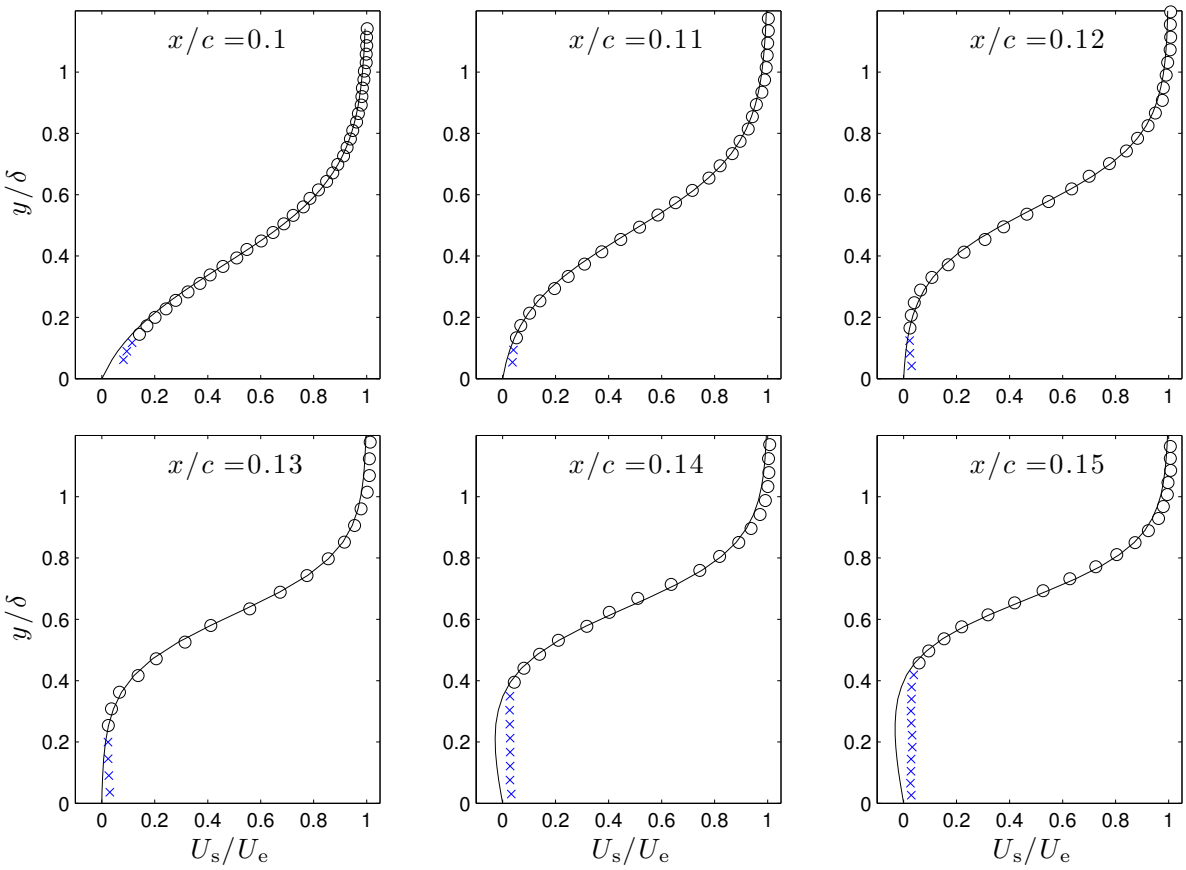

Figure 3.14: Boundary layer velocity profiles in the vicinity of separation measured by hot-wire. The lines show curve fits (equation (3.9)) to the (∘) points, (×) points were not included in the curve fitting procedure. δ increases approximately linearly from $\delta/c = 0.005$ to 0.012 over the streamwise range shown.

and is defined as [33]:

$$\int_0^{y_\mathrm{d}} U_\mathrm{s}\,\mathrm{d}y = 0, \tag{3.10}$$

where y_d is the wall-normal location of the dividing streamline. This quantity was computed from the mean velocity field measured by PIV , which allows accurate determination of U_s. However, as shown in Figure 3.10, the PIV results are limited by spatial resolution and the wall-normal location of the first velocity vector. As such, y_d could only be computed over $x/c \geq 0.2$, as shown in Figure 3.15. The streamline location y_d increases non-linearly in the downstream direction with unknown functional dependance on x. Also provided in Figure 3.15 are the mean flow streamlines with the dividing streamline included, which shows the mean dividing streamline contains the recirculation region. The x location where $y_\mathrm{d} = 0$ was estimated by extrapolating a linear curve fit

over a narrow range of points from $0.2 \leq x/c \leq 0.275$. The fitted linear line gives a separation point of $x_s/c = 0.14$. While the uncertainty associated with the estimation of x_s from a linear extrapolation of y_d cannot be evaluated, the close agreement to the aforementioned techniques serves as validation. The same result was also obtained by linearly extrapolating the zero velocity location where U_s changes direction.

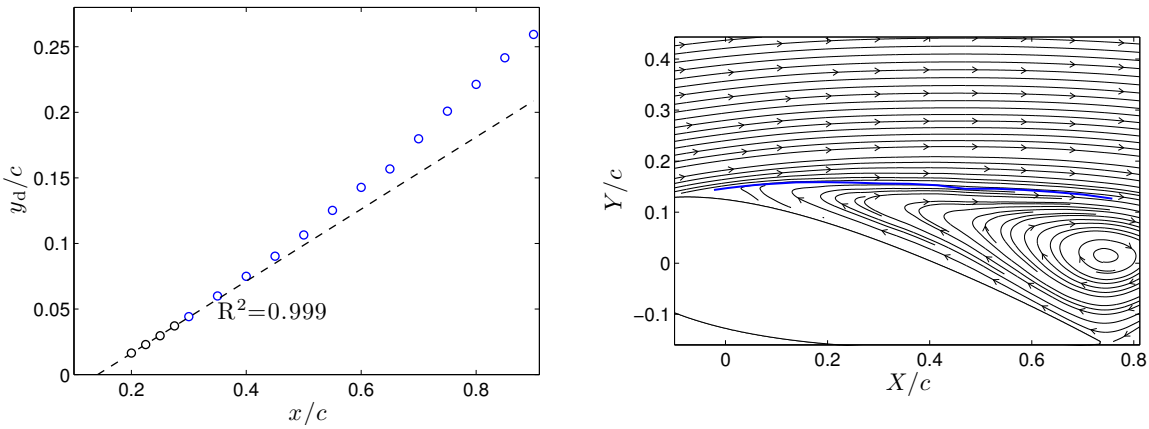

Figure 3.15: (a) Wall-normal location of the mean dividing streamline that encloses the region of recirculating fluid. The dashed line shows a linear fit to the points indicated by black markers and the coefficient of determination R^2 indicates the quality of the fit. (b) Mean streamlines with the dividing streamline shown in blue.

3.4 Midspan: spatiotemporal behaviour

Spatiotemporal characteristics of the baseline flow at $\alpha = 12°$ and $Re_c = 100,000$ were investigated using time-resolved velocity measurements from a hot-wire. Using spectral analysis, the frequencies associated with the shear layer and wake instabilities were identified. Measurements were performed at a sampling rate of 5 kHz, giving a Nyquist frequency of $f^+ = 289$. At a given location, a single measurement was performed and the power spectral density (PSD) was computed by dividing the signal into records with 2^{13} points and 50% overlap, giving a typical resolution in frequency of $\Delta f^+ = 0.07$. Long samples were acquired at each measurement location such that spectra were ensemble averaged from 512 overlapping records. Spectra were computed using Welch's method with a Hamming window to minimize the effects of finite record length.

The velocity spectra, $P_{u_t u_t}$, measured in the boundary layer/separated shear layer

along x/c at $y = \delta^*$ are shown in Figure 3.16. The wall-normal location $y = \delta^*$ matches closely with the location of maximum RMS velocity at each chord location. The spectra are normalized by the respective variance of the velocity signal and are offset in the plot for clarity. The spectra at $x/c = 0.15$ and 0.2 are indicative of laminar flow, however several peaks at $f^+ = 0.7$ and 2.4 are present. The same spectra at $x/c = [0.1, 0.15, 0.2, 0.25]$ are shown non-normalized in Figure 3.17 plotted against frequency. These peaks occur at $f = 12$ Hz and 46 Hz and in particular with the latter peak, it can be observed that its magnitude does not grow along x/c. Once $x/c = 0.25$ is reached, the peak no longer appears as it falls below the level of the spectrum. This result, along with laser vibrometer measurements performed on the hot-wire probe *it situ*, confirmed that these peaks are not physical to the flow but are due to flow induced vibrations of the probe/traverse. At $x/c = 0.2$, a band of frequencies over approximately $f^+_{\mathrm{sl}} = 10 - 26$ emerges and grows in amplitude downstream. The growth of harmonics is also evident at $x/c = 0.225$ and 0.25. At $x/c = 0.35$, the spectrum becomes broadband and shows a spectral shape consistent with turbulent flow. The transition location $x/c = 0.35$ coincides with the peak in δ^*/θ shown in Figure 3.12, which has also been observed for a laminar separation bubble by Burgmann and Schröder [18]. The transition process from laminar to turbulent follows the expected spatial growth of a band of unstable frequencies [23; 85]. The growth of velocity fluctuations observed in the spectra over $x/c = 0.2 - 0.35$ is consistent with the rapid streamwise growth of $-\overline{uv}$ following separation shown in Figure 3.9(b). Spectra at $x/c > 0.4$ are not shown, but maintain a similar turbulent shape.

Time resolved velocity was also measured in the wake to characterize the frequency of the global wake instability, f^+_{w}. The measurement was performed at the wake half-width at a streamwise location $2c$ downstream of the trailing edge, $X/c = 2.73$. Figure 3.18 compares the wake velocity spectrum to the boundary layer velocity spectrum at $x/c = 0.2$. The spectrum in the wake shows a single peak associated with the vortex shedding at $f^+_{\mathrm{w}} = 1$. The results demonstrate the expected order-of-magnitude separation in $f^+_{\mathrm{w}} = 1$ and $10 \leq f^+_{\mathrm{sl}} \leq 26$. Knowledge of the frequencies associated with the natural instabilities of the baseline flow was used to select forcing frequencies that would exploit these instabilities.

3.5 Summary

Features of the baseline flow were discussed in this chapter. The effect of end conditions on the spanwise uniformity of the flow was investigated, and the use of end plates was found to be critical for ensuring approximately two-dimensional flow. The remainder of the

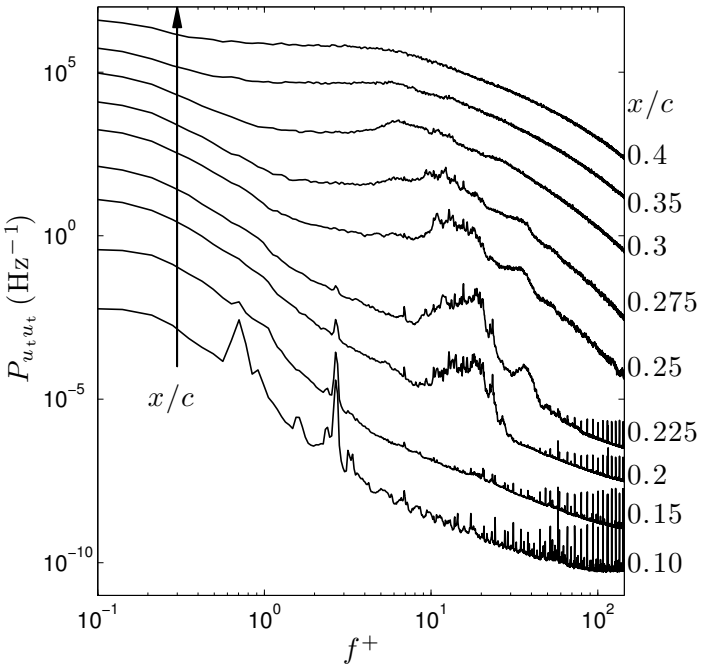

Figure 3.16: Power spectral density of velocity along the airfoil chord measured at $y = \delta^*$. Successive spectra are stepped by an order of magnitude for clarity and x/c locations are specified on the right side of the figure.

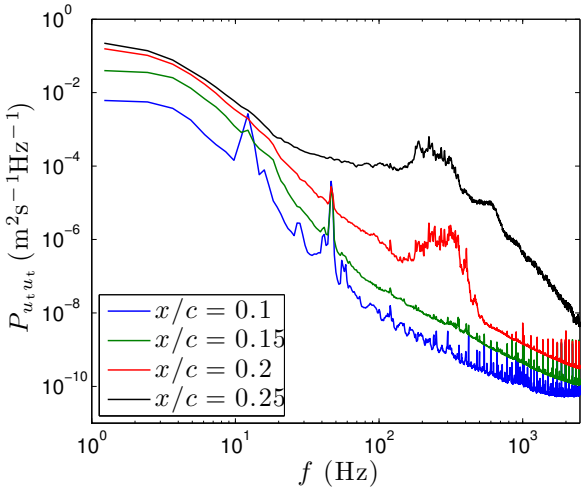

Figure 3.17: Boundary layer velocity spectra plotted against frequency as non-normalized quantities to highlight the behaviour of the extraneous peaks at $f = 12$ Hz and 46 Hz.

chapter focused on characterizing the flow at $Re_c = 100,000$ and $\alpha = 12°$, which served as the baseline for control. Features of the mean flow were described, and in particular the

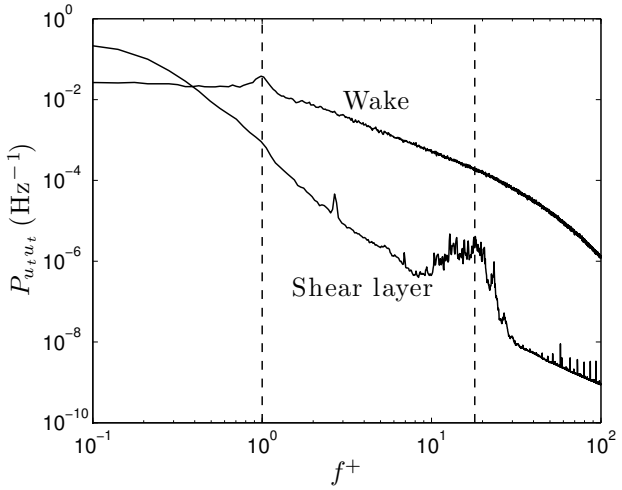

Figure 3.18: Normalized velocity spectra measured in the wake ($X/c = 2.73$ at the wake half-width) and the separated shear layer ($x/c = 0.2$ at $y = \delta^*$) for the baseline flow. Dashed vertical lines indicate $f^+ = 1$ and 18.

mean separation point was determined using several independent techniques. Velocity spectra were also used to identify the frequencies corresponding to the separated shear layer and wake instabilities.

Chapter 4

Synthetic Jet Characterization

The synthetic jet actuator described in Section 2.3 is the result of an iterative design process that had several main goals: mean expulsion velocity that could be increased up to several times that of the freestream velocity ($U_\infty \approx 5$ m/s), operating frequency significantly larger than the frequency range of the baseline flow instabilities, and a uniform velocity profile over the length L of the slot. These goals were accomplished through the optimization of the synthetic jet geometry and the piezoelectric disks used as drivers. This section will discuss the characterization of $\overline{U_\mathrm{j}}$ in regards to excitation frequency and voltage amplitude at the slot centerline, variations in magnitude and phase of the jet velocity along the major axis of the slot, and modulation frequency with fixed duty cycle. A detailed study of these parameters was necessary to have confidence in determining $\overline{U_\mathrm{j}}$ for the control experiments.

The coordinate system used for the synthetic jet benchtop measurements is described in Figure 4.1. The only relevant coordinate for the purpose of these results is ξ, which is located at the center of the minor axis (also referred to as the slot width, $d = 0.5$ mm) where all measurements were performed.

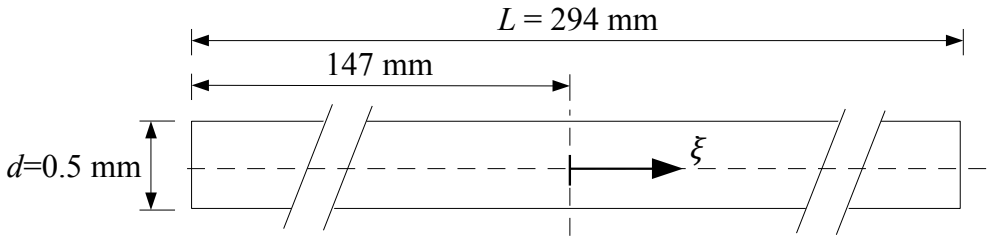

Figure 4.1: Definition of the coordinate ξ along the centerline of the synthetic jet slot major axis.

The time-varying oscillatory synthetic jet velocity along ξ was measured by hot-wire using the setup shown in Figure 4.2. A single-wire probe with its axis aligned with ξ was traversed along this dimension using an automated linear stage. Alignment of the traverse axis with the ξ was measured to be within 0.01 mm in each plane over the entire slot length using a dial test indicator. The height of the synthetic jet off the optical table and the axial distance of the probe from the slot were precisely controlled using manual traverses.

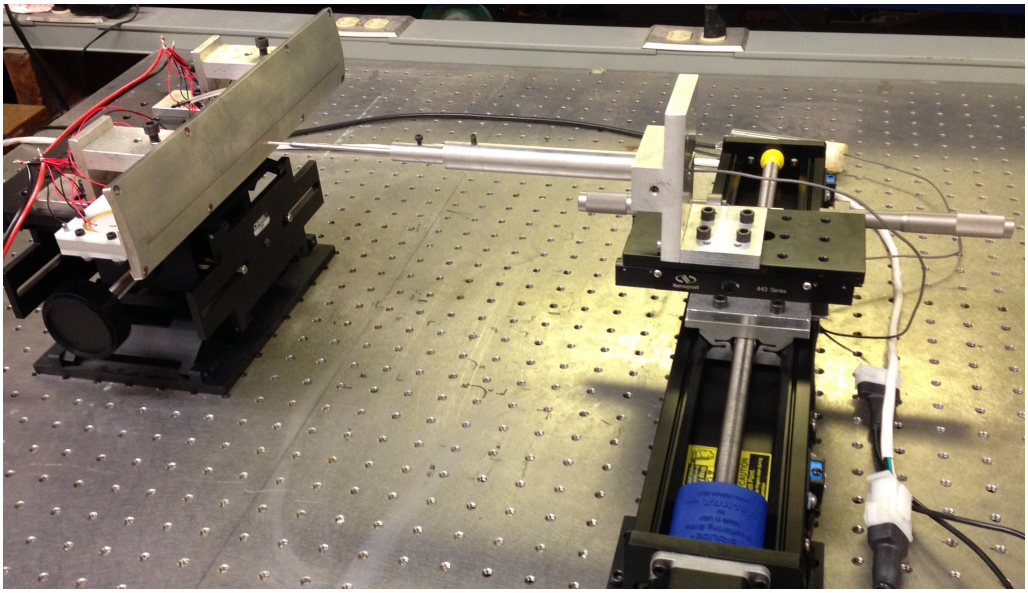

Figure 4.2: Photo of the benchtop setup used to perform hot-wire measurements of synthetic jet velocity.

4.1 Centerline velocity frequency response

The frequency response of the synthetic jet axial velocity, u_j, to a sinusoidal input signal was measured at ξ for a range of excitation frequencies and voltage amplitudes. This was necessary to identify resonant peaks in the response of $\overline{U_\mathrm{j}}$ where the velocity is amplified. Since the jet velocity is rectified by the hot-wire, typical system identification techniques employing frequency sweeps and Fourier analysis cannot be used. Due to rectification, the frequency of the velocity cycle appears doubled relative to the input signal. Thus, the frequency response was measured manually using harmonic excitation over $500 \leq f_\mathrm{e} \leq 2000$ Hz with increments of 50 Hz. At a given frequency, the jet velocity and input signal were sampled simultaneously at 20 kHz and at least 2500 cycles were acquired. A Hilbert transform was used to compute the instantaneous phase of the input

signal, which allowed the entire velocity signal to be sorted according to ascending phase. The sorted signal was then divided into 200 blocks, corresponding to a discretization in phase of 1.8°. The blocks were averaged to give the phase-averaged velocity $\langle u_j \rangle$. A typical example of the phase-averaged jet velocity at $f_e = 1000$ Hz and a voltage amplitude $E = 100$ V (peak-to-peak) is shown in Figure 4.3a, where the control signal is provided for reference. The phase angle, ϕ, is measured relative to the input signal. Two peaks are observed in $\langle u_j \rangle$ that correspond to the maximum expulsion and ingestion velocities. At the exit plane of the jet, these quantities would have the same magnitude if the velocity profiles were symmetric during the expulsion and ingestion portions of the cycle, however this is not necessarily the case [28]. To identify which peak corresponds with expulsion, the axial position of the hot-wire was varied from a location inside the slot to just outside the slot and the hot-wire voltage was monitored on an oscilloscope. Since the ingestion velocity decays much faster in the axial direction than the expulsion velocity [71], the smaller velocity peak at a distance away from the exit plane corresponds to ingestion. The hot-wire was fixed at an axial position where there was a substantial difference in the magnitude of the peaks to avoid ambiguity in identifying the expulsion half of the cycle. The expulsion half-cycle, also shown in Figure 4.3b, was integrated to obtain $\overline{U_j}$ for each value of f_e and E. Based on the measurement uncertainty in $\langle u_j \rangle$, the typical uncertainty in $\overline{U_j}$ is less than 1%.

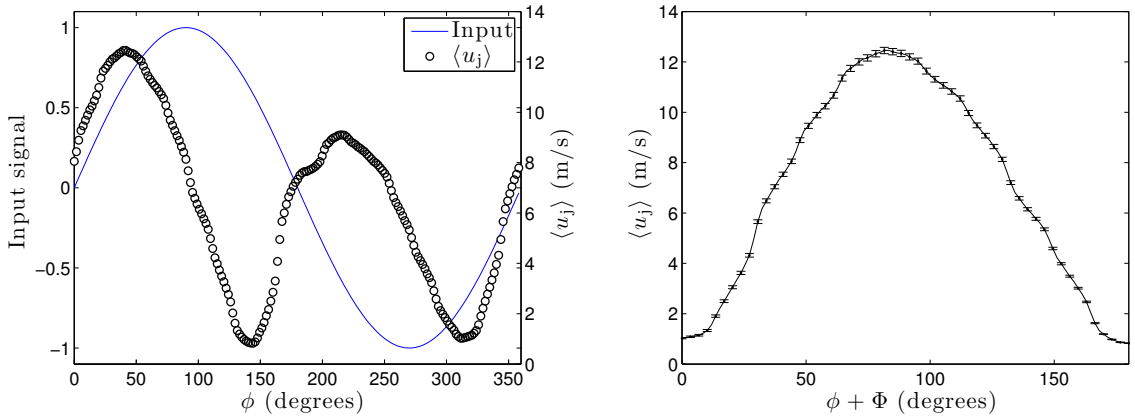

(a) (b)

Figure 4.3: (a) Phase-averaged synthetic jet velocity at $f_e = 1000$ Hz and $E = 100$ V measured at $\xi = 0$. The input signal from the function generator is included for reference. (b) Expulsion half of the velocity cycle, where Φ is the phase offset between $\langle u_j \rangle$ and the input signal.

Figure 4.4 shows the magnitude portion of the mean expulsion velocity frequency

response for $E = 50$ V, 100 V, 150 V and 200 V. Several peaks are observed in the responses, with the first maxima occurring at $f_e = 1000$ Hz. As described by Gallas et al. [36], a simple synthetic jet driven by a piezoelectric diaphragm (i.e. one with a single driver) has been shown to behave as a 4th-order coupled electromechanical-acoustic system, which results in either one or two resonant peaks. These peaks are bounded by the acoustic resonant frequency of the cavity (typically Helmholtz resonance), and the resonant frequency of the piezoelectric diaphragm. The proximity of these frequencies to each other, or the degree of coupling, will dictate whether the velocity response will have two resonant peaks or one merged peak. A more complex frequency response is observed in Figure 4.4 at frequencies above 1000 Hz, which is likely due to the synthetic jet being driven by 16 piezoelectric disks and the unconventionally high aspect ratio of the slot/cavity. The Helmholtz resonant frequency of a cavity connected to a rectangular slot can be estimated by [35]

$$f_H = \frac{1}{2\pi}\sqrt{\frac{5dLa^2}{6h\forall}}, \tag{4.1}$$

where a is the speed of sound in air (assumed to be at 300 K), $h = 5$ mm is the slot height and $\forall = 4.81 \times 10^4$ mm^3 is the cavity volume. The Helmholtz frequency is $f_H = 1200$ Hz according to equation (4.1). Therefore, the first resonant peak in the response at $f_e = 1000$ Hz is expected to correspond to the acoustic resonance of the cavity. Equation (4.1) may not strictly apply for the high aspect ratio geometry under consideration, which would account for a resonant peak in $\overline{U_j}$ occurring slightly below 1200 Hz.

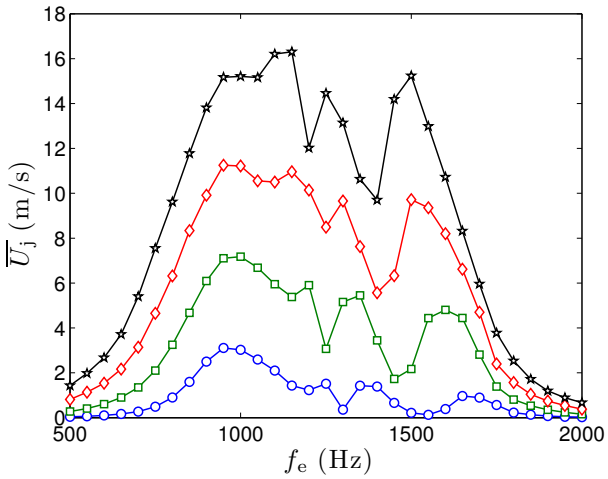

Figure 4.4: Mean expulsion velocity magnitude response measured at $\xi = 0$. ($\circ$) $E = 50$ V, ($\square$) $E = 100$ V, ($\diamond$) $E = 150$ V, ($\star$) $E = 200$ V.

The operating frequency of the synthetic jet for control experiments was selected to be $f_e = 1000$ Hz since mean expulsion velocities up to approximately 16 m/s were possible at this frequency, and as will be discussed in the forthcoming section, this frequency led to a relatively uniform profile along the slot major axis. At $f_e = 1000$ Hz, a detailed calibration of the variation of $\overline{U_j}$ with E was performed. This calibration was done each time the synthetic jet was changed to install a new slot. The voltage amplitude was varied over either $20 \leq E \leq 200$ V or $20 \leq E \leq 180$ V in increments of 20 V, which produced $\overline{U_j}$ up to ~ 16 m/s for all synthetic jet configurations. The calibration results for each of the slot locations specified in Section 2.3 are shown in Figure 4.5. In general, $\overline{U_j}$ increases non-linearly with voltage amplitude and the shape of the curve differs slightly for each configuration. A function that relates the desired $\overline{U_j}$ to the necessary E for the control experiments was obtained by fitting a 4th-order polynomial to the calibration data for a particular slot configuration, where the polynomial meets the physical constraint $\overline{U_j} = 0$ at $E = 0$ (i.e. a polynomial regression model with the constant term set to zero). The order of the polynomial was selected to be four as it was the lowest order polynomial that provided a good fit for each case. The curve fits were used to evaluate E over $\overline{U_j} = 0$ up to the maximum velocity in the calibration data. It is worthwhile to point out that these four calibration curves were obtained over a time span of approximately one year where no alterations were made to the cavity assembly portion of the synthetic jet, only the slot insert was changed. Over this long time period with extended use in experiments, no substantial degradation in jet velocity was observed.

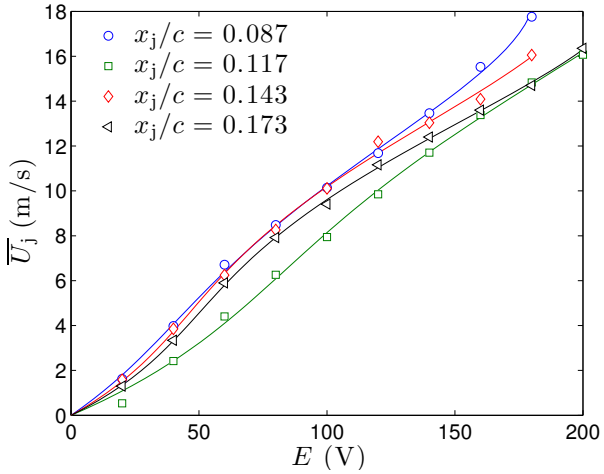

Figure 4.5: Calibration of $\overline{U_j}$ as a function of E at $f_e = 1000$ Hz for each of the four synthetic jet slot configurations. The lines are 4th-order polynomial curve fits to the data of corresponding color.

4.2 Major axis velocity profile

The goal of the synthetic jet was to provide essentially a uniform 2D input over the slot length, thus the velocity profile along the slot major was measured throughout the design process. An initial design sought to maximize jet velocity by designing the cavity and piezo diaphragms to have closely matched resonant frequencies, since this is expected to produce a single peak in the velocity response of larger magnitude than with two distinct peaks [36]. Piezoelectric diaphragms with natural frequency $f_\mathrm{d} = 1400 \pm 300$ Hz were selected and the geometry of the synthetic device was designed for Helmholtz resonance at $f_\mathrm{H} \approx 1450$ Hz. This initial design was driven by only eight piezo disks located on one cavity wall. The velocity characterization results are summarized in Figure 4.6. The frequency response of $\overline{U_\mathrm{j}}$ shows the expected merging of resonant peaks to produce velocities substantially larger than in Figure 4.4 for a given voltage amplitude. The response in this case shows substantial non-linearity with voltage amplitude, which may be due to a dependance of f_d on E. Figures 4.6b and 4.6c show the variation in $\overline{U_\mathrm{j}}$ and the phase offset between u_j and the input signal, Φ, along the slot major axis. The subscript 'ave' for quantities related to the jet velocity denotes a mean over ξ. For $f_\mathrm{e} = 1450$ Hz and 1600 Hz, the jet velocity is highly non-uniform in both magnitude and phase along the length of the slot. The velocity magnitude varies over a particularly wide range of $0.1 \leq \overline{U_\mathrm{j}}_\mathrm{ave} \leq 3.4$ for $f_\mathrm{e} = 1600$ Hz. The velocity variations are not limited to magnitude, as Φ fluctuates up to approximately $\pm 180°$. The cause of this unwanted non-uniformity in jet velocity was investigated by considering the effects of piezo diaphragms operating at different amplitude or phase. It was determined that the results in Figure 4.6 are likely the result of operating the piezo diaphragms very near resonance. Due to manufacturing tolerances, the piezo diaphragms do not have identical resonant frequencies ($f_\mathrm{d} = 1400 \pm 300$ Hz). This may be exacerbated by slight differences in the clamping conditions of individual piezos when installed in the synthetic jet. Therefore, when operating at a frequency near the nominal f_d, each piezo may be operating at substantially different phase since a phase shift of 180° occurs at resonance. Additional testing showed that compared with amplitude differences, having significant phase difference between individual piezos cause dramatic non-uniformities in jet velocity.

The insights gained from testing of the initial synthetic jet led to a new design objective where $f_\mathrm{H} << f_\mathrm{d}$ and the jet would be designed to operate at acoustic resonance. In this way, the issues associated with resonance of the piezo diaphragms would be avoided. New piezos were selected with $f_\mathrm{d} = 2075 \pm 75$ Hz, which was confirmed *in situ* using laser vibrometer measurements on eight different piezos. Although the volume displacement is

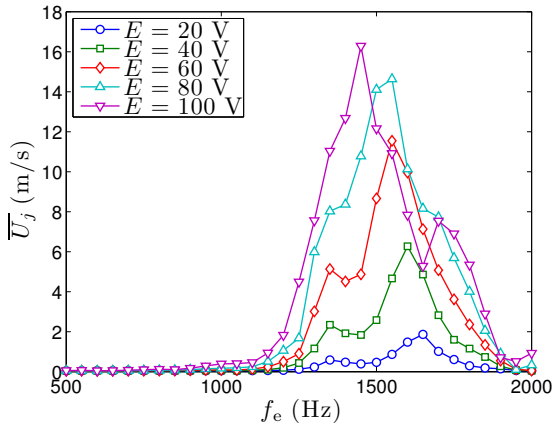

(a) Magnitude response of mean expulsion velocity at $\xi = 0$.

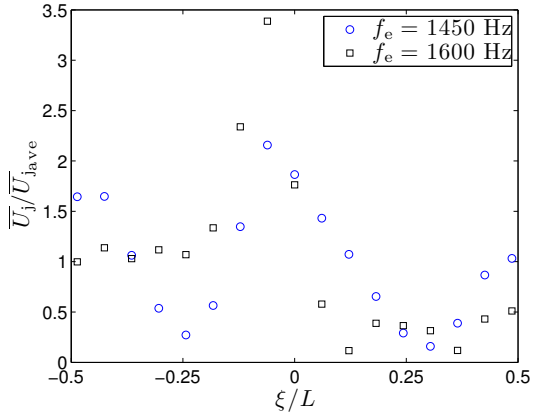

(b) Velocity magnitude variation along the slot major axis.

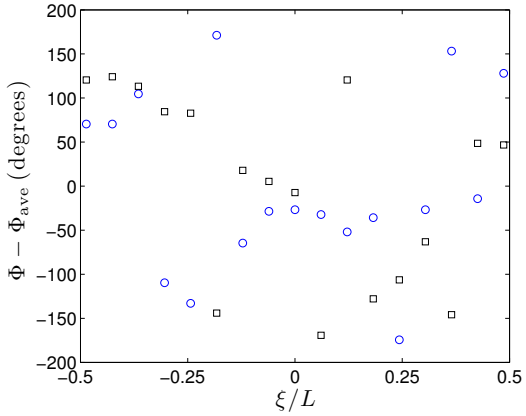

(c) Velocity phase (relative to the input signal) variation along the slot major axis.

Figure 4.6: Characterization of the initial synthetic jet design with $f_H = 1450$ Hz and $f_d = 1400$ Hz.

doubled by using 16 piezos with this design, uncoupling the acoustic and diaphragms resonant frequencies had a substantial effect on the expulsion velocity that can be achieved (Figure 4.4). However, the benefit of operating well below f_d at acoustic resonance is a velocity profile along the major axis that is relatively uniform, as shown in Figure 4.7 for several voltage amplitudes at $f_e = 1000$ Hz. The mean expulsion velocity is shown to vary within approximately $\pm 15\%$ of the mean, with the majority of the variation along ξ being within $\pm 10\%$. Similarly, the phase uniformity is increased to within $\pm 10°$ over the majority of the slot. The velocity profile along the slot length was deemed to be acceptably uniform for control experiments based on these results. The quantity used when computing C_B was $\overline{U_{j_{ave}}}$, which is related to the centerline velocity (the location of

the calibration measurements shown in Figure 4.5) by $\overline{U}_{\mathrm{j}_{\mathrm{ave}}} \approx 1.1\overline{U}_{\mathrm{j}_{\xi=0}}$. It was assumed that the velocity profile along the minor axis (slot width) is uniform during expulsion (similar to Greenblatt et al. [42]) and thus $\overline{U}_{\mathrm{j}_{\mathrm{ave}}}$ represents the temporally and spatially averaged expulsion velocity.

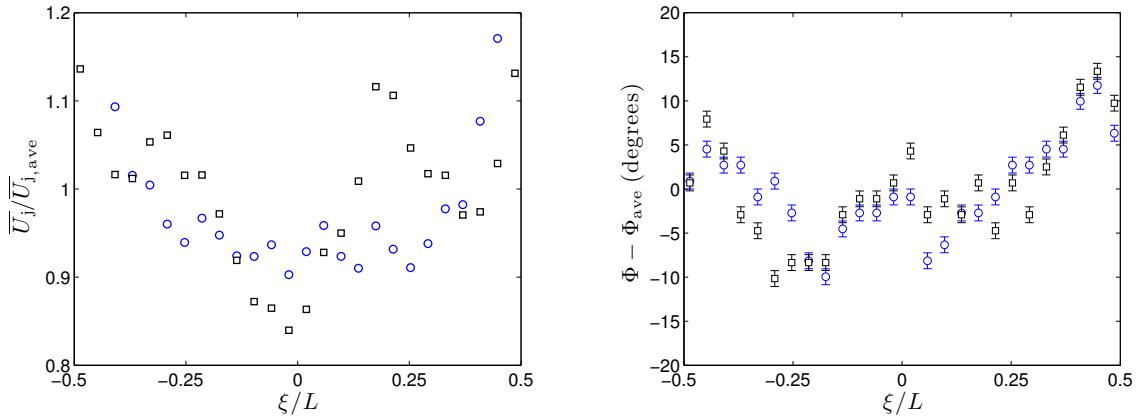

(a) (b)

Figure 4.7: Variation of synthetic jet velocity magnitude and phase along the slot major axis at $f_{\mathrm{e}} = 1000$ Hz. (○) $\overline{U}_{\mathrm{j}_{\mathrm{ave}}} = 7.3$ m/s, (□) $\overline{U}_{\mathrm{j}_{\mathrm{ave}}} = 12.0$ m/s.

4.3 Burst modulated excitation

The nominal excitation frequency $f_{\mathrm{e}} = 1000$ Hz corresponds to a reduced frequency $F^+ = 58$ at $Re_c = 100,000$ and $c = 300$ mm for the present wind tunnel experiments. From the frequency response seen in Figure 4.4, it is clear that simple harmonic excitation at lower frequencies will not produce jet velocities of sufficient amplitude. To achieve reduced frequencies of $F^+ \approx 1$ and $F^+ \approx 10$, burst modulation (i.e., modulation by a square wave varying between 0 and 1) at a frequency f_{m} of a carrier sinusoid at $f_{\mathrm{c}} = 1000$ Hz was employed. The duty cycle was fixed at 50% and the modulation frequency was selected to produce an integer number of carrier waves per cycle. Phase was matched such that there were no partial cycles. Examples of the input control signal using burst modulation are shown in Figure 4.8. For consistency between experiments at $F^+ = 58$ and those at lower F^+ using burst modulation, $\overline{U}_{\mathrm{j}}$ is always defined as the mean over the expulsion half of the 1000 Hz carrier wave. Therefore, the relative velocity amplitude (C_{B}) remains constant. Note that when burst modulation is employed, F^+ is defined based on the modulation frequency, f_{m}.

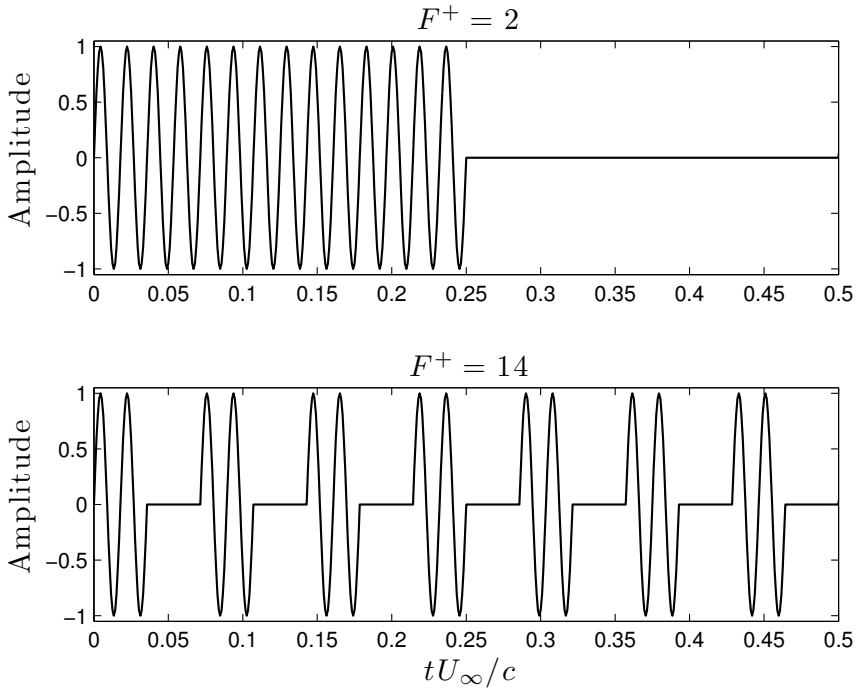

Figure 4.8: Example burst-modulated control signals with $f_c = 1000$ Hz and 50% duty cycle. The signals are presented per unit time relative to the flow for the wind tunnel experiments with $U_\infty = 5.2$ m/s and $c = 300$ mm.

An important aspect of the SJA characterization is the effect of burst modulation on the jet velocity. In particular, characterizing the effect of modulation frequency on the expulsion velocity. The finite number of carrier waves per cycle may result in transient behaviour due to the response time of the system. This was investigated by measuring the velocity using the same hot-wire setup described in Section 4.1. Figure 4.9 shows two examples of the phase-averaged synthetic jet velocity with burst modulation at $E = 100$ V, carrier frequency $f_c = 1000$ Hz and two modulation frequencies $f_m = 50$ Hz and 167.7 Hz (10 and 3 pulses per cycle, respectively). At $f_m = 50$ Hz, transients are observed at the beginning of the cycle and $tf_m \geq 0.5$ due to the starting and stopping of the sinusoidal pulses. This effect is more pronounced for $f_m = 166.7$ Hz where there are less carrier waves per cycle.

The important aspect of this transient behaviour for the purpose of control is the effect on $\overline{U_j}$. The results in Figure 4.9 demonstrate that as f_m increases, the maximum $\langle u_j \rangle$ reached during the cycle is reduced. The same is true of $\overline{U_j}$, which is defined using the sinusoidal wave with the maximum $\langle u_j \rangle$. This effect was quantified for the range of voltage amplitudes and modulation frequencies used in the control experiments: $10 \leq E \leq 200$

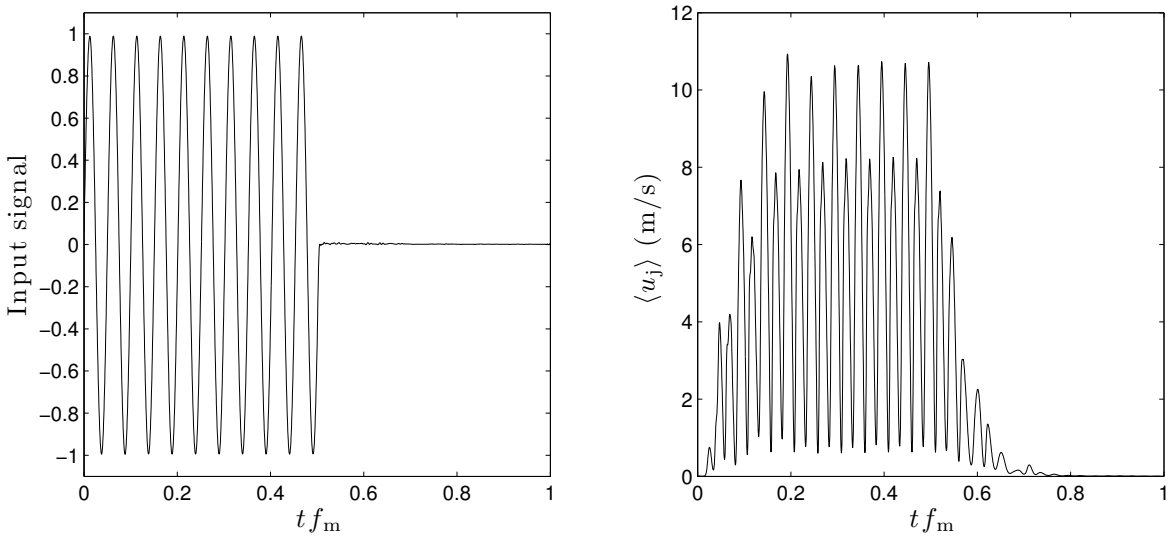

(a) $f_\mathrm{m} = 50$ Hz

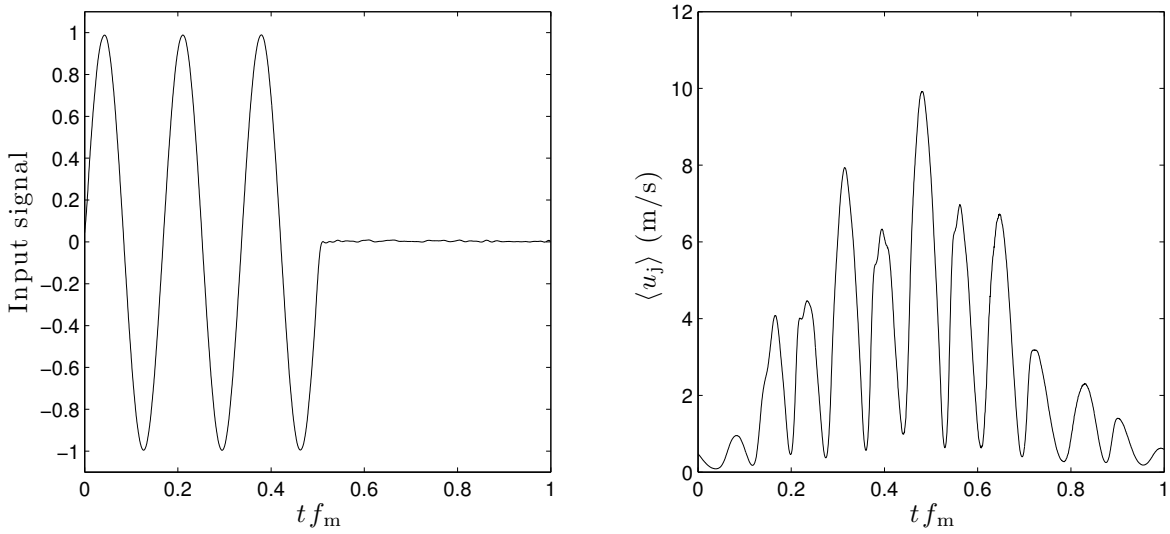

(b) $f_\mathrm{m} = 166.7$ Hz

Figure 4.9: Phase-averaged synthetic jet velocity measured by hot-wire with burst modulated excitation at $f_\mathrm{c} = 1000$ Hz and $E = 100$ V.

V and $10 \leq f_\mathrm{m} \leq 250$ Hz. A mapping function relating the jet velocity at a given E and f_m to the velocity with no modulation ($f_\mathrm{m} = 0$) was defined:

$$VR = \frac{\langle u_\mathrm{j} \rangle_\mathrm{max}(f_\mathrm{m},\, E)}{\langle u_\mathrm{j} \rangle_\mathrm{max}(0,\, E)} \equiv \frac{\overline{U_\mathrm{j}}(f_\mathrm{m},\, E)}{\overline{U_\mathrm{j}}(0,\, E)}, \tag{4.2}$$

where $\langle u_\mathrm{j} \rangle_\mathrm{max}$ is the maximum jet velocity in a phase-averaged cycle. This modulation ve-

locity ratio VR is shown in Figure 4.10. The effect of f_{m} on the velocity ratio is relatively small with variations of approximately $\pm 10\%$ at large voltage amplitudes $E > 125$ V. Substantial reductions in the maximum expulsion velocity are observed with increasing f_{m} at lower voltages. At $E = 10$ V, the velocity is reduced to approximately 25% of that without modulation. A cubic spline surface fit to the modulation velocity ratio was used in conjunction with the calibrations curves measured with harmonic excitation (Figure 4.5) to determine the necessary E for a desired $\overline{U_{\mathrm{j}}}$ at a given modulation frequency. This ensured consistency in $\overline{U_{\mathrm{j}}}$, and therefore C_{B}, over the entire range of F^{+} tested.

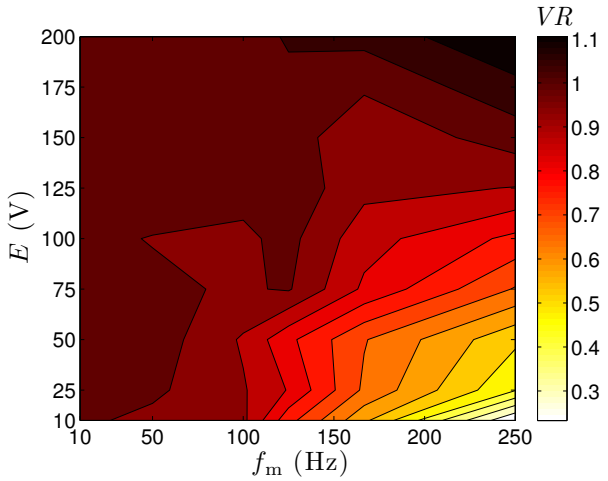

Figure 4.10: Contours of modulation velocity ratio as a function of voltage amplitude and modulation frequency at 50% duty-cycle.

4.4 Summary

This chapter showed a detailed bench-top characterization of the synthetic jet. The frequency response of the jet velocity was used to identify resonant peaks and select a frequency that would maximize the achievable jet velocity. In addition to this, measurements along the major axis of the high aspect ratio slot were critical to ensure an axial velocity profile that could be considered approximately uniform. A strong dependance of this velocity profile on forcing frequency was observed. The effect of burst modulating the harmonic signal at various frequencies and voltage amplitudes on the jet velocity was also quantified. The results in this chapter provide confidence that the forcing input provided by the synthetic jet in the control experiments was well defined.

Chapter 5

Control Parameter Study

This chapter will discuss the results of the open-loop control on the baseline flow described in Chapter 3 using the synthetic jet whose velocity characterization was detailed in Chapter 4. Important parameters relating to the baseline flow are summarized in Table 5.1.

Table 5.1: Important baseline flow parameters at $Re_c = 100,000$ and $\alpha = 12°$. Note that the separated shear layer instability corresponds to a range of amplified frequencies rather than a single value.

Description	Symbol	
Freestream velocity (typical)	U_∞	5.2 m/s
Separation point	x_s/c	0.13
Wake frequency	f_w^+	1.0
Separated shear layer frequency	f_{sl}^+	18 ± 8

The three control parameters that were varied are excitation amplitude, characterized by C_B, frequency, F^+, and the chordwise location of the slot, x_j. Specifically, the location relative to separation was of interest and is defined as $x_j^* = (x_j - x_s)/c$. The values of each parameter for the majority of the experiments are summarized in Table 5.2. For a given F^+ and x_j^*, a range of C_B was considered up to a maximum of $C_B = 3$. Four different F^+ were selected based on the dynamics of the baseline flow: $F^+ = 1$, 2, 14 and 58. $F^+ = 1$ corresponds to forcing the flow at f_w^+, and $F^+ = 2$ is the first harmonic of this frequency. To target the shear layer instability, f_{sl}^+, $F^+ = 14$ was selected. Although the central frequency of f_{sl}^+ is 18, $F^+ = 14$ corresponds to $f_m = 250$ Hz, which was the highest modulation frequency where there were at least two carrier waves per cycle at 50% duty-cycle. Finally, $F^+ = 58$ (harmonic excitation at $f_e = 1000$ Hz) was employed as the 'high-frequency' control strategy since at this frequency, the synthetic jet is essentially time-invariant relative to the time scales of the flow. As discussed in

Section 2.3, $x_{\mathrm{j}}^* = -4.3\%$ was the most upstream location where the jet could be installed. A location 'just upstream' of separation was selected as $x_{\mathrm{j}}^* = -1.3\%$. The remaining two slot locations were selected to be symmetric about the separation point.

Table 5.2: Control parameter ranges at $Re_c = 100,000$ and $\alpha = 12°$.

Description	Symbol	
Blowing ratio	C_{B}	0 – 3
Reduced frequency	F^+	1, 2, 14, 58
Relative slot location	x_{j}^*	-4.3, -1.3, 1.3, 4.3%

5.1 Aerodynamic performance

Aerodynamic performance was assessed by midspan surface pressure distributions, section lift, C_L, and section drag, C_D, coefficients that were measured as a function of C_{B}, F^+ and synthetic jet slot location. The section drag coefficient was computed using a control volume approach [77; 4], *viz.*

$$C_D = -\frac{2}{U_\infty^2 c}\int_{-\infty}^{\infty}[U(U-U_\infty)+(\overline{uu}-\overline{vv})]\,\mathrm{d}Y \approx -\frac{2}{U_\infty^2 c}\int_{-\infty}^{\infty}U(U-U_\infty)\,\mathrm{d}Y. \qquad (5.1)$$

This formulation varies slightly from that of Antonia and Rajagopalan [4] in that mass conservation is strictly imposed across the control volume boundaries, as recommended for wing-like bodies by van Oudheusden et al. [78]. The simplification of ignoring the Reynolds stress term was made since often $\overline{uu} \approx \overline{vv}$, which was shown to be the case at a plane $2c$ downstream of the trailing edge in previous work by the author [26]. The difference between C_D determined with and without the Reynolds stress term for both attached and stalled flow at $\alpha = 10°$ and $Re_c = 100,000$ was found to be less than 3%. This is a useful result as the mean streamwise velocity can be easily and accurately measured by traversing a static-pitot tube (or using a rake of pitot-static tubes), while obtaining the Reynolds normal stresses would require a more complex measurement instrument (e.g., cross-wire, LDA, etc.). Therefore, C_D was computed from profiles of $U(Y)$ measured $2c$ downstream of the trailing edge by traversing a pitot-static tube. This streamwise measurement location is consistent with other studies concerning thick airfoils at low Re_c under stalled conditions [56; 66].

The lift and drag coefficients for the controlled flow are compared to the baseline values; $C_{Lo} = 0.135 \pm 0.004$ and $C_{Do} = 0.105 \pm 0.005$. These error bounds represent

the variation in C_{Do} and C_{Lo} due to changing the slot location. Typical measurement uncertainties in C_L and C_D are ± 0.001 and ± 0.003, respectively. Therefore, changing the synthetic jet slot location had no appreciable effect on the baseline flow. In addition to comparing the unforced flow for the four different slot configurations, a measurement was performed to ensure the presence of the $d/c = 0.0017$ wide slot did not passively alter the baseline flow due to the small change in geometry. The surface pressure distribution was measured with the slot at $x_j/c = 0.117$ in two configurations: the slot covered with a piece of ~ 0.04 mm thick tape (to simulate the model surface with no slot), and the slot open with no forcing. The results in Figure 5.1 show that the presence of the open slot does not affect the mean flow. The difference in C_L between these two cases is well below the measurement uncertainty in C_L (i.e. < 0.001).

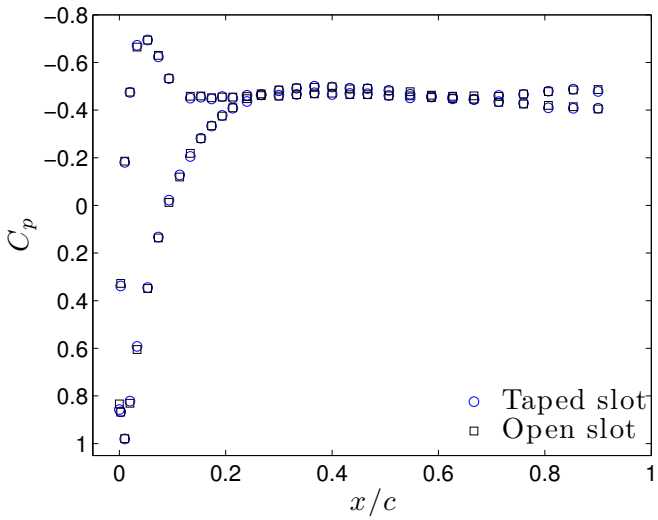

Figure 5.1: Comparison of C_p for the baseline flow with the synthetic jet slot at $x_j/c = 0.117$ open (no forcing), and covered with a thin piece of tape.

Figures 5.2 and 5.3 show the change in C_D and C_L, respectively, relative to the baseline values as a function of the control parameters. The general, and expected, trend that is observed in both C_D and C_L for all F^+ and x_j^* is that increasing C_B initially has a positive effect, but this effect saturates at a C_B that depends on both frequency and slot location. Furthermore, forcing at $F^+ = 1$, 2 or 14 is more effective than $F^+ = 58$ as a substantial lift increase/drag decrease is observed even at the lowest blowing ratios of $C_B \approx 0.1$. While forcing at $F^+ = 1$ or 2 leads to the largest lift increment, drag is reduced to a greater extent with $F^+ = 14$ or 58. As the slot is moved from the most upstream location $x_j^* = -4.3\%$ to $x_j^* = 1.3\%$, the blowing ratio for each F^+ to reach saturation of C_D and C_L increases. The details of this threshold blowing ratio required

for saturation will be discussed further at the end of this section.

Once the slot location moves downstream of separation, it is observed for all frequencies other than $F^+ = 14$ at $x_j^* = 1.3\%$ that a certain blowing ratio must be exceeded before there are any positive effects on C_D and C_L. At $x_j^* = 1.3\%$ the blowing ratio must exceed $C_B = 0.6$ for $F^+ = 1$, 2 and 58, while positive results are seen even at $C_B = 0.2$ for $F^+ = 14$. There is more of a dependance on F^+ at $x_j^* = 4.3\%$ with regards to the minimum blowing ratio where drag is begins to decrease. For F^+ =[1, 2, 14, 58], the corresponding values of C_B that must be exceeded are [1, 0.5, 0.5, 1.5]. Once this blowing ratio has been exceeded, the additional increase in C_B required to reach saturation is also noticeably larger than in the upstream forcing cases. That is, the pre-saturation slopes $|\partial C_L/\partial C_B|$ and $|\partial C_D/\partial C_B|$ decrease as the slot moves downstream. At the most downstream slot location, saturation occurs approximately at or beyond $C_B = 3$ for each F^+. As x_j^* is increased from -4.3% to 4.3%, the maximum C_D at saturation for each frequency remains relatively unchanged, while the maximum C_L tends to decrease for each F^+.

The effect of slot location on C_D and C_L is highlighted for 'low-frequency' forcing at $F^+ = 1$ and 'high-frequency' at $F^+ = 58$ in Figure 5.4. These plots clearly demonstrate the decrease in $|\partial C_L/\partial C_B|$ and $|\partial C_D/\partial C_B|$ prior to saturation with increasing x_j^* and the corresponding increase in C_B required to reach saturation. The exemption from this is for $F^+ = 58$ at $x_j^* = -4.3\%$ and -1.3% where saturation occurs at approximately $C_B = 1$ in each case. However, C_L reaches a constant value that is larger for $x_j^* = -4.3\%$ and $F^+ = 58$. Lift generally increases as the slot location moves upstream for a given C_B at these two frequencies, but the behaviour of drag is slightly more complex. Decreasing x_j^* generally decreases drag at $F^+ = 1$, with this effect saturating at large blowing ratios. However, for $F^+ = 58$ there is a limited range $0.5 \leq C_B \leq 1$ where forcing at $x_j^* = -1.3\%$ causes a greater reduction in C_D than -4.3%. This effect is not observed at $F^+ = 2$ or 14, which show trends similar to $F^+ = 1$.

To study the effect of control on the flow when C_B is below or above the level required for C_L and C_D to reach saturation, surface pressure distributions are considered. Figure 5.5 shows C_p distributions at $C_B = 0.1$ and $C_B = 1$ for $x_j^* = -1.3\%$ (indicated by the dashed vertical lines in Figures 5.2b and 5.3b). At $C_B = 0.1$, there is considerable change in C_D and C_L between $F^+ = 1$, 2 and 14; however, this blowing ratio does not have an effect on the flow at $F^+ = 58$. The results demonstrate that the initial drag reduction and lift increase at $C_B = 0.1$ is due to the formation of a laminar separation bubble on the suction surface. The LSB is identified from the characteristic pressure plateau that is followed by a pressure recovery. Transition to turbulence in the boundary layer occurs

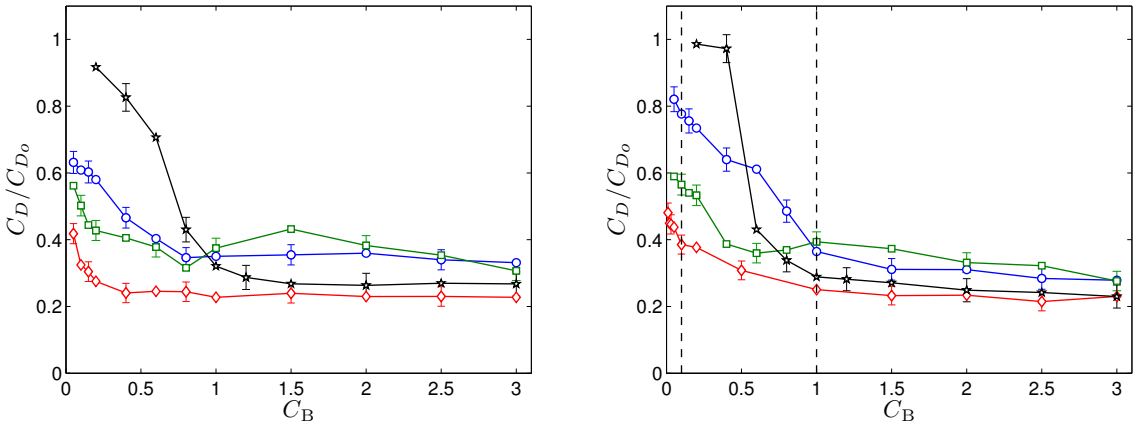

(a) $x_j^* = -4.3\%$ (b) $x_j^* = -1.3\%$

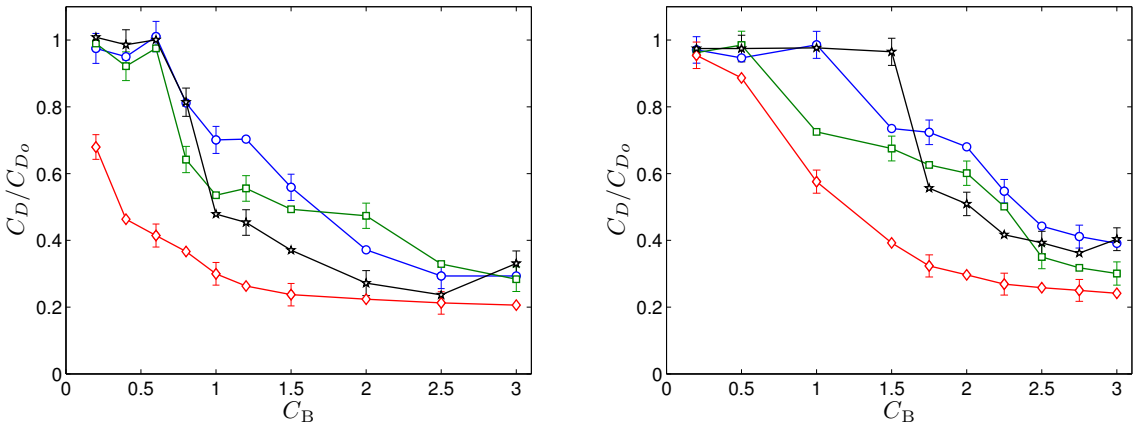

(c) $x_j^* = 1.3\%$ (d) $x_j^* = 4.3\%$

Figure 5.2: Drag coefficient variation with C_B, F^+ and slot location. ($\circ$) $F^+ = 1$, ($\square$) $F^+ = 2$, ($\diamond$) $F^+ = 14$, ($\star$) $F^+ = 58$.

approximately at the end of the plateau and is followed by reattachment, the location of which can be estimated to be where the rate of pressure recovery becomes more gradual [63]. At $F^+ = 1$ and 2 there is an easily identifiable LSB that is approximately $0.25c$ in length. At $F^+ = 14$, it is less apparent from the C_p distribution alone whether a LSB exists since it is not 'flat' over any over any chordwise extent, however the typical pressure recovery following turbulent transition in an LSB is observed. The shape of the C_p distribution for $F^+ = 14$ bears resemblance to those observed by Zilli et al. [87] at $Re_c \geq 150,000$ and $\alpha = 8°$ on a SD7003 airfoil, where skin friction measurements confirmed the presence of an LSB. The location where rapid pressure recovery begins is upstream relative to $F^+ = 1$ and 2, therefore there is likely a bubble of shorter length

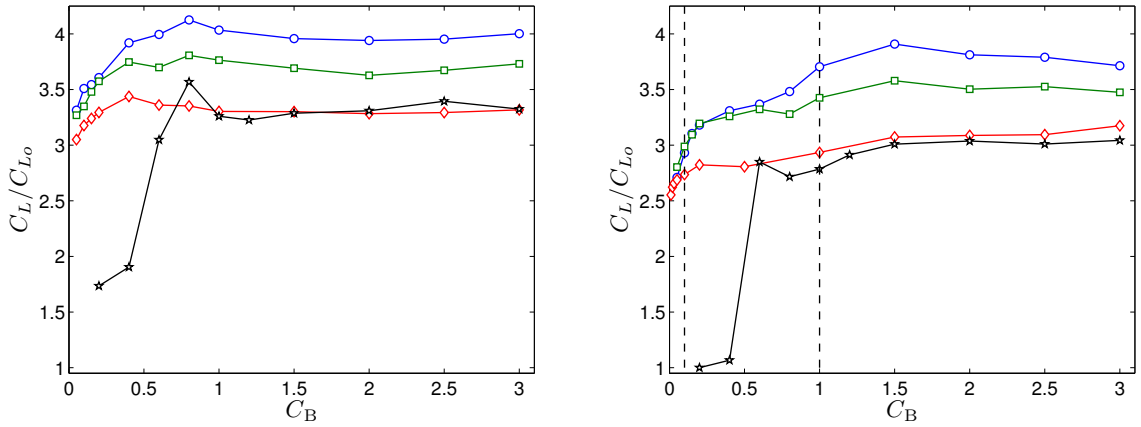

(a) $x_j^* = -4.3\%$ (b) $x_j^* = -1.3\%$

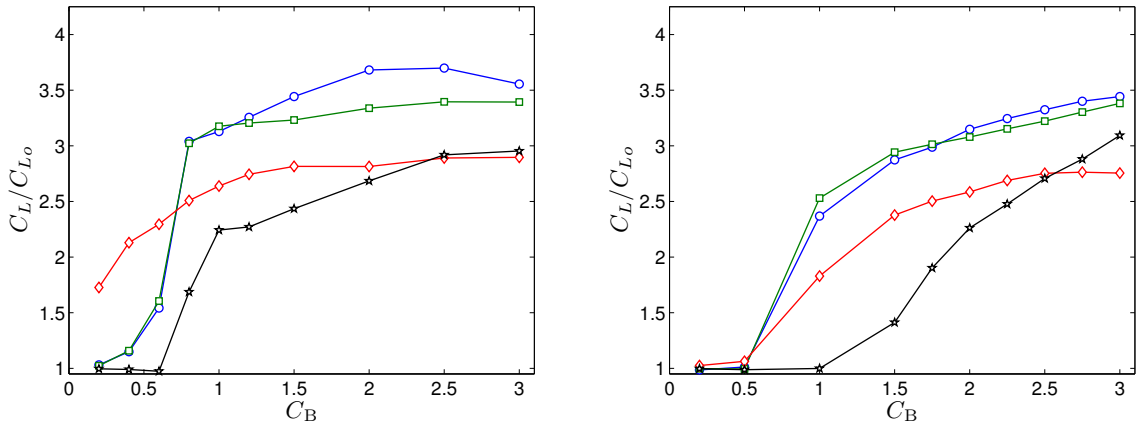

(c) $x_j^* = 1.3\%$ (d) $x_j^* = 4.3\%$

Figure 5.3: Lift coefficient variation with C_B, F^+ and slot location. ($\circ$) $F^+ = 1$, ($\square$) $F^+ = 2$, ($\diamond$) $F^+ = 14$, ($\star$) $F^+ = 58$. Note that at this scale, the error bars on C_L are no larger than the size of the plot markers.

that is present in this case. The LSB for $F^+ = 1$ and 2 causes reduced pressure over a greater extent of the suction surface, therefore leading to larger C_L than $F^+ = 14$ with a shorter bubble. The drag coefficient, however, does not scale with LSB size since C_D at $C_B = 0.1$ decreases monotonically with increasing F^+ from 1 to 14, yet the LSB length for $F^+ = 1$ and 2 are nearly identical. This effect will be discussed further in the forthcoming sections regarding flow field measurements.

The results in Figures 5.2 and 5.3 suggest that in terms of drag reduction, $F^+ = 14$ is the most effective forcing frequency, while for lift increase $F^+ = 1$ is most effective. A range of frequencies from $F^+ = 0.25$ to 58 was tested for a fixed slot location $x_j^* =$

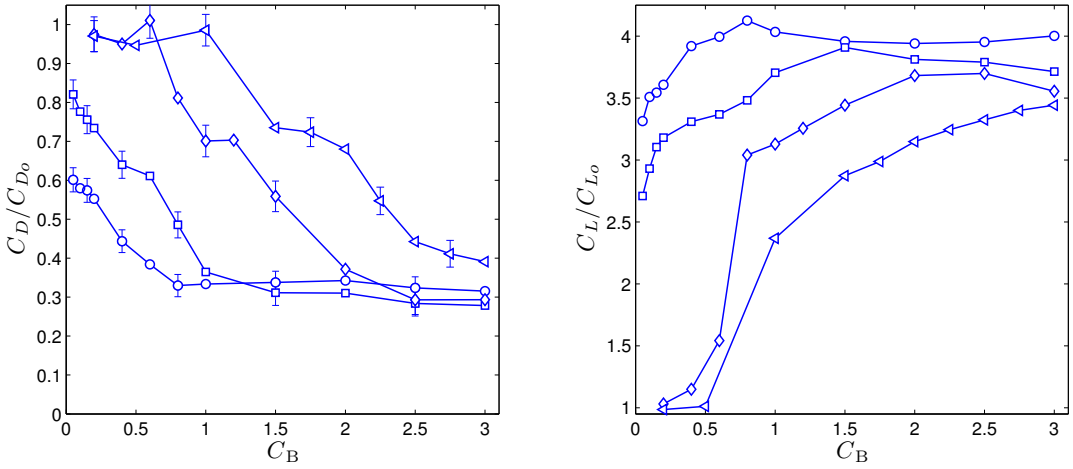

(a) $F^+ = 1$

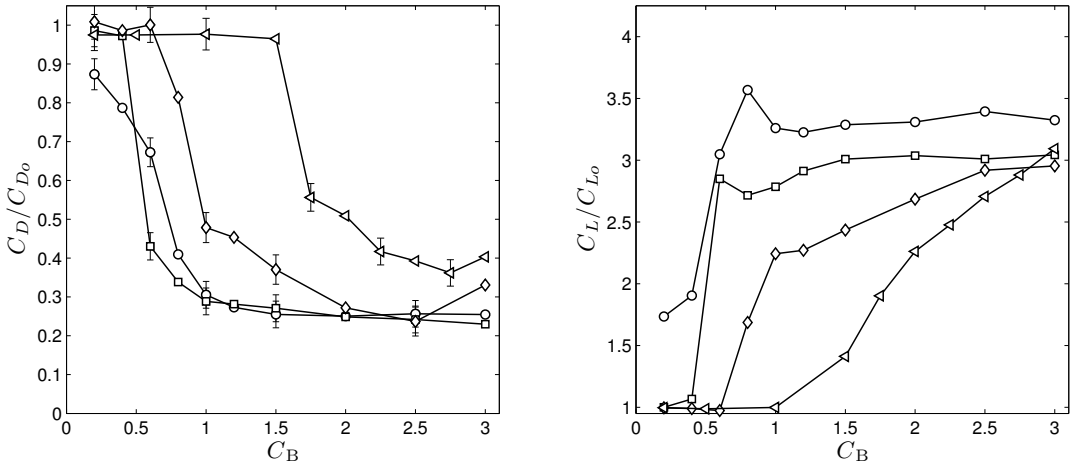

(b) $F^+ = 58$

Figure 5.4: Lift and drag coefficient variation with C_B and slot location. ($\circ$) $x_j^* = -4.3\%$, ($\square$) $x_j^* = -1.3\%$, ($\diamond$) $x_j^* = 1.3\%$, ($\triangleleft$) $x_j^* = 4.3\%$.

-1.3% at pre/post-saturation blowing ratios; $C_B = 0.1$ and 1. Such a measurement that considers the effect of F^+ on both lift and drag over such a wide range of excitation frequencies is one that has not yet been demonstrated for a post-stalled airfoil at low Re_c. Studies often consider only the effect on C_L (e.g. [41]) or the pressure drag (e.g. [3]), since these parameters are relatively easily acquired from only C_p distributions. Figure 5.6 shows the results of C_D and C_L as functions of F^+ at this slot location and for the two blowing ratios. For reference, the shaded areas in the plots show the frequencies associated with the baseline flow (i.e., f_w^+ and f_{sl}^+). In terms of lift increase, the results confirm that forcing at $F^+ = 1$, corresponding to f_w^+ is most effective. The maxima in

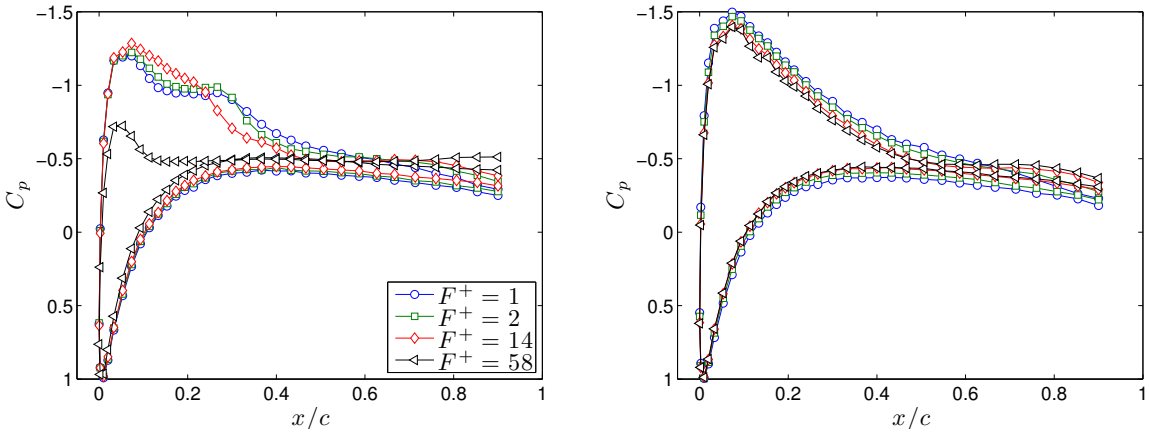

(a) $C_\mathrm{B} = 0.1$ (b) $C_\mathrm{B} = 1$

Figure 5.5: Surface pressure distributions for low and high C_B at $x_\mathrm{j}^* = -1.3\%$.

C_L at $F^+ = 1$ is more pronounced at the larger blowing ratio, while at $C_\mathrm{B} = 0.1$ there is an approximate plateau over $1 \leq F^+ \leq 5$. These results are consistent with previous studies who also observed a maximum in C_L at $F^+ \approx 1$ when controlling post-stall flow [41; 43]. Greenblatt et al. [41] investigated the effect on C_L over $0 \leq F^+ \leq 10$ with leading-edge excitation at $\alpha = 16°$ and $Re_c = 200,000$ and saw a maximum at $F^+ = 1$–2 for $C_\mu = 0.2\%$ and 1.2%. However, unlike the present results where lift is increased over all F^+ at $C_\mathrm{B} = 1$, they observed a range of F^+ that was ineffective for increasing lift even at a relatively large $C_\mu = 1.2\%$ (the corresponding C_μ for the present experiments at $C_\mathrm{B} = 1$ is approximately $C_\mu = 0.3\%$). Several factors may contribute to this difference in behaviour, including relative slot location, Reynolds number, and angle-of-attack.

The drag results show that for $C_\mathrm{B} = 0.1$, there is a minimum at frequencies in a range around f_sl^+. Frequencies in the range $F^+ \geq 41$ are ineffective in terms of drag reduction at this blowing ratio, while control at frequencies $F^+ \leq 1$ varies from non-optimal to detrimental. At $C_\mathrm{B} = 1$, all frequencies lead to drag reduction, however there appears to be a minimum over $5 \leq F^+ \leq 41$. In examining the other slot location cases shown in Figures 5.2 and 5.3, these results appear to be applicable over the range of x_j^* tested. It is also interesting to note that for $C_\mathrm{B} = 0.1$ and $F^+ = 0.25$, despite the increase in drag, the lift is still substantially increased to greater than $2C_{Lo}$. As shown in Figure 5.7, this increase in lift and drag is due to the presence of a long laminar separation bubble. The location of reattachment is difficult to ascertain from the C_p profile, however the bubble likely extends from $x/c \approx 0.15$ to a location near the trailing edge. Unlike short LSBs which are beneficial for both lift and drag relative to stalled flow (Figure 5.5(a)), a long

LSB may increase lift while being detrimental in terms of drag increase. An important aspect that is not investigated in this work is the effect of control on the lift and drag fluctuations. It is likely that for $F^+ \leq \mathcal{O}(1)$, a time-averaged increase C_L and decrease in C_D may be accompanied by substantial fluctuations in these forces. This is supported by the dynamics of the controlled flow at $F^+ = 1$, discussed in Section 5.3.

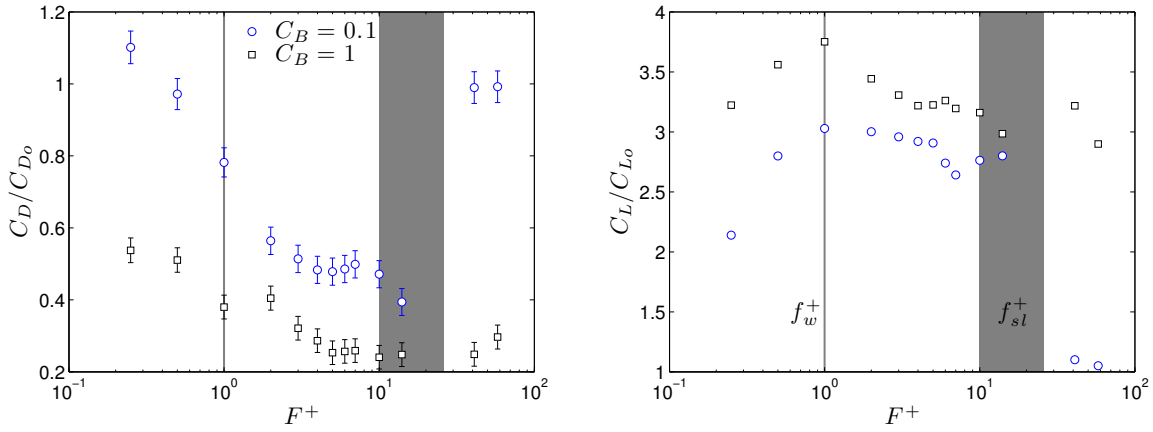

Figure 5.6: Lift and drag coefficient variation with F^+ for $C_\mathrm{B} = 0.1$ and 1 (see vertical dashed lines in Figures 5.2 and 5.3) at $x_\mathrm{j}^* = -1.3\%$. The shaded regions indicate the wake and separated shear layer frequencies associated with the baseline flow.

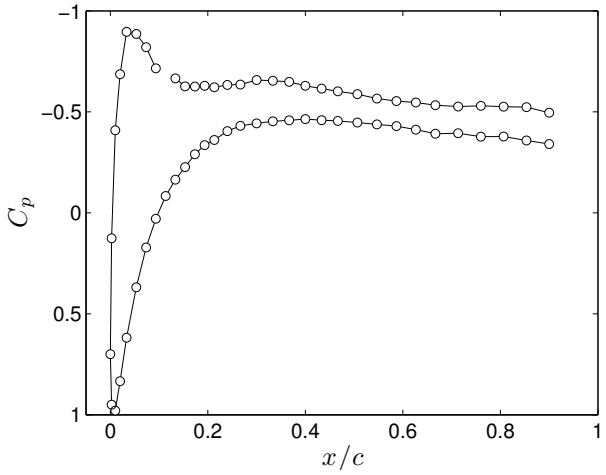

Figure 5.7: C_p profile for $F^+ = 0.25$ and $C_\mathrm{B} = 0.1$ at $x_\mathrm{j}^* = -1.3\%$ where $C_L/C_{Lo} = 2.1$ and $C_D/C_{Do} = 1.1$.

At all slot locations and reduced frequencies, increasing C_B initially leads to drag reduction/lift increase due to the formation of a LSB, which is then followed by fully

attached flow and a saturation in the control benefits. A threshold blowing ratio can therefore be defined as the C_B at a particular F^+ required for the flow to become fully attached and is given by C_B^*. Fully attached flow is estimated from the shape of the C_p distribution, and the determination of C_B^* in this manner was used to guide subsequent flow field measurements. Velocity measurements over the airfoil chord using hot-wire were time consuming and thus for each slot location and desired F^+, these measurements were done at $C_B/C_B^* = 1$ and 2 (Section 5.2). The impact of slot location on the control effectiveness can be quantified by considering the variation in this threshold C_B^* with x_j^*, as shown in Figure 5.8 for $F^+ = 1$, 14 and 58. The C_B^* values for $F^+ = 2$ were nearly identical to $F^+ = 1$ and were thus were not included for clarity. For each frequency, the threshold blowing ratio for fully attached flow decreases as the slot moves upstream, with this decrease beginning to saturate as $x_j^* = -4.3\%$ is reached. The results also show that at each x_j^* tested, the threshold C_B is lowest for $F^+ = 14$. This effect becomes more pronounced as the slot location moves upstream, with only $C_B^* = 0.15$ required at $F^+ = 14$ and $x_j^* = -4.3\%$. High-frequency control at $F^+ = 58$ is generally the least effective, other than at $x_j^* = -1.3\%$ and 1.3% where the threshold C_B at this frequency is equivalent to $F^+ = 1$.

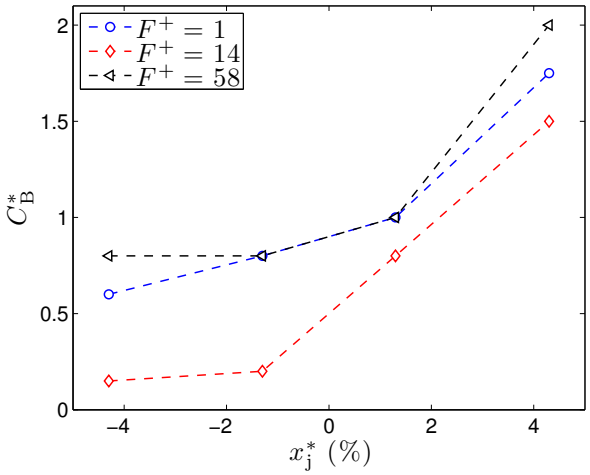

Figure 5.8: Threshold blowing ratio required for fully attached flow as a function of slot location and F^+.

The effect of slot location on control effectiveness can also be assessed by considering the lift-to-drag ratio, C_L/C_D, at fixed F^+ and C_B. Figure 5.9 shows C_L/C_D as a function of x_j^* for $C_B = 0.2$ (shown as open markers) and 1 (filled markers), and $F^+ = 1$, 14 and 58. The blowing ratio $C_B = 0.2$ was selected as it is the lowest blowing ratio tested for all F^+ and x_j^*. The measurement uncertainty in C_L/C_D for the cases shown in Figure

5.9 is within ±13%. The results clearly demonstrate that the effectiveness of control in improving lift-to-drag increases as the slot location moves further upstream. This is in contrast to the common suggestion that the actuator location should be as close to separation as possible [44]. These results suggest that there is some location upstream of separation, potentially as far upstream as the leading edge, where C_L/C_D is maximized. In particular, for control at $F^+ = 1$ and 58 it appears that the growth in C_L/C_D with decreasing x_j^* may plateau or peak at some location $x_j^* < -4.3\%$. The C_L/C_D curves for $F^+ = 14$ at $x_j^* < 0$ have greater slope and may continue to increase up to the leading edge. These results also show that despite excitation at $F^+ = 1$ having greater benefits in terms of lift increase, the benefits of $F^+ = 14$ for drag reduction cause this forcing frequency to be most effective at improving the lift-to-drag ratio. At the most upstream slot location, forcing at $F^+ = 14$ and $C_B = 0.2$ leads to greater or approximately equivalent C_L/C_D as forcing with $C_B = 1$ at $F^+ = 1$ or 58 (i.e., similar results are achieved for C_B that is an order of magnitude lower). Least effective is high-frequency control at $F^+ = 58$ because while this frequency may have threshold C_B values similar to $F^+ = 1$, at low blowing ratios such as $C_B = 0.2$ forcing at $F^+ = 58$ leads to much lower C_L/C_D. At $C_B = 1$, the lift-to-drag performance of $F^+ = 1$ and 58 become similar.

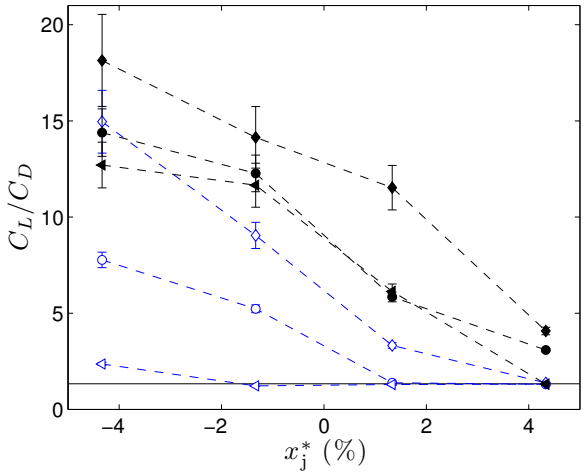

Figure 5.9: Lift-to-drag ratio variation with slot location. The solid horizontal line shows the baseline value of $C_{Lo}/C_{Do} = 1.3$. (○) $F^+ = 1$, (◇) $F^+ = 14$, (◁) $F^+ = 58$. Open markers: $C_B = 0.2$, filled markers: $C_B = 1$.

5.2 Control effects: mean flow

This section will detail the effects of control on the mean flow using velocity field measurements performed by PIV and hot-wire at midspan. Time-averaged velocity statistics were obtained using PIV for all F^+ and a range of C_B at one slot location: $x_\mathrm{j}^* = -1.3\%$. Boundary layer velocity profiles over $0.2 \leq x/c \leq 0.9$ measured by hot-wire were obtained for all slot locations for $F^+ = 1$ and 58 at $C_\mathrm{B}/C_\mathrm{B}^* = 1$ and 2. The forthcoming section will discuss the dynamics of the flow for the same cases. The control cases that were selected for velocity field measurement (including phase-locked PIV, discussed in Section 5.3) using the two different techniques represent a compromise between covering the entire parameter space and the time required for experiments.

Figure 5.10 shows contours of U_T with forcing at $x_\mathrm{j}^* = -1.3\%$ for each F^+ and two blowing ratios: $C_\mathrm{B} = 0.1$ and 1 (see Figure 5.5 for the corresponding C_p distributions). Included in the plots are the mean streamlines and the outline of the boundary layer (i.e. $y = \delta$) over $0.35 \leq x/c \leq 0.9$. At $C_\mathrm{B} = 0.1$, where the C_p distributions indicate LSBs for $F^+ = 1$, 2 and 14, the velocity contours show no visible regions of reversed flow, indicating that the bubble heights do not exceed the height of the measured region from the airfoil surface ($y/c \approx 0.008$). However, for $F^+ = 1$ and 2 there is evidence of curvature of the streamlines just downstream of the high velocity region that indicate the presence of the LSB. Comparing the flow at $F^+ = 14$ to $F^+ = 1$ or 2 at $C_\mathrm{B} = 0.1$, the boundary layer at $F^+ = 14$ is observed to be substantially thinner due to a smaller separation bubble. There is no effect due to the forcing at $F^+ = 58$ and $C_\mathrm{B} = 0.1$.

Increasing to $C_\mathrm{B} = 1$ leads to fully attached flow for each F^+, which is expected from the C_p distributions in Figure 5.5. The transition from attached with an LSB to fully attached flow is accompanied by an increase in the maximum velocity over the suction surface and a thinner boundary layer that more closely follows the local airfoil curvature. At $F^+ = 1$ and 2, the slight curvature of the streamlines at the trailing edge for $C_\mathrm{B} = 0.1$ is eliminated with fully attached flow at the larger blowing ratio.

Evaluation of δ was limited to the chordwise range $0.35 \leq x/c \leq 0.9$ due to insufficient spatial resolution and lack of data in the near wall region (i.e. $< y/c = 0.008$) when the flow is fully attached at $C_\mathrm{B} = 1$. An example of boundary layer profiles of U_s and U_n for $F^+ = 1$ and $C_\mathrm{B} = 1$ is shown in Figure 5.11. At the most upstream location $x/c = 0.35$, the first point in the wall-tangential velocity profile is at 75% of the edge velocity. This precludes the determination of integral boundary layer parameters over the majority of the airfoil chord, however the location of δ can still be identified with confidence. The variation of δ over the resolvable chordwise range for $F^+ = 1$ and $F^+ = 14$ over a range

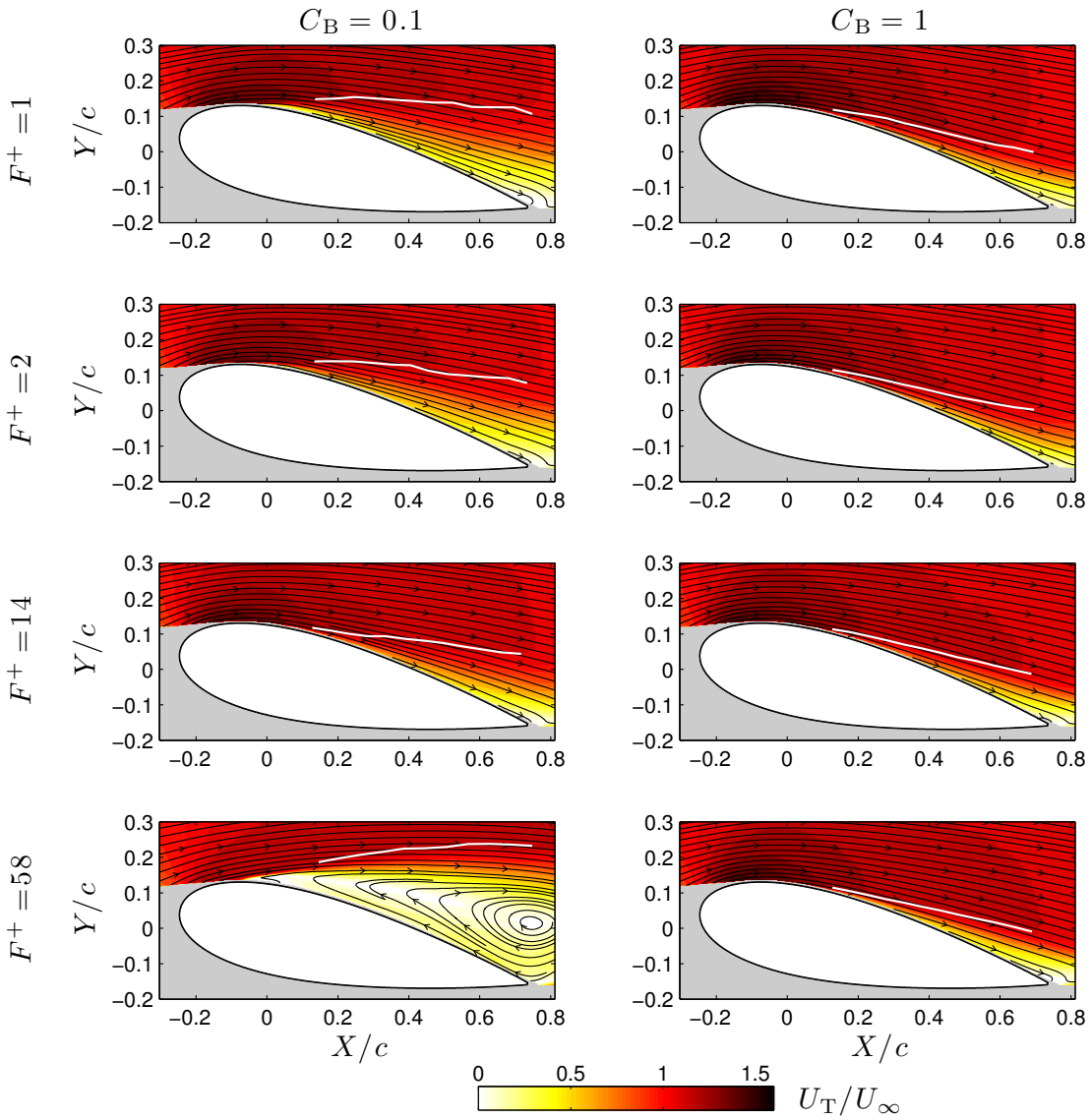

Figure 5.10: Contours of mean total velocity for $x_j^* = -1.3\%$. Black lines show the mean streamlines, and the white lines indicates δ over $0.35 \leq x/c \leq 0.9$.

of $0.1 \leq C_B \leq 2$ is shown in Figure 5.12. At $F^+ = 1$, a substantial decrease in δ occurs as C_B increases from 0.1 to 0.8 due to the flow becoming fully attached, which is accompanied by a large decrease in drag from approximately $0.8C_{Do}$ to $0.5C_{Do}$ (Figure 5.2). There is little change in δ once $C_B \geq 1$ is reached, other than over approximately $0.5 \leq x/c \leq 0.65$, where the increase to $C_B \geq 2$ causes a further decrease in boundary layer thickness. Similar results are observed at $F^+ = 14$, although a slightly more upstream region $0.4 \leq x/c \leq 0.55$ shows the additional decrease in δ with increasing C_B

above $C_\mathrm{B} = 0.8$. Comparing the results of $F^+ = 1$ and 14 shows that over the entire range of C_B, δ near the trailing edge is similar in magnitude, however the boundary layer is significantly thinner in the region $x/c < 0.5$ with forcing at $F^+ = 14$.

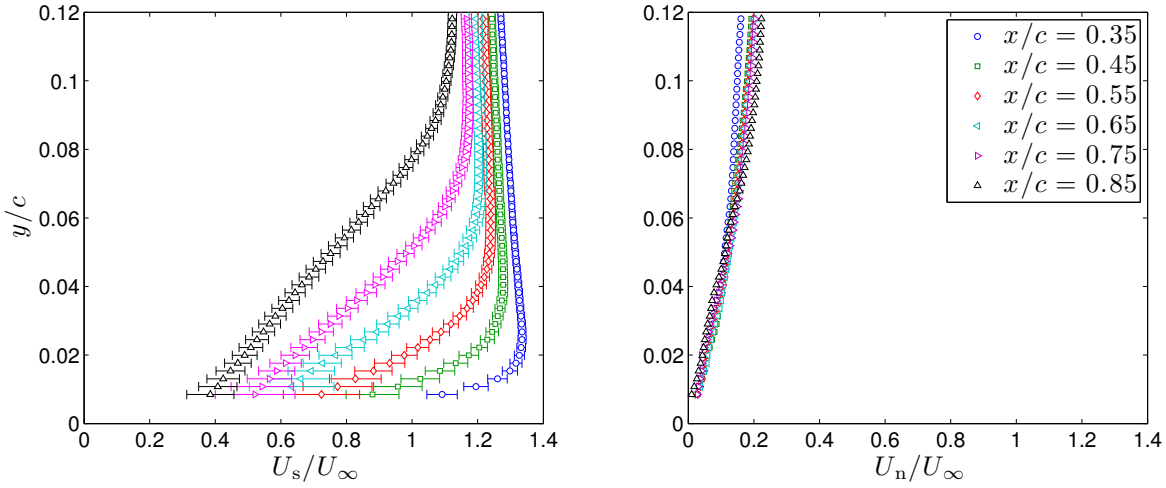

Figure 5.11: Boundary layer velocity profiles at $C_\mathrm{B} = 1$, $F^+ = 1$ and $x_\mathrm{j}^* = -1.3\%$. Error bars are omitted for U_n but are similar in magnitude to the corresponding values of U_s.

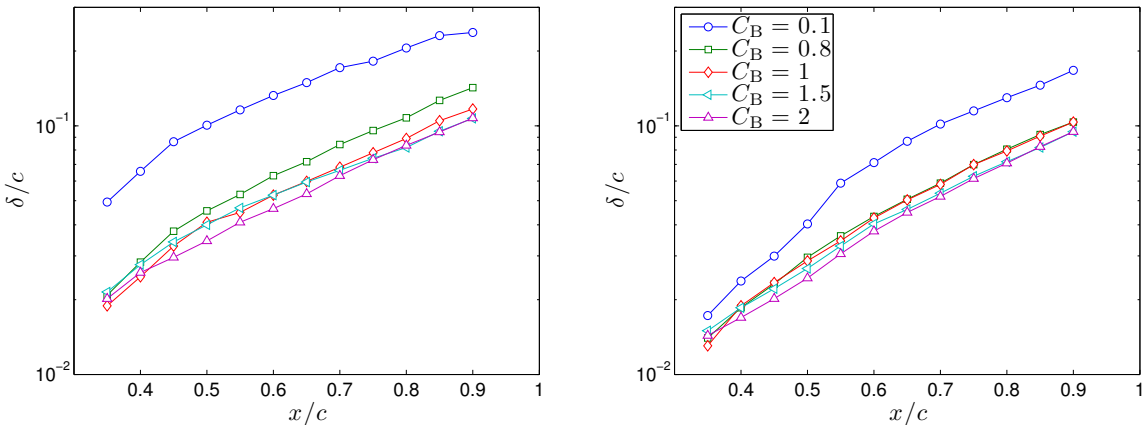

(a) $F^+ = 1$ (b) $F^+ = 14$

Figure 5.12: Boundary layer thickness evolution along the airfoil chord with increasing C_B for $x_\mathrm{j}^* = -1.3\%$.

The effects of C_B and F^+ for control at $x_\mathrm{j}^* = -1.3\%$ on the trailing edge boundary layer are shown in Figure 5.13 by considering the displacement thickness at $x/c = 0.9$, $(\delta^*/c)_{x/c=0.9}$. Comparing Figures 5.13 and 5.2b it can be observed that the drag coefficient

at each F^+ shows a very similar trend to the trailing edge displacement thickness. As discussed previously, the change in C_L at $C_\mu = 0.1$ for $x_j^* = -1.3\%$ with F^+ increasing from 1 to 14 was found to scale with the separation bubble size, but this is not the case for C_D. The results in Figure 5.13 demonstrate that at $C_\mu = 0.1$, the monotonic decrease in drag with frequency increasing from $F^+ = 1$ to 14 is due to a reduction in the boundary layer thickness near the airfoil trailing edge. It is intuitive that this decrease in boundary layer thickness leads to a mean flow with a narrower wake, and thus a reduction in C_D. This behaviour suggests that the effect of control at pre-saturation C_μ on $(\delta^*/c)_{x/c=0.9}$ and C_D is strongly related to F^+, and therefore the dynamic aspects of the forcing cycle. This is in contrast to C_L, which was found to scale with separation bubble length in this blowing ratio regime. The dynamic aspects of control will be discussed in Section 5.3.

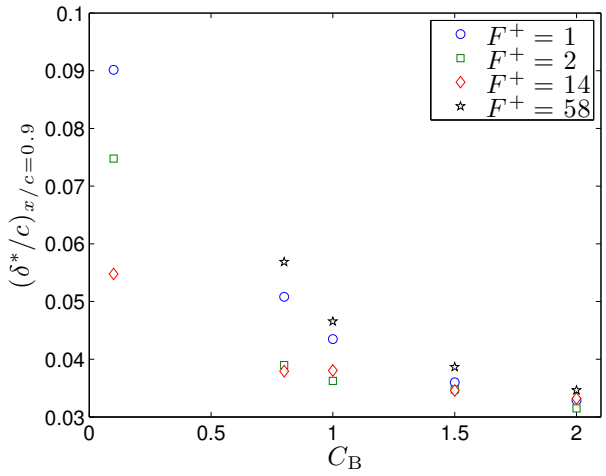

Figure 5.13: Boundary layer displacement thickness at $x/c = 0.9$ for $x_j^* = -1.3\%$. The value for $C_\mu = 0.1$ and $F^+ = 58$, where the flow remains stalled, is excluded for scaling purposes.

Contours of Reynolds shear stress for $x_j^* = -1.3\%$ are presented in Figure 5.14 for the same cases as Figure 5.10. This quantity is useful to consider as it represents momentum transfer due to velocity fluctuations. It should be noted that for the PIV velocity fields, decomposition of the velocity fluctuations into coherent and turbulent components was not possible due to a resolution in phase of only 45°. The Reynolds stress $\overline{uv}$ therefore contains contributions of possible coherent unsteadiness, and turbulent unsteadiness created by the forcing. At $C_\mu = 0.1$, the Reynolds stress in the region just downstream of the synthetic jet for $F^+ = 1$ and 2 increases to relatively large magnitudes up to $\overline{uv}/U_\infty^2 = -0.05$, which exceeds that of the baseline flow ($F^+ = 58$ at $C_\mu = 0.1$ is equivalent to the baseline case). After the location where the peak $\overline{uv}$ is reached, a de-

crease in magnitude is observed in the chordwise direction to values of approximately $\overline{uv}/U_\infty^2 = -0.01$ at the trailing edge. A different behaviour is observed at the same blowing ratio for $F^+ = 14$, where not only is the Reynolds stress lower in magnitude, but $\overline{uv}$ remains low in magnitude until further downstream compared to the other cases. The largest magnitude of $\overline{uv}$ for $F^+ = 14$ is similar to that of the wake for $F^+ = 1$ or 2. This is indicative of regions of highly unsteady flow near the synthetic jet at $F^+ = 1$ and 2, which is to be expected, but substantially less so with forcing at $F^+ = 14$. This will be explored further by considering phase-averaged velocity fields in Section 5.3. The results at the higher blowing ratio $C_\mu = 1$ for $F^+ = 1$ and 2 are similar to $C_\mu = 0.1$ and $F^+ = 14$, in that $\overline{uv}$ is relatively uniform at $\overline{uv}/U_\infty^2 = -0.01$ along the airfoil chord once this value has been reached. At $F^+ = 14$ and 58, substantially lower magnitudes of $\overline{uv}$ are observed in the midchord region, with an increase along the airfoil chord to approximately $\overline{uv}/U_\infty^2 = -0.01$ at the trailing edge. Compared to $C_\mu = 0.1$, the region where $|\overline{uv}/U_\infty^2| \geq 0.001$ is contained closer to the surface due to a general reduction in boundary layer thickness at $C_\mu = 1$.

The foregoing results presented in this section showed the effects on the mean flow of forcing at a fixed location of $x_j^* = -1.3\%$. The effect of slot location on the mean flow in the boundary layer is considered in Figure 5.15 for $F^+ = 1$ and 58 at a fixed blowing ratio relative to the threshold value, $C_\mu/C_\mu^* = 1$. For $F^+ = 1$, laminar velocity profiles with an inflection point and similar thickness are seen at the most upstream measurement station. Moving downstream beyond $x/c > 0.4$, the cases with forcing downstream of separation lead to a substantially thicker boundary layer than with upstream forcing. In addition, the velocity profiles each exhibit a 'fuller' shape with no inflection point, which is indicative of an attached turbulent boundary layer. The shape of the velocity profiles for $x_j^* = -4.3\%$ at $x/c = 0.2$ and 0.3 suggest that that there may be a small LSB in this region, however U_t shows no distinct evidence of reversed flow. The difference in behaviour with x_j^* in the chordwise region near the synthetic jet ($x/c < 0.4$) is likely attributed to the different values of C_μ^*, where $x_j^* = -4.3\%$ has the lowest threshold blowing ratio of the four slot locations.

The effect of forcing at $F^+ = 58$ on the mean boundary layer shows notable differences compared to $F^+ = 1$. At this frequency, forcing at the most upstream slot location leads to a separation bubble within the range $x/c \leq 0.4$, as evidenced by the large region of approximately constant U_t at $x/c = 0.3$. The presence of this LSB causes the boundary layer to be thicker than the $x_j^* = -1.3\%$ and 4.3% cases in the region of the LSB. Downstream of this ($x/c > 0.4$), the boundary layer is observed to be substantially thicker for $x_j^* > 0$. Forcing at the most downstream location leads to earlier appearance

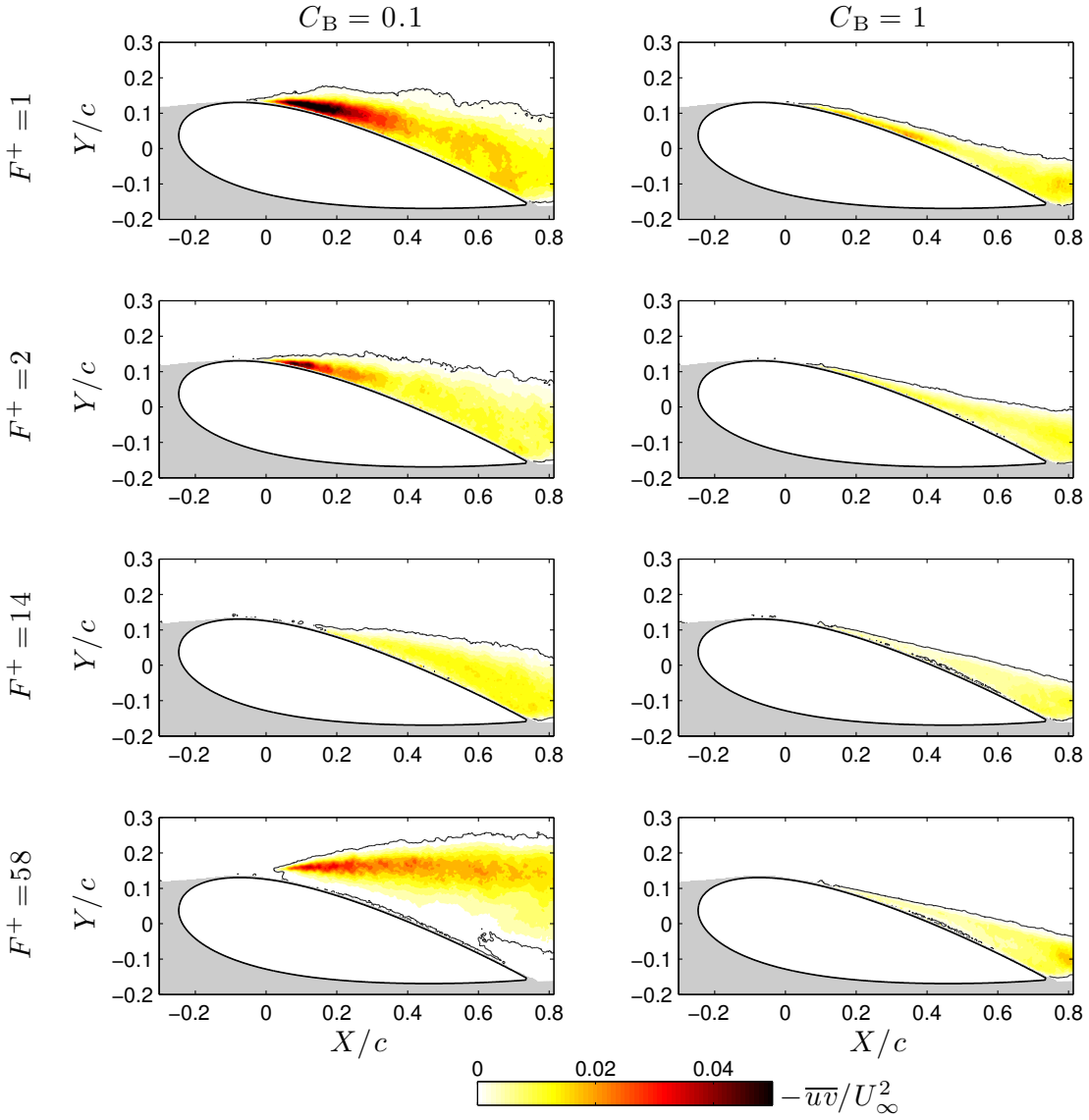

Figure 5.14: Contours of Reynolds shear stress for $x_j^* = -1.3\%$. The contour at $-\overline{uv}/U_\infty^2 = 0.001$ is outlined in black.

of turbulent velocity profiles, with a turbulent profile evident at $x/c = 0.3$ for $x_j^* = 4.3\%$. This again is likely due to the increasing threshold blowing ratio with increasing x_j^*. Once $x/c = 0.5$ is reached, each x_j^* case shows velocity profiles that suggest the boundary layer is turbulent. The upstream forcing cases exhibit different velocity profile shapes relative to downstream forcing in the region near the trailing edge, where a region of high velocity near the wall is followed by an area of low velocity gradient near $y = 0.5\delta$. This is most apparent at $x/c = 0.9$ for $x_j^* = -4.3\%$. While forcing downstream of separation leads to

flows that are attached over the entire chord, the near wall region of the boundary layer at $x/c > 0.5$ is less energetic relative to the upstream forcing cases.

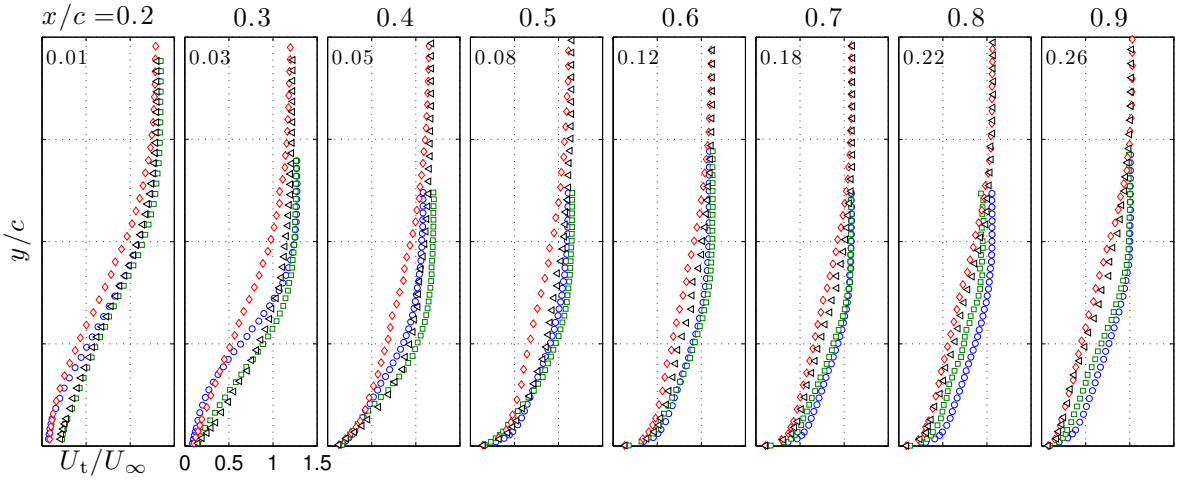

(a) $F^+ = 1$

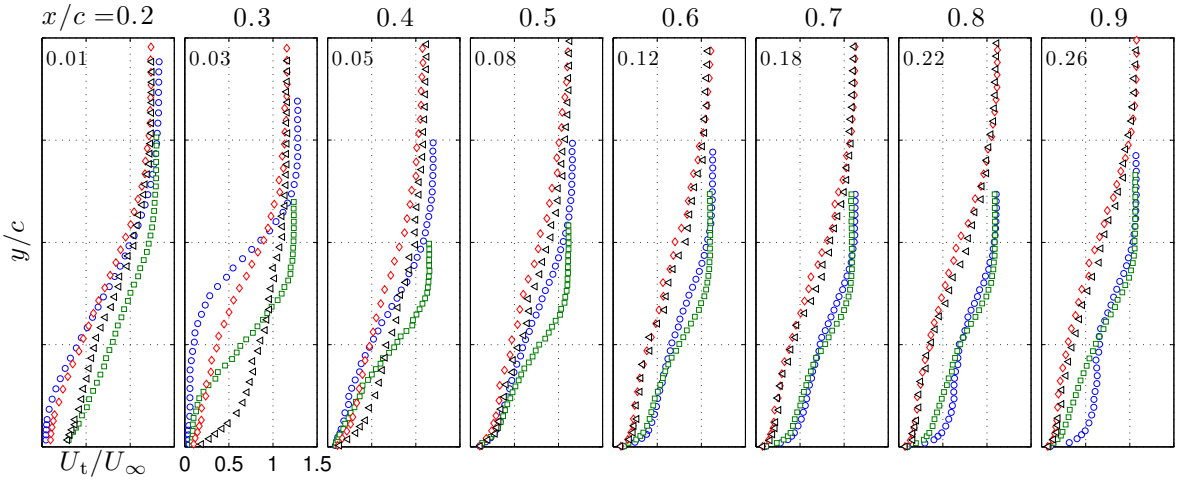

(b) $F^+ = 58$

Figure 5.15: Boundary layer velocity profiles along the chord with forcing at $-4.3 \leq x_j^* \leq 4.3\%$ and $C_B/C_B^* = 1$. The upper y/c limit for each plot is given in the upper left corner and increases along x/c. ($\circ$) $x_j^* = -4.3\%$, ($\square$) $x_j^* = -1.3\%$, ($\diamond$) $x_j^* = 1.3\%$, ($\triangleleft$) $x_j^* = 4.3\%$.

Similar mean velocity profiles as in Figure 5.15 but with forcing at $C_B/C_B^* = 2$ are presented in Figure 5.16. The relatively high blowing ratios corresponding to $C_B/C_B^* = 2$ were only attainable for slot locations $-4.3 \leq x_j^* \leq 1.3\%$ given the actuator capabilities. For both $F^+ = 1$ and $F^+ = 58$, the results are markedly different than $C_B/C_B^* = 1$, as there is very little change in the mean velocity profiles for the different forcing locations. Boundary layer profiles typical of turbulent flow are observed by $x/c = 0.3$ for all x_j^* at

$F^+ = 58$, while profiles with similar shapes occur further downstream at approximately $x/c = 0.6$ for $F^+ = 1$. The effect of control on the location of turbulent transition will be discussed further in Section 5.3. Some small differences are seen at $x/c < 0.5$ for $F^+ = 58$, however downstream of this, U_t/U_∞ is nearly identical. In particular, for $x_j^* = -1.3\%$ an inflectional boundary layer profile is seen at $x/c = 0.2$, which suggests that a small separation bubble may by present in this case. Although not shown for brevity, this is supported by a plateau in C_p spanning approximately $0.04c$ immediately downstream of the slot. In general, the results in Figure 5.16 show that the larger the blowing ratio relative to the threshold value, the less impact the slot location has on the mean flow. This can also be observed in the lift and drag coefficients, examples of which are shown for $F^+ = 1$ for the four slot locations with increasing C_B/C_B^* in Figure 5.17. Comparing the boundary layer profiles in Figure 5.15 at $C_B/C_B^* = 1$ to the corresponding C_L and C_D values, it can be observed that the generally thicker boundary layer with downstream forcing results in lower lift and larger drag relative to the upstream forcing cases. The slightly lower C_D and increased C_L at $x_j^* = -4.3\%$ relative to $x_j^* = -1.3\%$ is also consistent with slightly fuller boundary layer profiles near the trailing edge. Once $C_B/C_B^* = 2$ is reached, the values of C_D are approximately equivalent (within measurement uncertainty) and there is less variation in C_L. This agrees with the velocity profiles that are nearly equivalent over the entire airfoil chord at $C_B/C_B^* = 2$ and $F^+ = 1$. The variation in C_L is likely represented by differences in the boundary layer velocity profiles closer to the leading edge in the vicinity of the suction peak, which are outside the measurement domain at $x/c < 0.2$.

5.3 Control effects: dynamics

This section will discuss the dynamic aspects of the controlled flow using velocity field measurements. Phase-locked velocity fields were measured at $x_j^* = -1.3\%$ for $F^+ = 1$ and 14 at $C_B = 0.1$ and 1. For each of these four control cases, the entire cycle was captured with a phase resolution of 45° (i.e., eight discrete phase angles). Phase-locked measurements by PIV were not possible at $F^+ = 58$ due to the finite time delay between images. The boundary layer velocity profiles measured by hot-wire for the cases described in Section 5.2 were acquired simultaneously with the input signal, which provided the means to decompose velocity signals into turbulent and coherent fluctuations (as described in Section 2.8) for $F^+ = 1$ and 58. Spectral analysis of velocity at important locations in the flow was also performed using hot-wire measurements.

Figures 5.18 and 5.19 show contours of the coherent transverse velocity fluctuations

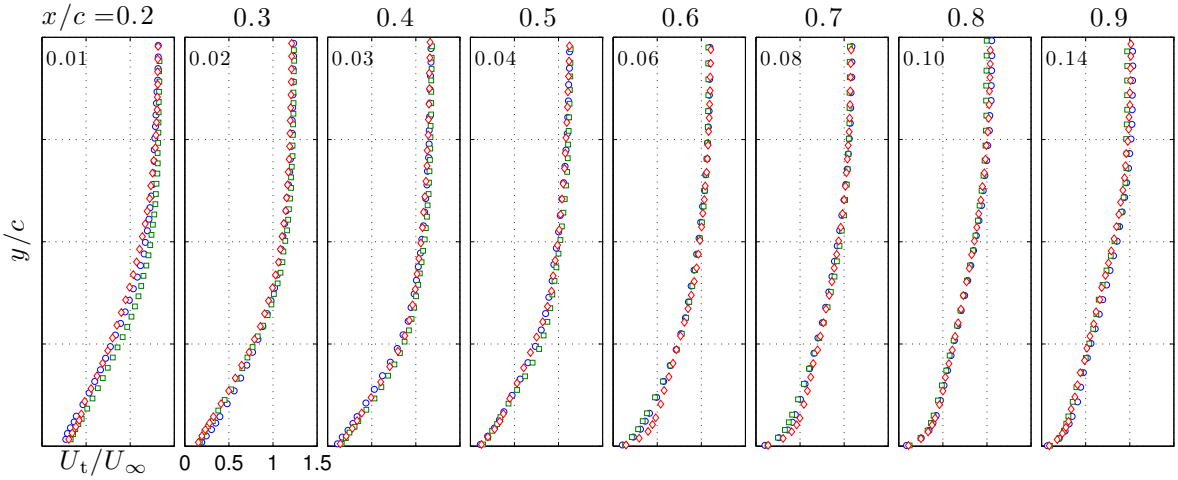

(a) $F^+ = 1$

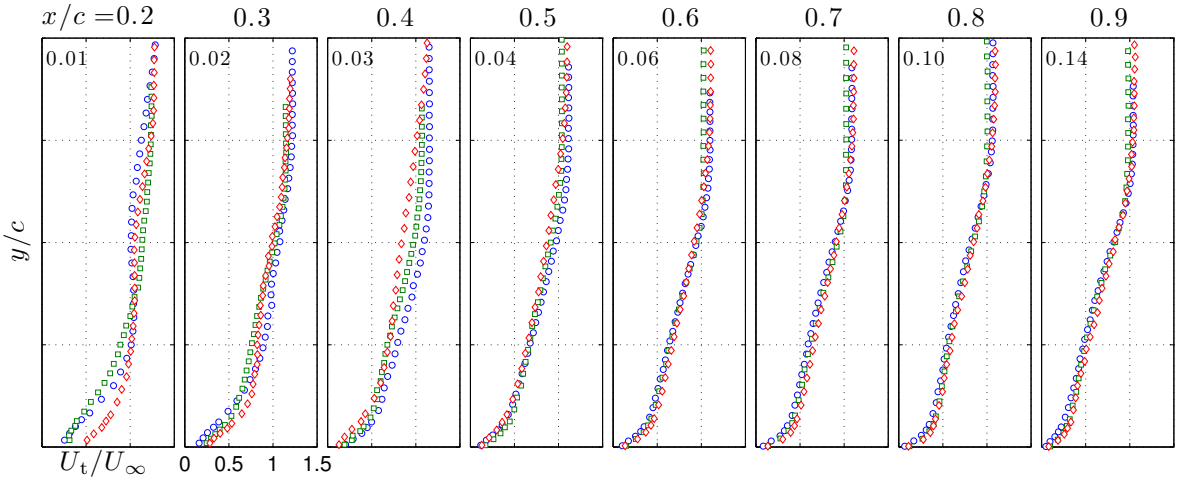

(b) $F^+ = 58$

Figure 5.16: Boundary layer velocity profiles along the chord with forcing at $-4.3 \leq x_{\mathrm{j}}^* \leq 1.3\%$ and $C_{\mathrm{B}}/C_{\mathrm{B}}^* = 2$. ($\circ$) $x_{\mathrm{j}}^* = -4.3\%$, ($\square$) $x_{\mathrm{j}}^* = -1.3\%$, ($\diamond$) $x_{\mathrm{j}}^* = 1.3\%$.

($\tilde{v} = \langle v \rangle - V$) at eight instances throughout the control cycle for $C_{\mathrm{B}} = 0.1$ at $F^+ = 1$ and 14, respectively, when forcing at $x_{\mathrm{j}}^* = -1.3\%$. Contours of the phase-averaged spanwise vorticity, $\langle \omega_Z \rangle = \partial \langle v \rangle / \partial X - \partial \langle u \rangle / \partial Y$, are also overlaid on the velocity contours. The results at $F^+ = 1$ demonstrate that the flow over the suction surface produced by the forcing is highly unsteady. At a given instant, either one or two vortical structures can be identified between regions of high and low $\tilde{v}$, which corresponds to the location of a maxima in $\langle \omega_Z \rangle$. A discrete vortex emerges near $X/c = 0.1$ at $\phi = 90°$ and convects over the airfoil surface following a trajectory that is approximately aligned with the streamwise direction. This vortex has moved beyond the trailing edge by the time $\phi = 0°$ is reached. The streamwise distance of approximately $0.7c$ travelled over 270° ($0.75/f_{\mathrm{m}}$) of the cycle

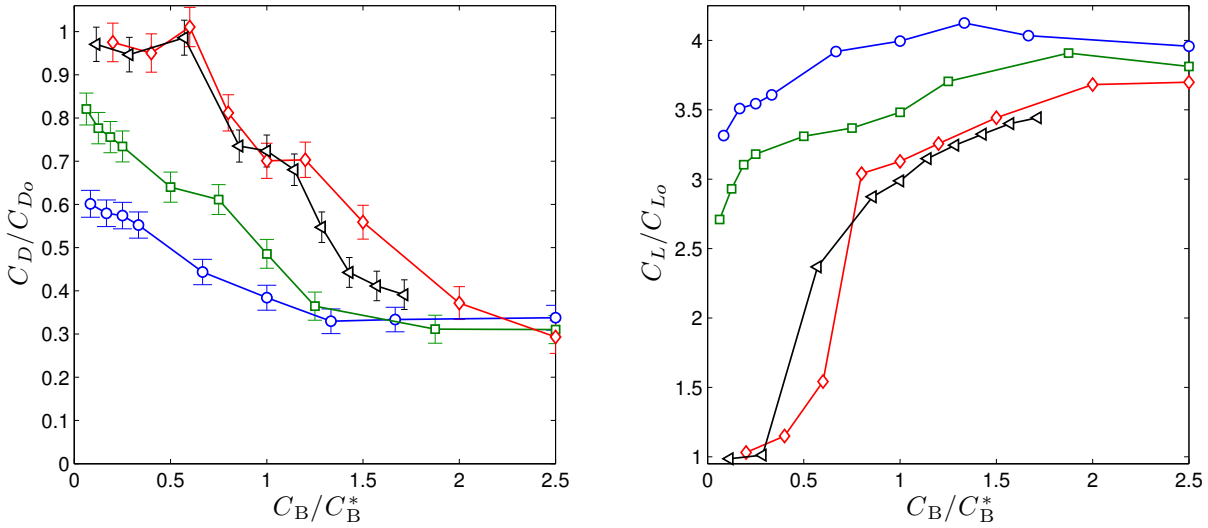

Figure 5.17: Lift and drag coefficient variation with C_B/C_B^* and slot location at $F^+ = 1$. ($\circ$) $x_j^* = -4.3\%$, ($\square$) $x_j^* = -1.3\%$, ($\diamond$) $x_j^* = 1.3\%$, ($\triangleleft$) $x_j^* = 4.3\%$.

implies that the vortices are convecting at a speed of $\sim U_\infty$. A second vortex is produced at a 180° phase offset from the first, occurring at $\phi = 270°$. Comparing phases that are 180° apart (i.e., the left column of the figure to the right column), the two vortices are qualitatively similar in size, however the second induces $\tilde{v}$ of greater magnitude in the vicinity of the vortex. The discrete vortices are formed by breaking away from a region of high magnitude vorticity that forms in the shear layer over approximately $-0.05 \leq X/c \leq 0.2$ in the region downstream of the synthetic jet. These results show that this form of low amplitude control at $F^+ = 1$ leads to what is effectively an organization of the large scale vortex shedding that is present in the wake of the baseline, stalled flow. The time-averaged result of the organized passage of vortices over the suction surface downstream of the synthetic jet is a laminar separation bubble (as evidenced by the mean flow field in Figure 5.10 and the C_p distribution in Figure 5.5(a)) and thus benefits to mean C_L and C_D. It is anticipated that the highly unsteady flow described in Figure 5.18 would also lead to lift and drag fluctuations of considerable magnitude.

The behaviour of the flow over the control cycle for $F^+ = 14$ at $C_B = 0.1$ shows significant differences compared to $F^+ = 1$. Large vortices advecting over the surface like with $F^+ = 1$ are not present, instead a region of vorticity downstream of $X/c \approx 0.3$ that does not vary in size is observed. Forcing at $F^+ = 14$ produces vortices that are much smaller in size and that follow a trajectory closer to the airfoil surface relative to $F^+ = 1$. Compared to $F^+ = 1$, these small vortices lead to a smaller region of unsteady

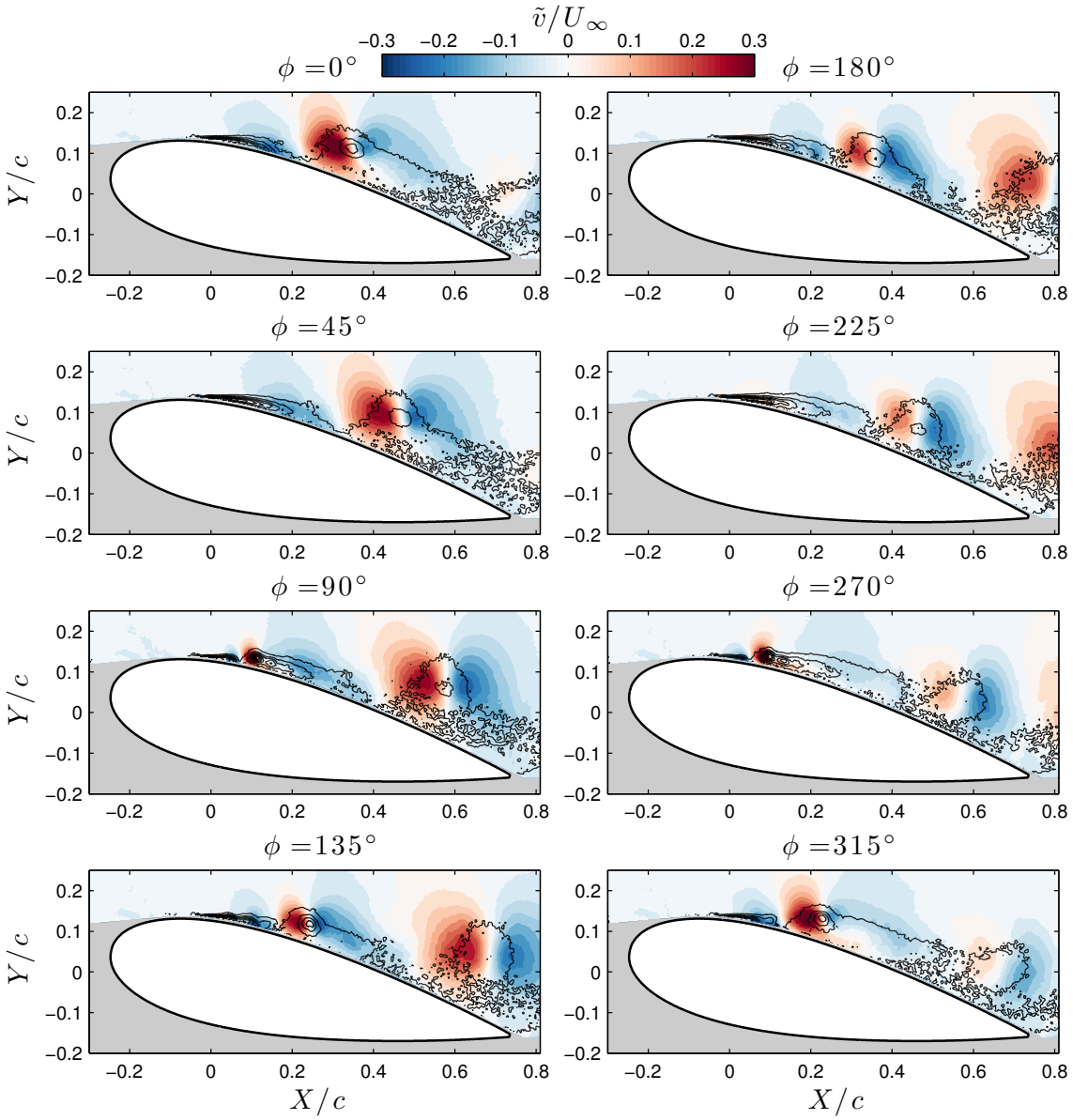

Figure 5.18: Contours of coherent transverse velocity fluctuations at $F^+ = 1$ and $C_B = 0.1$ for $x_j^* = -1.3\%$. Phase-averaged vorticity contours are overlaid in black.

flow where substantial $\tilde{v}$ is observed near the surface over $0 \leq X/c \leq 0.3$. A detailed view of this region is shown for clarity in Figure 5.20 at a phase angle $\phi = 135°$. Despite the lack of data in the near wall region, clear regions of opposing sign $\tilde{v}$ are present and coincide with concentrations of phase-averaged vorticity. Approximately five such vorticity concentrations can be visually identified at each phase during the cycle. The results presented in Figures 5.18 and 5.19 provide insight into the cause of the monotonic decrease in C_D with increasing F^+ shown in Figure 5.2b. Up to a limit, the number of

vortical structures produced by the forcing that are present during a cycle increases with F^+. Assuming an approximately constant convection speed, an increase in F^+ implies smaller and weaker vortices being produced. The reduction in the size of the vortices as F^+ is increased from 1 to 14 allows their center of rotation to maintain a trajectory closer to the airfoil surface, which results in a thinner time-averaged boundary layer near the trailing edge, as was shown in Figure 5.13. It follows that the thinner boundary layer causes less displacement of the streamlines relative to the baseline case, resulting in a narrower wake and reduced drag. The same is not true of the lift coefficient, as C_L for $F^+ = 1$ is greater than $F^+ = 14$ at this blowing ratio. This may be due to the large vortices at $F^+ = 1$ transporting high-momentum fluid from the external flow to the boundary layer over the control cycle, leading to a larger chordwise region of reduced pressure on the suction surface relative to $F^+ = 14$. This is similar to the findings of Buchmann et al. [16], who showed that there was a net entrainment towards the wall along the path of the vortices when forcing at $F^+ = 1$.

Figures 5.21 and 5.22 show coherent velocity fluctuations for $F^+ = 1$ and 14, respectively, at $C_\mathrm{B} = 1$. At $F^+ = 1$, several differences are observed relative to the lower blowing ratio case at $C_\mathrm{B} = 0.1$. Most notably is that rather than two vortices being shed during one control cycle, there is a single vortex that moves in a trajectory along the airfoil surface. This vortex emerges near $X/c = 0.1$ at $\phi = 90°$ (as evidenced by the opposing sign regions of transverse velocity) and has a shape that is considerably skewed in comparison to those at the lower blowing ratio. The *Q-criterion* method [50], which identifies vortices as locations where the vorticity tensor dominates over the rate of strain, confirmed that these locations of skewed vorticity surrounded by $\tilde{v}$ of opposite sign do indeed correspond to a passing vortex. Since a single vortex is present during the cycle but travels approximately the same distance, the convection speed in this case is a factor of two smaller, $\sim 0.5U_\infty$. Figure 5.5b shows that in the time-averaged sense the flow is fully attached, however it is evident that considerable coherent unsteadiness remains. Similar to increasing F^+ at a given C_B, the fact that increasing C_B causes the shed vortices to follow a trajectory closer to the surface leads to a substantial decrease in drag (Figure 5.2b). The results for $F^+ = 14$ in Figure 5.22 show much more resemblance to the lower blowing ratio case, where small vortices can be observed in the boundary layer. It is important to notice the scale of $\tilde{v}$ in Figure 5.22, which is an order of magnitude smaller than in Figure 5.19, showing that the increase in blowing ratio for $F^+ = 14$ in fact results in vortices of lower strength. However, unlike forcing at the low blowing ratio of $C_\mathrm{B} = 0.1$, evidence of these relatively weak vortices persisting to the trailing edge is observed. This is not visually apparent in the phase-averaged vorticity, but regularly

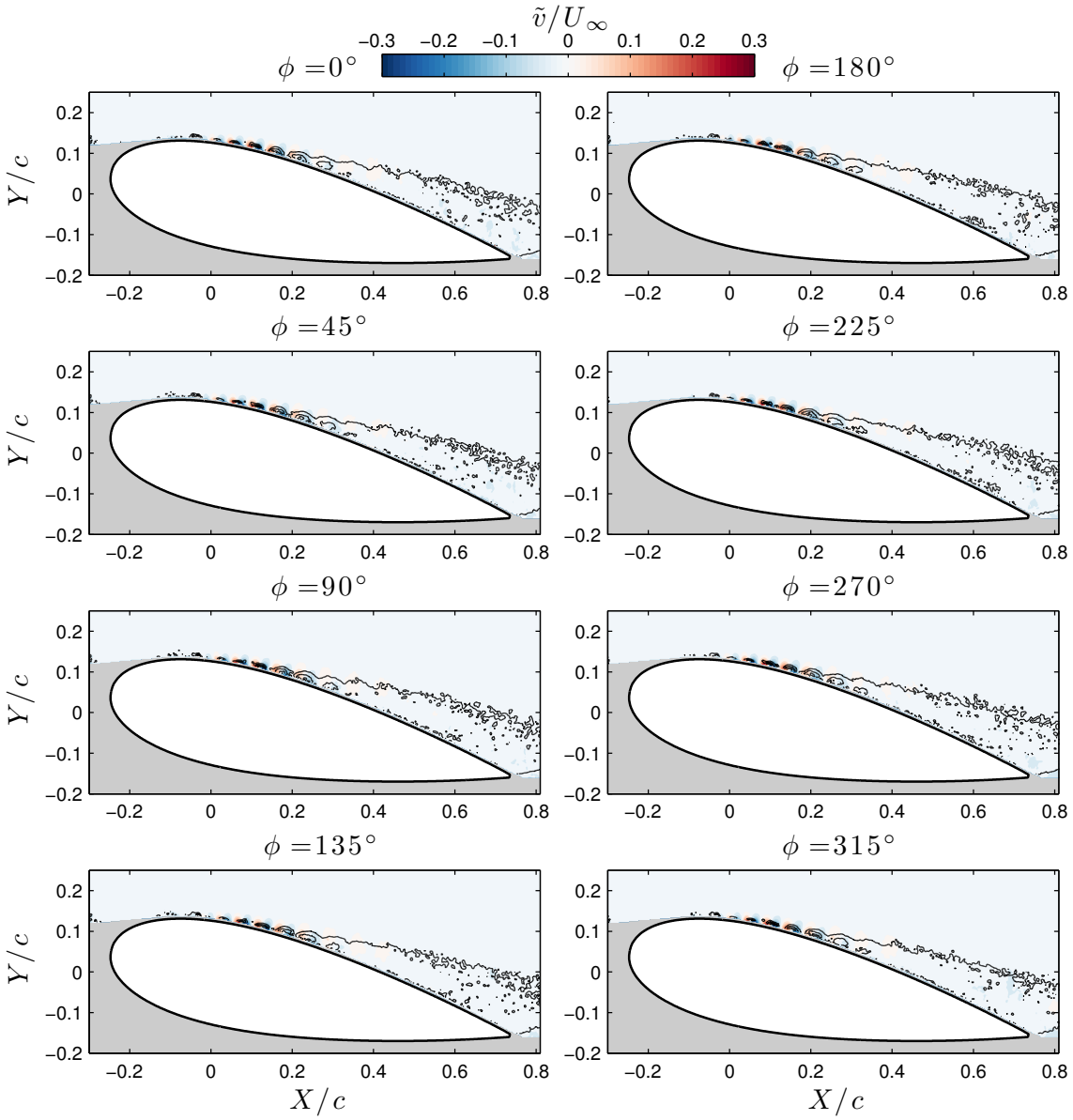

Figure 5.19: Contours of coherent transverse velocity fluctuations at $F^+ = 14$ and $C_\mathrm{B} = 0.1$ for $x_\mathrm{j}^* = -1.3\%$.

spaced concentrations of $-\tilde{v}$ can be observed near the trailing edge, which were found to be consistent with locations satisfying the Q-criterion. This transition of vortices persisting towards the trailing edge as the blowing ratio increases from $C_\mathrm{B} = 0.1$ to 1 agrees with previous results from Feero et al. [26], where the unsteadiness of the controlled flow was assessed using velocity spectra in the wake. It was shown that with increasing excitation amplitude at $F^+ = 9.9$, the flow was initially attached with no apparent peak in the velocity spectrum, but once a certain excitation amplitude was reached a sharp

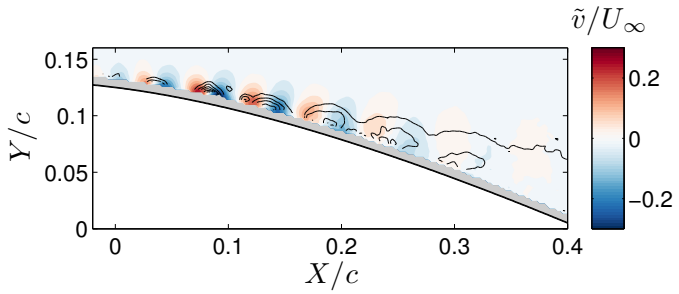

Figure 5.20: Detailed view of the coherent velocity/vorticity field at $\phi = 135°$ for $F^+ = 14$ from Figure 5.19.

peak at $f^+ \approx 5$ emerged and grew in magnitude. Compared with forcing at $F^+ = 1$, this peak was smaller in magnitude relative to the broadband level of the spectrum. This result also compares well with the present flow field measurements that show relatively large scale unsteadiness when forcing at $F^+ = 1$, but only small scale unsteadiness when forcing in the range of the shear-layer instability at $F^+ = 14$.

Boundary layer velocity spectra measured at $y = \delta^*$ along x for $F^+ = 1$ and 58 at $x_j^* = -1.3\%$ and $C_B/C_B^* = 1$ (the same cases as Figure 5.15) are shown in Figure 5.23. Successive spectra are stepped by an order of magnitude. Consistent with the phase-averaged flow fields presented for $F^+ = 1$ in Figures 5.18 and 5.21, the spectra show a dominant peak at the control frequency $F^+ = 1$. A cascade of peaks at the harmonics of $f^+ = 1$ are also observed due to the modulation of the control signal by a square wave. As x/c increases, the high-frequency harmonics begin to decrease in magnitude relative to the broadband spectrum level until $x/c = 0.9$ where peaks up to only $f^+ = 4$ are visible. The magnitude of the spectral peaks decreases with increasing order of the harmonic (i.e., the peak at $f^+ = 2$ is lower than at $f^+ = 1$). The magnitude of the peak at $f^+ = 1$ is larger than that at the carrier frequency $f^+ = 58$ by several orders of magnitude, which shows that the dynamics of the controlled flow are dominated by the forcing frequency $F^+ = 1$. Identifying a chord location where the boundary layer becomes turbulent is not straightforward from the velocity spectra as the spectral content due to the unsteady flow produced by the forcing does not lead to a typical turbulent spectrum shape. However, apart from the peak at $f^+ = 1$ and its harmonics at $x/c = 0.4$, the spectrum shows a shape that is flat followed by decay at high-frequency typical of turbulent flow. The velocity spectra for high-frequency control at $F^+ = 58$ show considerably different behaviour than $F^+ = 1$. A peak is observed at $f^+ = 58$ that is of significant magnitude relative to the low frequency level of the spectrum at $0.2 \leq x/c \leq 0.3$, but at $x/c \geq 0.4$ the peak becomes very narrow and its magnitude relative to the broadband spectrum level

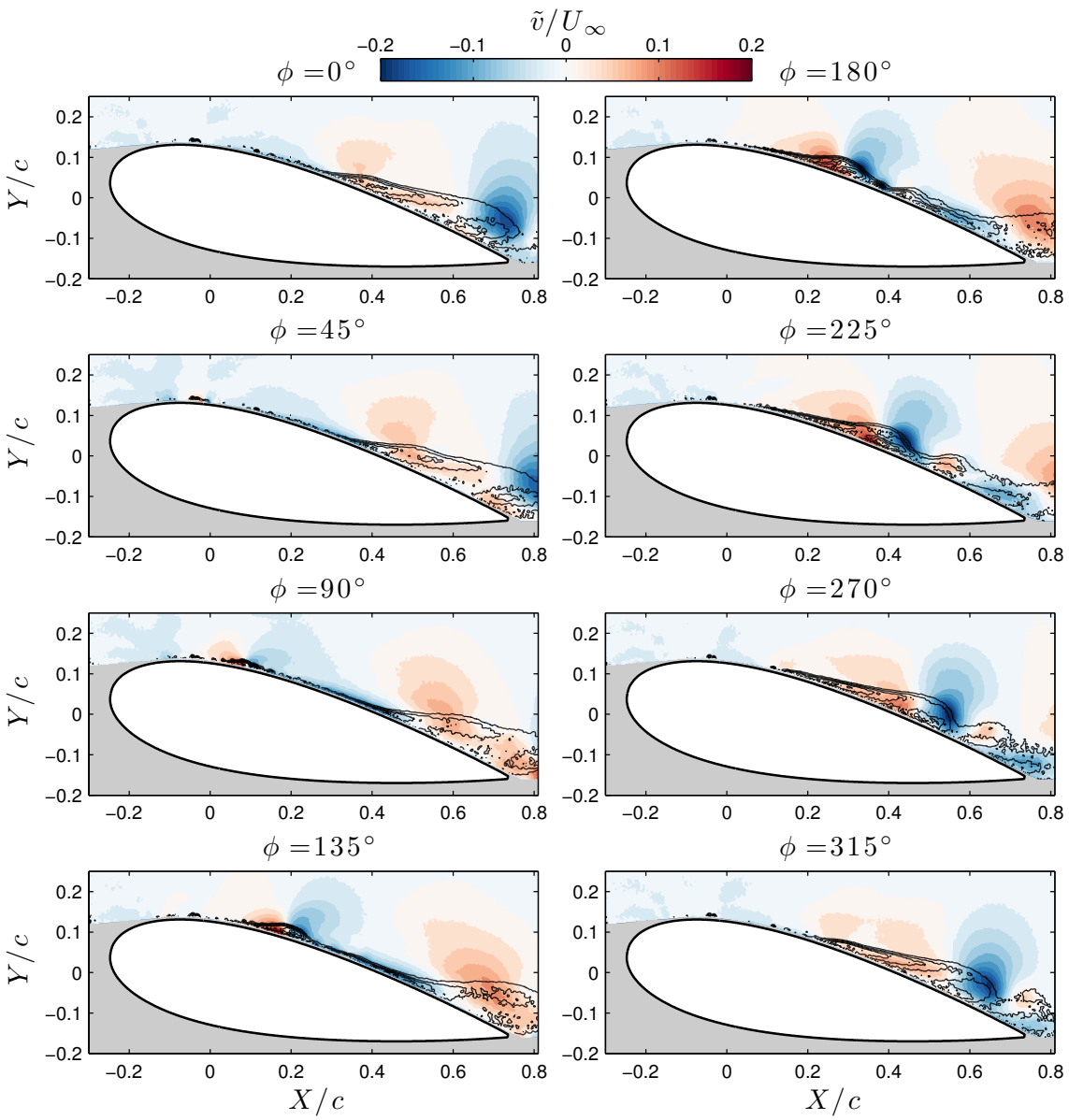

Figure 5.21: Contours of coherent transverse velocity fluctuations at $F^+ = 1$ and $C_\mathrm{B} = 1$ for $x_\mathrm{j}^* = -1.3\%$.

is small. Furthermore, the evolution of the velocity spectra shows more resemblance to the baseline flow (Figure 3.18), where the spectra are initially laminar and transition to turbulence with an amplified band of frequencies. As discussed in regards to the baseline velocity spectra, the peak at $f^+ \approx 2.4$ is not physical but is associated with traverse vibrations. In this case, the band of amplified frequencies has a central frequency of approximately $f^+ = 25$, as opposed to the baseline flow that has a central frequency of $f^+ = 18$. Typical turbulent spectra are observed once $x/c = 0.5$ is reached, which agrees

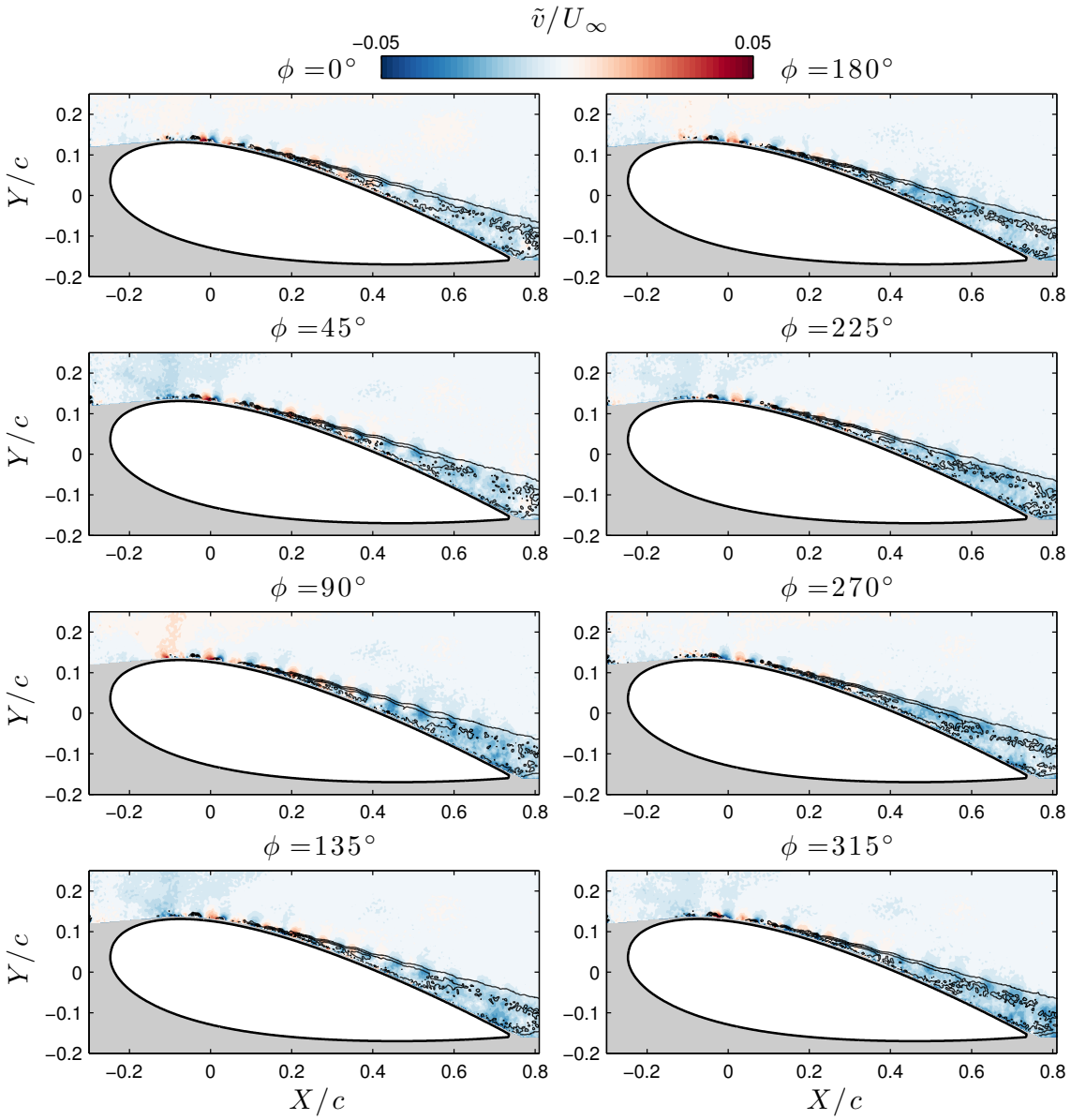

Figure 5.22: Contours of coherent transverse velocity fluctuations at $F^+ = 14$ and $C_B = 1$ for $x_j^* = -1.3\%$. Note that the scale for $\tilde{v}/U_\infty$ in this figure is smaller than in Figure 5.19.

with the change in the shape of the velocity profiles from $x/c < 0.5$ to $x/c \geq 0.5$ in Figure 5.15b. The velocity spectra at $F^+ = 58$ suggest that unlike $F^+ = 1$, where the time-averaged effects of the forcing are the result of unsteady flow, the controlled flow is likely steady. That is, at $F^+ = 1$ the flow is only fully attached in the time-averaged sense, whereas at $F^+ = 58$ the flow remains fully attached at all times. This will be discussed subsequently by considering a decomposition of the velocity into turbulent and

coherent fluctuations.

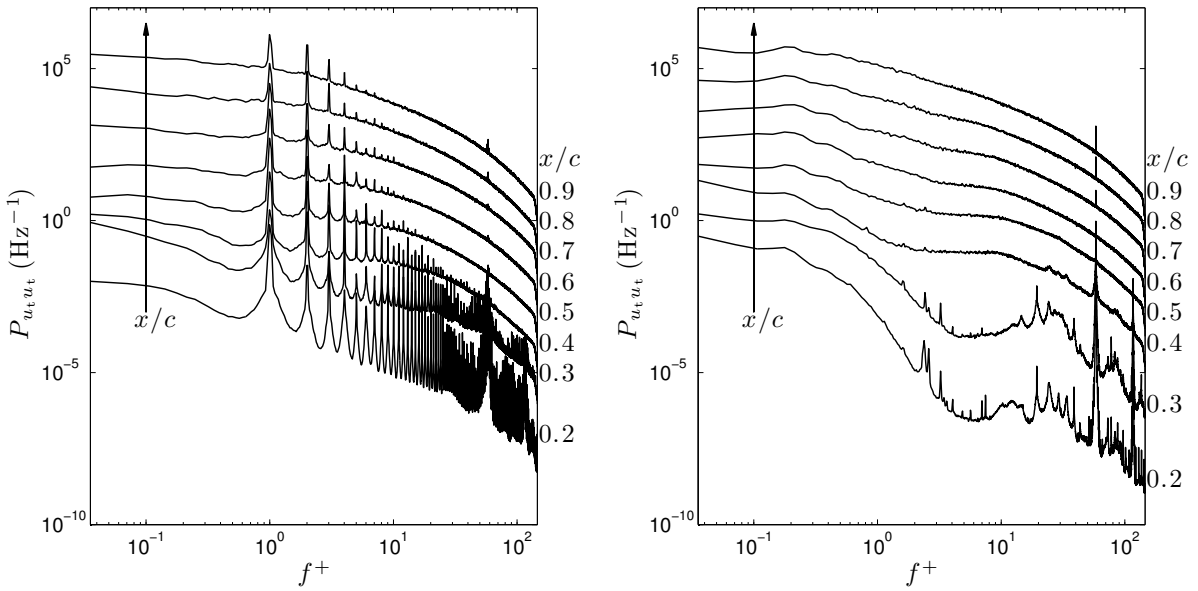

(a) $F^+ = 1$ (b) $F^+ = 58$

Figure 5.23: Boundary layer velocity spectra along the airfoil chord for $x_{\mathrm{j}}^* = -1.3\%$ at $C_{\mathrm{B}}/C_{\mathrm{B}}^* = 1$.

Similar results are presented in Figure 5.24 for the larger relative blowing ratio case, $C_{\mathrm{B}}/C_{\mathrm{B}}^* = 2$ (see Figure 5.16 for corresponding mean profiles). The spectra at $F^+ = 1$ are qualitatively quite similar to those at $C_{\mathrm{B}}/C_{\mathrm{B}}^* = 1$, although the magnitude of the peak at $f^+ = 1$ relative to the broadband spectrum level has increased. The location where, apart from the dominant unsteadiness, the flow may be considered turbulent remains similar at $x/c \approx 0.4$–0.5, which agrees with the shape of the mean velocity profiles in Figure 5.16. The magnitude of the peak at the carrier frequency $f^+ = 58$ is slightly larger owing to the increase in C_{B}. At this larger $C_{\mathrm{B}}/C_{\mathrm{B}}^*$, the spatial development of the velocity spectra for $F^+ = 58$ shows several differences. Over the chordwise range $0.2 \leq x/c \leq 0.9$, there is no region of laminar flow with a spatial growth of amplified frequencies, as was shown at $C_{\mathrm{B}}/C_{\mathrm{B}}^* = 1$. The high-frequency range of the spectrum at the first measurement station $x/c = 0.2$ is dominated by a broad peak at $f^+ = 58$ and its harmonic $f^+ = 116$ due to the increase in C_{B} causing localized unsteadiness near the synthetic jet. The velocity spectra downstream of this at $x/c \geq 0.3$ show shapes typical of a turbulent flow, which suggests that the increase in C_{B} leads to an earlier transition. An interesting observation at $F^+ = 58$ is the low frequency peak at $f^+ = 0.8$ for $x/c = 0.2$.

This peak decreases in magnitude moving downstream, until $x/c = 0.4$ where it is no longer apparent. As discussed previously, a small region of separation just downstream of the slot was identified by an inflectional mean velocity profile at $x/c = 0.2$. The localized peak in the velocity spectra near this location suggest the shedding of vortical structures from this small separation bubble at a frequency of $f^+ = 0.8$. However, the fact that the peak does not persist to the trailing edge suggests that the unsteadiness is local, while globally the flow remains steadily attached. Similar behaviour occurred when forcing at $F^+ = 58$ for the other slot locations (i.e. peaks at $f^+ \approx 0.8$ were observed near the synthetic jet).

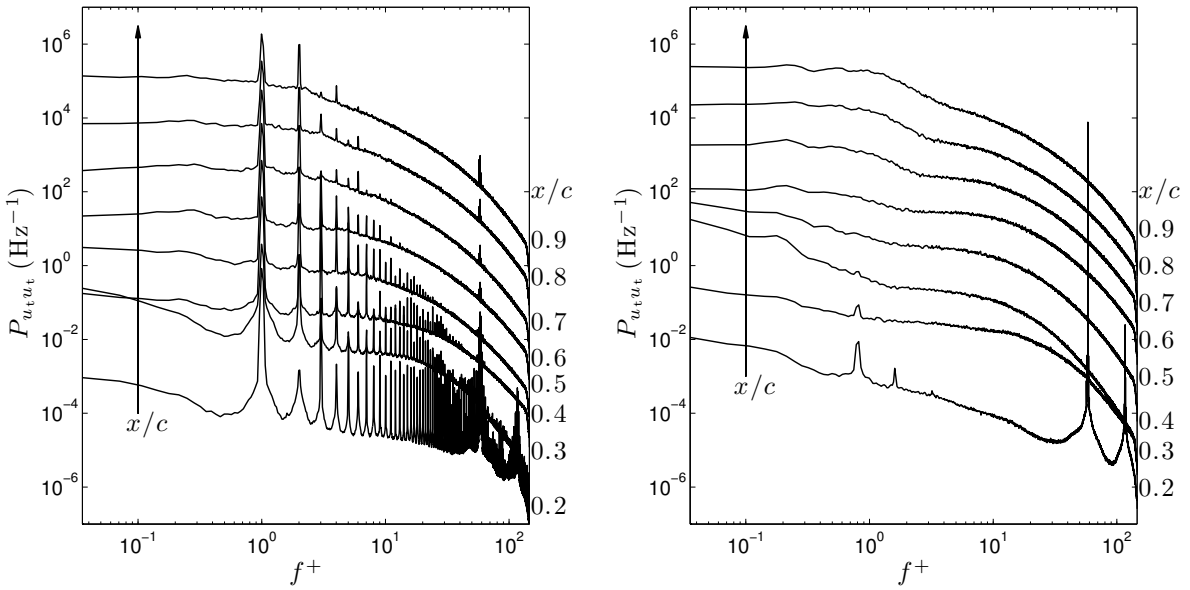

(a) $F^+ = 1$ (b) $F^+ = 58$

Figure 5.24: Boundary layer velocity spectra along the airfoil chord for $x_j^* = -1.3\%$ at $C_B/C_B^* = 2$.

The triple decomposition methodology described in Section 2.8 was used to extract the coherent and turbulent fluctuations for boundary layer velocity profiles at $F^+ = 1$ and 58 to compare the effects of low- and high-frequency forcing on the dynamics of the controlled flow. The 'coherent' fluctuations are those that occur as the result of phase-averaging, and are thus a direct result of the periodic control input. The turbulent fluctuations are instantaneous deviations from the phase-averaged cycle, as defined by equation (2.5). An example of the decomposition of a typical velocity signal into the time-average, coherent fluctuations and turbulent fluctuations for $F^+ = 1$ is shown in Figure

5.25. At this particular measurement location in the figure, the instantaneous velocity is shown to primarily follow $\langle u_t \rangle$, although there are also deviations from the phase-average occurring over part of the cycle. Both the instantaneous and phase-averaged velocity show fluctuations at the carrier wave frequency ($f^+ = 58$), but these tend to be larger in an instantaneous cycle, which contributes to the magnitude of the turbulent fluctuations. The RMS magnitudes of the coherent and turbulent fluctuations are $\tilde{u}_{t,rms}/U_\infty = 0.10$ and $u'_{t,rms}/U_\infty = 0.06$, respectively.

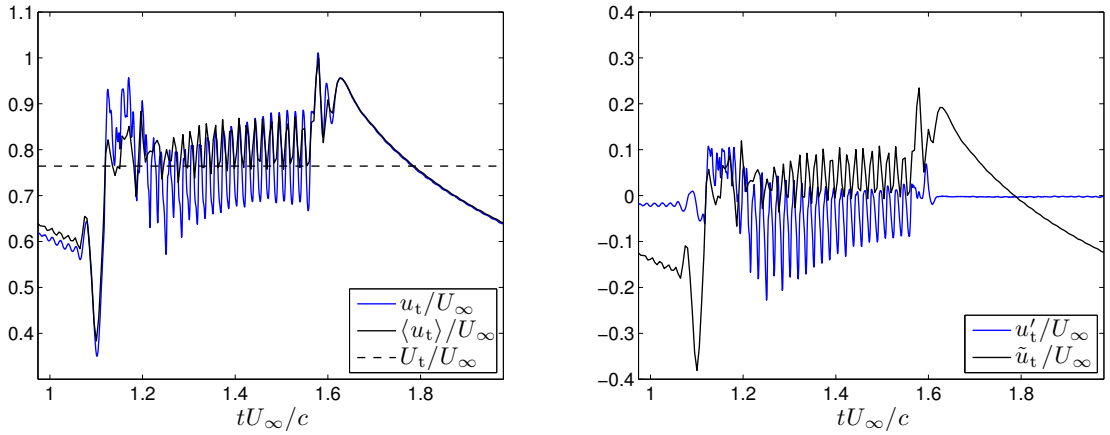

(a) Instantaneous, phase-averaged, and time-averaged velocities.

(b) Turbulent and coherent fluctuations.

Figure 5.25: Triple decomposition of a typical velocity signal measured at $x/c = 0.2$ and $y \approx 0.5\delta$ for $F^+ = 1$, $C_B/C_B^* = 1$ and $x_j^* = -1.3\%$. A portion of the time-series containing one control cycle is shown.

Figure 5.26 shows the coherent and turbulent RMS velocity profiles for four control cases at $C_B/C_B^* = 1$: $F^+ = 1$ and 58 at the most upstream and downstream slot locations, $x_j^* = -4.3\%$ and 4.3%. Also included in Figure 5.26(a) is the evolution of the RMS velocity over the suction surface for the baseline flow as reference for the control cases. The RMS velocity profiles are normalized by U_∞ over $x/c = 0.2$ – 0.9. The wall-normal coordinate, y, has been normalized by δ to account for the drastic boundary layer growth along the chord. Over this chordwise range, the baseline $u'_{t,rms}$ grows from approximately $0.1U_\infty$ to $0.2U_\infty$. The width of the peak in u'_{rms}/U_∞ is centered near $\sim 0.8\delta$ and becomes wider as x increases along the chord and the separated shear layer becomes thicker.

In terms of the control cases, the results for $F^+ = 1$ will first be considered. When forcing is applied upstream of separation at $x_j^* = -4.3\%$, the magnitude of the coherent and turbulent fluctuations are similar, until $x/c \geq 0.7$ where the turbulent fluctuations begin to dominate. This is in exception to $x/c = 0.2 - 0.3$ (near the jet location) where

there are substantial coherent fluctuations throughout the boundary layer. For forcing at $x_j^* = 4.3\%$, in the region close to excitation, the magnitude of the coherent fluctuations near the wall are much larger and they dominate over the turbulent fluctuations. Once $x/c = 0.5$ is reached, $u'_{t,rms}$ begins to dominate and become larger than $\tilde{u}_{t,rms}$ through most of the boundary layer. Compared with $x_j^* = -4.3\%$, there is greater turbulent energy away from the wall, with a broad peak in $u'_{t,rms}$ observed at $x/c > 0.5$ and its maximum located near $y/\delta \approx 0.5$. This broad distribution of larger turbulent fluctuations in the boundary layer coincides with a thicker boundary layer for downstream forcing at $F^+ = 1$ (Figure 5.15a). For each forcing location, the coherent fluctuations are consistent with the passage of vortices over the airfoil throughout the cycle as shown in Figures 5.18 and 5.20.

The behaviour for $F^+ = 58$ is substantially different than $F^+ = 1$ in that for each forcing location, the coherent fluctuations are negligible (except nearest the synthetic jet for $x_j^* = 4.3\%$). This is indicative of flow that is steadily attached, and agrees with the velocity spectra presented in Figure 5.23(b). When forcing is applied upstream of separation, there are larger turbulent fluctuations in the outer part of the boundary layer for $x/c \leq 0.5$ compared with the downstream case. There is also a rapid growth of the fluctuations, as can be seen by comparing the $u'_{t,rms}$ profiles at $x/c = 0.2$ and 0.3 for $x_j^* = -4.3\%$. At $x/c = 0.2$ the magnitude of the fluctuations for the downstream forcing case is much larger, likely associated with the fact that the blowing ratio necessary for reattachment is significantly larger than the upstream case. This chord location is the only one for $F^+ = 58$ where substantial coherent fluctuations are also observed, which is due to the proximity to the synthetic jet and the larger C_B relative to $x_j^* = -4.3\%$. Similar to forcing at $F^+ = 1$, a broader distribution of $u'_{t,rms}$ with a maximum near $y/\delta \approx 0.5$ is observed near the trailing edge for $x_j^* = 4.3\%$, whereas a larger peak near the wall is present for $x_j^* = -4.3\%$. This is consistent with a thicker trailing edge boundary layer for $x_j^* = 4.3\%$ than $x_j^* = -4.3\%$ with forcing at $F^+ = 58$ (Figure 5.15b).

Similar results are presented in Figure 5.27 for the larger relative blowing ratio $C_B/C_B^* = 2$. As mentioned in regards to the mean velocity profiles in Figure 5.16, $C_B/C_B^* = 2$ was not attainable at $F^+ = 58$ for $x_j^* = 4.3\%$, thus upstream forcing at $x_j^* = -4.3\%$ is compared to downstream forcing at $x_j^* = 1.3\%$. For $F^+ = 1$ at the upstream slot location, a substantial increase in the near-wall coherent fluctuations is observed at $x/c \leq 0.3$ when compared with $C_B/C_B^* = 1$ (Figure 5.26a). The coherent fluctuations are shown to dominate over the turbulent fluctuations up to $x/c = 0.6$, and downstream of this $\tilde{u}_{t,rms}$ and $u'_{t,rms}$ are of similar magnitude throughout the boundary layer. At $x_j^* = 1.3\%$, a large peak of $\tilde{u}_{t,rms}/U_\infty = 0.3$ is observed near the wall

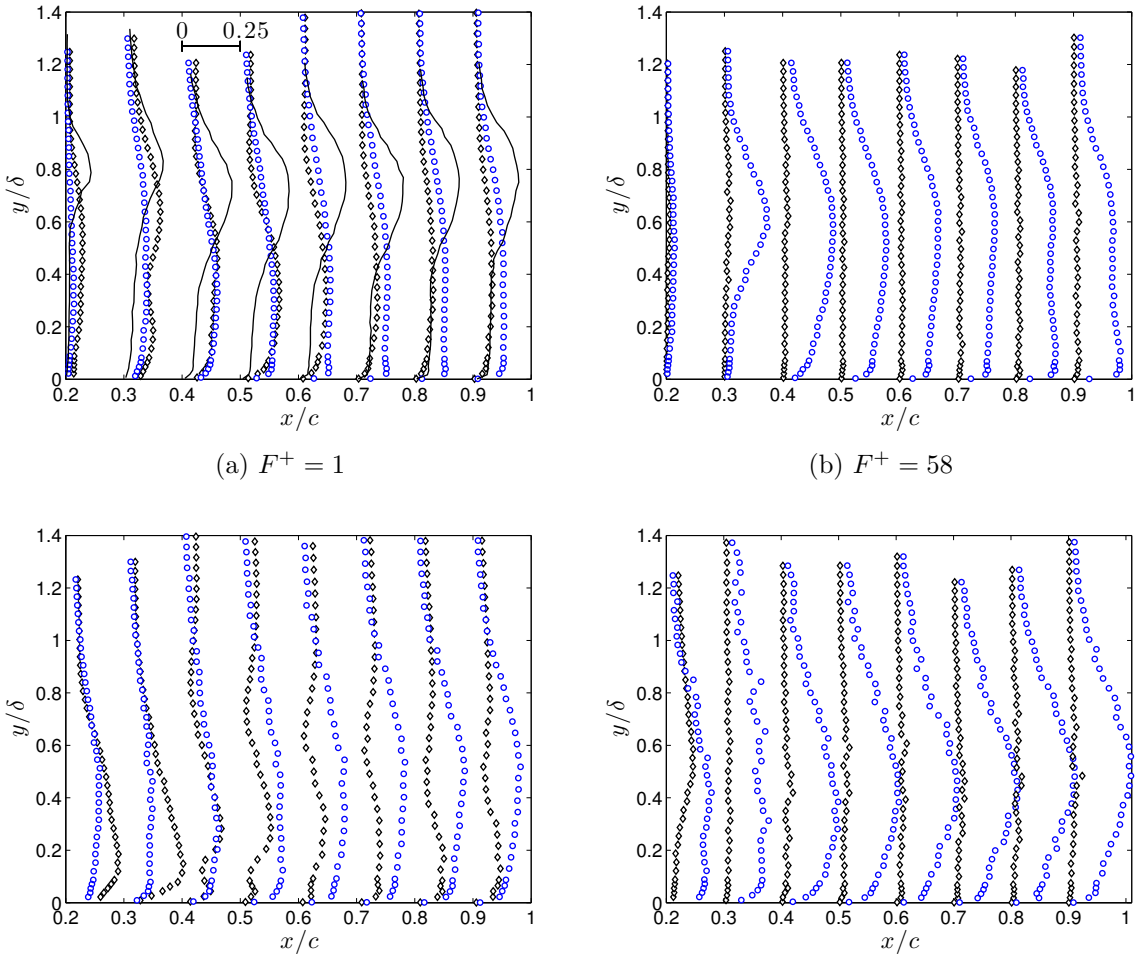

(a) $F^+ = 1$ (b) $F^+ = 58$

(c) $F^+ = 1$ (d) $F^+ = 58$

Figure 5.26: Coherent and turbulent RMS velocity profiles at $x_j^* = -4.3\%$ (a, b) and $x_j^* = 4.3\%$ (c, d) for $C_\mathrm{B}/C_\mathrm{B}^* = 1$. ($\circ$) $u'_{\mathrm{t,rms}}/U_\infty$, ($\diamond$) $\tilde{u}_{\mathrm{t,rms}}/U_\infty$. The scale for the RMS velocity profiles and $u'_{\mathrm{t,rms}}/U_\infty$ for the baseline flow (shown by the solid line) are given in (a).

at $y/\delta \approx 0.2$ for $x/c = 0.2$. The chordwise growth of turbulent fluctuations is more rapid at this slot location, with $u'_{\mathrm{t,rms}}$ becoming similar in magnitude to $\tilde{u}_{\mathrm{t,rms}}$ over all y/δ at $x/c \geq 0.4$. This is unlike the downstream forcing case at $C_\mathrm{B}/C_\mathrm{B}^* = 1$, where turbulent fluctuations were found to dominate in the outer region of the boundary layer near the trailing edge. Thus, the increase in $C_\mathrm{B}/C_\mathrm{B}^*$ causes strong coherent fluctuations to persist over the entire chordwise extent downstream of the synthetic jet slot when forcing at $F^+ = 1$. In general, both the coherent and turbulent RMS velocity profiles show very similar shapes over the extent of the measurement domain. The results for high-frequency forcing at $F^+ = 58$ are similar to $C_\mathrm{B}/C_\mathrm{B}^* = 1$: other than at $x/c = 0.2$,

the coherent velocity fluctuations are negligible, indicative of steadily attached flow. The coherent fluctuations are substantial relative to the turbulent fluctuations at $x/c = 0.2$ for each slot location, and are even slightly larger near the edge of the boundary layer at $y/\delta \approx 0.8$. The coherent fluctuations are due to oscillations at the control frequency $F^+ = 58$ and would not include contributions from the low-frequency peak at $f^+ = 0.8$ that was shown in the velocity spectra in Figure 5.24(b). Unlike $C_\mathrm{B}/C_\mathrm{B}^* = 1$, the shape and magnitude of $u'_{\mathrm{t,rms}}$ is similar between the upstream and downstream forcing cases over the airfoil chord. A dominant peak near the wall at $y/\delta \approx 0.1$ develops rapidly and is present over $0.3 \leq x/c \leq 0.5$, downstream of which the turbulent fluctuations become more evenly spread out over a large portion of the boundary layer covering approximately $0.1 \leq y/\delta \leq 0.8$. The similarity of $u'_{\mathrm{t,rms}}$ between the two slot locations is also observed in the mean velocity profiles (Figure 5.16b). The results concerning the mean and RMS velocity profiles, for both $F^+ = 1$ and 58, show that as C_B is increased to a level well above C_B^*, the effect of slot location on the controlled flow becomes less significant. This is not surprising since forcing at a large blowing ratio such as $C_\mathrm{B}/C_\mathrm{B}^* = 2$ represents a 'brute force' type strategy, where benefits that may be gained by optimizing the slot location at relatively low excitation amplitudes are suppressed by the high amplitude excitation.

5.4 Summary

The chapter discusses the effect of control parameters on the aerodynamic forces, the mean flow and the flow dynamics, which forms the main results of this thesis. A saturation in both C_D and C_L with increasing C_B was generally observed for all F^+ and x_j^*. The most effective control was achieved when forcing at $F^+ = 14$ and $x_\mathrm{j}^* = -4.3\%$, the most upstream forcing location. $F^+ = 14$ was most effective in minimizing drag, while $F^+ = 1$ maximized lift. When forcing at C_B pre-saturation, the trend in C_D was found to be consistent with the boundary-layer thickness near the trailing edge. Differences in the mean flow for varying x_j^* were observed when forcing at $C_\mathrm{B}/C_\mathrm{B}^* = 1$, however at $C_\mathrm{B}/C_\mathrm{B}^* = 2$ forcing location had minimal effect. The flow was shown to be globally unsteady when forcing at $F^+ = 1$ with one or two large vortices advecting over the surface during a cycle, while at $F^+ = 14$ the unsteadiness was localized and a larger number of much smaller vortices were produced. In contrast, high-frequency forcing at $F^+ = 58$ was found to produce a steadily attached flow. This was shown both from velocity spectra, and a decomposition of the boundary layer velocity into turbulent and coherent fluctuations. Coherent fluctuations were negligible at $F^+ = 58$. Compared with

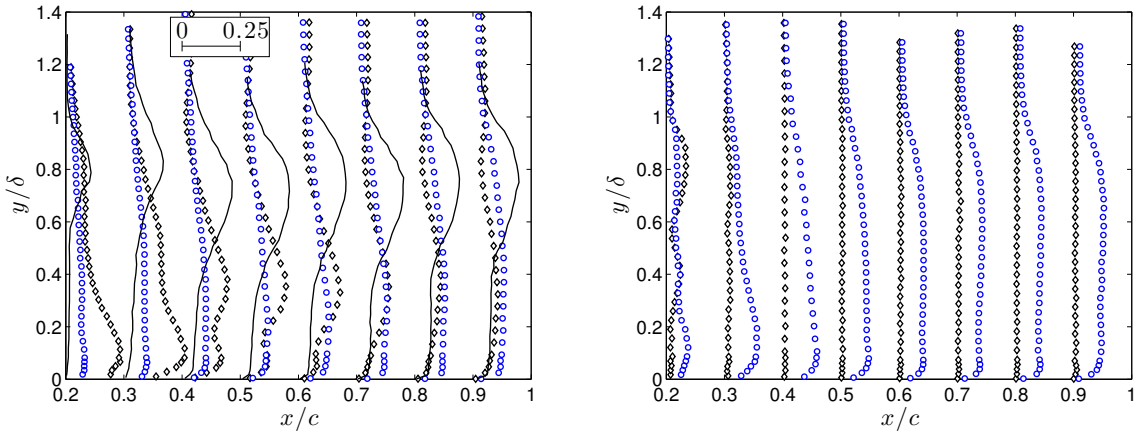

(a) $F^+ = 1$ (b) $F^+ = 58$

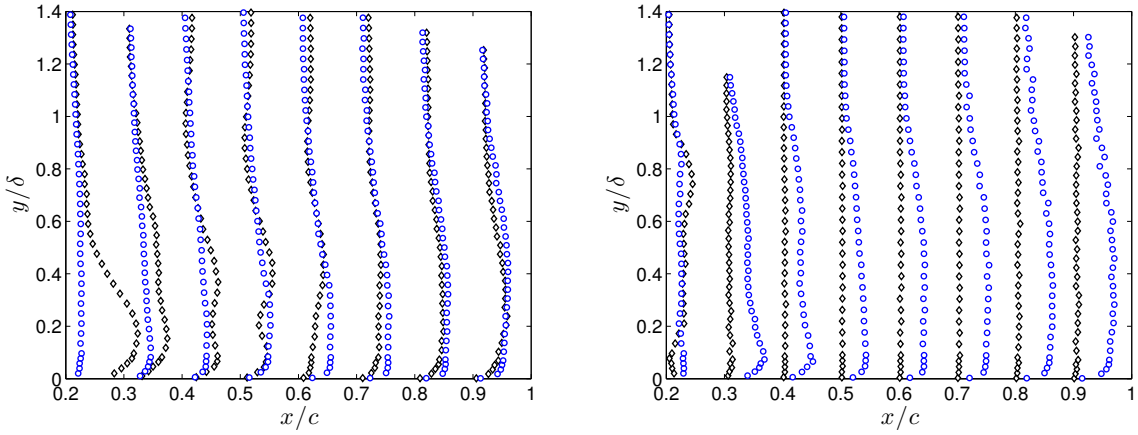

(c) $F^+ = 1$ (d) $F^+ = 58$

Figure 5.27: Coherent and turbulent RMS velocity profiles at $x_j^* = -4.3\%$ (a, b) and $x_j^* = 1.3\%$ (c, d) for $C_\mathrm{B}/C_\mathrm{B}^* = 2$. ($\circ$) $u'_{\mathrm{t,rms}}/U_\infty$, ($\diamond$) $\tilde{u}_{\mathrm{t,rms}}/U_\infty$.

forcing upstream of separation, downstream forcing for both $F^+ = 1$ and 58 led to a broader distribution of turbulent fluctuations away from the wall.

Chapter 6

Controlled Flow Three-Dimensionality

This chapter focuses on an investigation into the three-dimensionality of the controlled flow. The previous chapter discussed section lift and drag coefficients, and flow field measurements at midspan with the assumption that the flow in this plane would be representative of a model where control is applied over the entire span. This assumption was based on knowledge that the baseline flow being controlled can be considered two-dimensional (Section 3.1), and the synthetic jet produces a relatively uniform forcing input over the length of the slot (Section 4.2) that covers 33% of the model span. However, edge effects are expected since the slot does not cover the full span. The edge effects were studied both qualitatively using surface flow visualization with tufts and oil film, and quantitatively with flow field measurements by PIV at several XY planes along the span.

6.1 Flow visualization

Prior to the tuft flow visualization, the baseline C_p distribution at $\alpha = 12°$ and $Re_c = 125,000$ was measured with and without tufts attached to the model to ensure that they did not affect the flow. Note that unlike the results discussed in previous chapters where experiments were performed at $Re_c = 100,000$, the flow visualization was done at a slightly higher Reynolds number $Re_c = 125,000$ ($U_\infty \approx 6.3$ m/s). This was done to facilitate the oil film visualization since the surface shear stresses were too low at $Re_c = 100,000$ ($U_\infty \approx 5$ m/s) to form oil streaks. At the increased Reynolds number, the baseline C_p distribution in Figure 6.1 shows that the flow remains stalled. The cases with and without the tufts show negligible differences, indicating that the tufts did not

affect the flow in a substantial way. A surface pressure distribution is also provided for a control case at $C_\mathrm{B} = 1$ and $F^+ = 47$, where C_p indicates that the flow is fully attached at midspan. This result was typical of other F^+ values at the same blowing ratio. The flow visualization and spanwise PIV results were obtained for a single slot location, $x_\mathrm{j}^* = -1.3\%$.

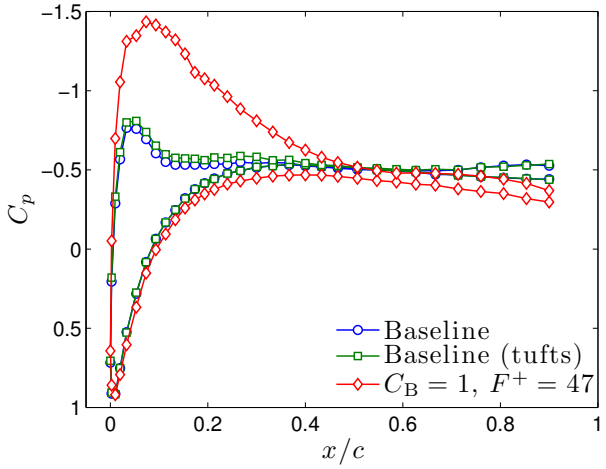

Figure 6.1: Midspan pressure coefficient distribution at $\alpha = 12°$ and $Re_c = 125,000$ under baseline conditions (with and without tufts) and with control.

The flow near the surface of the airfoil under baseline and control conditions was visualized using tufts for $C_\mathrm{B} = 1$ and $F^+ = 0.5$, 1, 2, 12 and 47. To visualize unsteady flow regions, photographs were taken with an exposure time of 2 seconds, which corresponds to approximately $43T_\mathrm{I}$ ($22T_\mathrm{I}$ for $F^+ = 0.5$), where T_I is the integral time scale. This causes tufts in regions of unsteady flow to appear blurry and an approximate range of motion can be visualized from the photos.

The tuft flow visualization results are shown in Figure 6.2. In the baseline case, motion can be seen in almost all the tufts and few are aligned with the mean flow direction, typical of a region where the flow is separated. The most motion is observed in the row of tufts closest to the trailing edge. When control is applied for each F^+ value: the flow does not appear to be attached over the entire span of the synthetic jet, the spanwise extent of the attached flow decreases towards the trailing edge, there is significant flow in the spanwise direction at the edges of the attached region, and the size of the attached region appears similar. The lines in Figure 6.2 indicate the estimated bounds of the attached region. The amount by which the span of the attached flow region contracts in the streamwise direction can be quantified as the ratio of the spanwise length of the attached flow in the first row of tufts to the fourth row. The approximate spanwise

extent of the attached flow at $x/c = 30\%$ is $0.9c$ and reduces to $0.4c$ at $x/c = 85\%$, giving a ratio of 44%. At $F^+ = 0.5$ and 1, significant unsteadiness can be observed in the tufts in the attached region other than very near $z/c = 0$, which is indicative of the expected unsteadily attached flow. For $F^+ \geq 2$, the flow appears to be steady in the attached region. While three-dimensionality of the reattached flow due to the finite span of the synthetic jet and edge effects is not unexpected, the extent by which the span of the reattached flow decreases in the streamwise direction is substantial.

Because oil film visualization is not well suited for unsteady flows, the oil experiments were limited to $F^+ = 12$ (i.e. forcing in the range of f_{sl}^+) and 47 (i.e. high-frequency forcing) where the fully attached flow is known to be essentially steady in time (Section 5.3). The effect of F^+ on the shape of the attached region for constant $C_B = 1$ is shown in Figure 6.3. The solid black region indicates separated flow where the oil has not moved due to the low shear stress at the wall. Near the edges of the area where the oil was applied, there are some streaks from accumulated oil flowing due to gravity. The viscosity of the oil/pigment mixture had to be optimized such that it was low enough to be affected by the relatively low wall shear stresses, but large enough not to flow due to gravity on the inclined surface of the airfoil. The results show that the spanwise extent of the attached flow near mid chord and the trailing edge are similar for the two F^+ values, while just downstream of the slot it appears that the flow is attached over almost the entire span of the slot for $F^+ = 12$. For $F^+ = 47$, the flow is attached over approximately $-0.4 \leq Z/c \leq 0.4$ just downstream of the slot.

The effect of C_B on the three-dimensionality of the reattached flow was also investigated to determine whether increasing C_B would decrease the severity of the edge effects that cause the contraction of the attached flow region. At $F^+ = 47$, three blowing ratios were considered: $C_B = 1$, 2 and 2.5 (the largest blowing ratio possible at the given U_∞). As C_B is increased (Figure 6.4), the spanwise extent of the attached region increases and the edge effects become less severe (i.e., there is less of a contraction of the attached flow in the streamwise direction). As estimated from the oil images, the spanwise extent of the attached flow at $x/c = 0.9$ increases from $0.43c$, $0.49c$, to $0.56c$ for $C_B = 1$, 2 and 2.5, respectively. The spanwise extent of the attached flow near the trailing edge at $C_B = 1$, $0.43c$, compares very well to the value of $0.4c$ estimated from the tuft visualization. It is also interesting to note the 'finger-like' structures in the attached region. While it is possible that this is a product of the oil visualization, these may qualitatively indicate the presence of secondary spanwise structures. Sahni et al. [67] performed experiments with a finite span synthetic jet on a NACA 4421 airfoil and observed the presence of secondary structures for blowing ratios from $C_B = 0.2$ to 1.2. Furthermore, they found that the

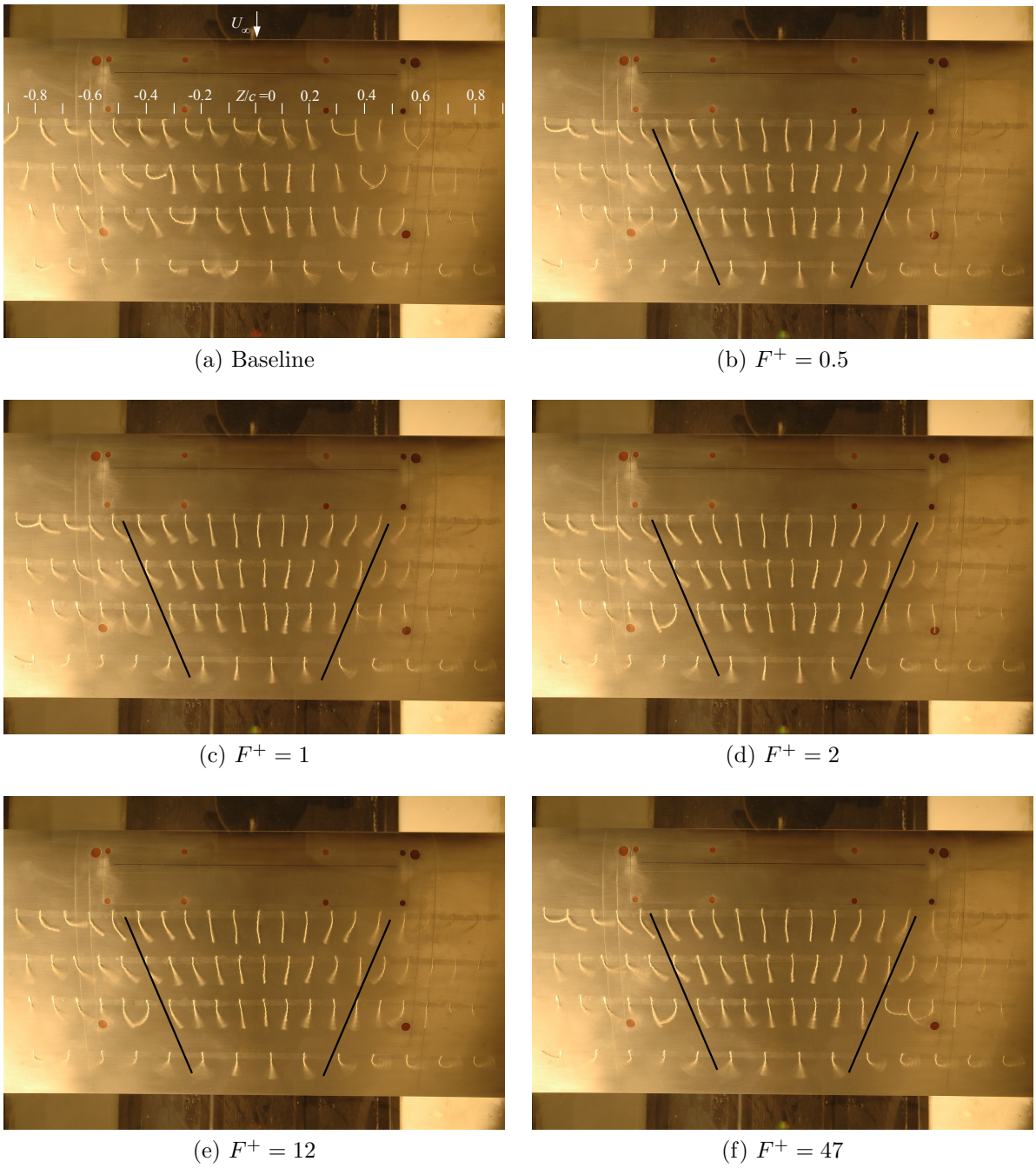

(a) Baseline

(b) $F^+ = 0.5$

(c) $F^+ = 1$

(d) $F^+ = 2$

(e) $F^+ = 12$

(f) $F^+ = 47$

Figure 6.2: Tuft flow visualization of the flow on the suction surface at $Re_c = 125,000$ for a range of F^+ at constant $C_\mathrm{B} = 1$.

spanwise wavelength of these structures increased with increasing blowing ratio and the channeling of the tracer material in Figure 6.3 seems to show similar behaviour. In their case, the baseline flow appears to be attached (likely with a laminar separation bubble), and may differ from the case of a baseline stalled flow. Smith and Glezer [71] showed the

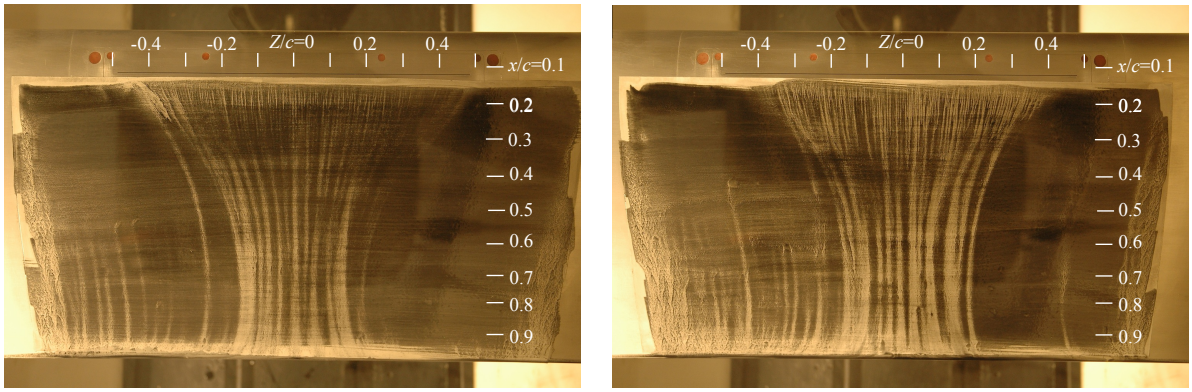

(a) $F^+ = 12$ (b) $F^+ = 47$

Figure 6.3: Oil visualization at $F^+ = 12$ and 47 at constant $C_B = 1$.

existence of spanwise structures forming in the near-field region of a rectangular synthetic jet with aspect ratio 150 in quiescent conditions. The spanwise structures, observed by smoke visualization, were found to have a spacing of approximately 2.5 slot widths. If similar behaviour occurred in the presence of a pressure gradient, this may be the cause of the apparent spanwise structures observed in this study. A quantitative investigation of these possible secondary structures would require measurements such as volumetric PIV or planar PIV in streamwise-spanwise planes parallel with the airfoil surface such that the Z component of velocity could be measured. Such an investigation was outside the scope of the present work.

6.2 Velocity field measurements

The spanwise variation in the controlled flow was also investigated quantitatively using planar PIV measurements in the XY plane at four different locations: $Z/c = 0$, -0.17, -0.33 and -0.5. This range covers the half-span of the synthetic jet slot, as shown in Figure 2.7b. The mean total velocity and the mean streamlines are shown for each of the four spanwise locations in Figure 6.5 for $F^+ = 58$ and $C_B = 1$, which can be compared to the surface oil visualization in Figure 6.4(a). At $Z/c = 0$ and -0.17, the flow is attached over the entire suction surface and shows very similar behaviour at these two planes. The boundary layer at $Z/c = -0.17$ becomes moderately thicker towards the trailing edge relative to midpsan. Once $Z/c = -0.33$ is reached, the flow separates at a location downstream of the synthetic jet slot (i.e. a location downstream of the baseline separation point) and does not reattach. The flow at $Z/c = -0.5$ resembles that of

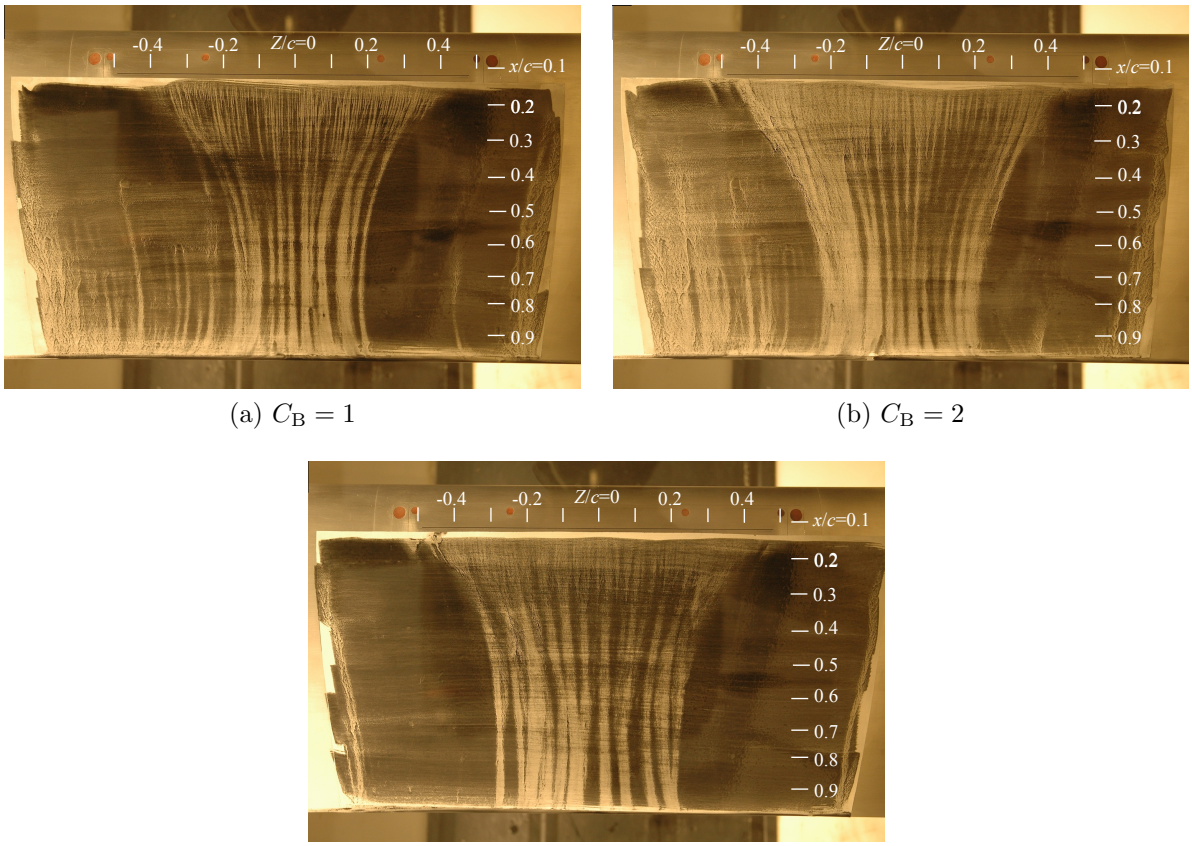

(a) $C_B = 1$

(b) $C_B = 2$

(c) $C_B = 2.5$

Figure 6.4: Oil visualization at $F^+ = 47$ with increasing blowing ratio.

the baseline flow (Figure 3.9a) and indicates that the control has essentially no effect on the flow at the slot edges. This behaviour agrees very well with the oil visualization, which suggests that the area affected by control where the flow is attached over the entire chord covers the range $-0.2 \leq Z/c \leq 0.2$. The delayed separation point in the plane at $Z/c = -0.33$ shows the effect on control is reduced at this plane, which is also reflected in the oil visualization.

A case that could not be investigated using oil visualization due to highly unsteady flow, $F^+ = 1$ at $C_B = 0.1$, was also considered using PIV measurements. As shown in Figure 5.5(a), this case corresponds to the formation of a laminar separation bubble on the suction surface. The U_T fields at planes along the span are shown in Figure 6.6. Evidence of a LSB is observed at both $Z/c = 0$ and -0.17 by the curvature of streamlines near the surface beginning at $X/c \approx 0$, followed by attached flow over the remainder of the chord. The flow at $Z/c = -0.17$ is quite similar to midpsan, although as in Figure 6.5, a thicker boundary layer near the trailing edge is seen. Dramatic changes occur at

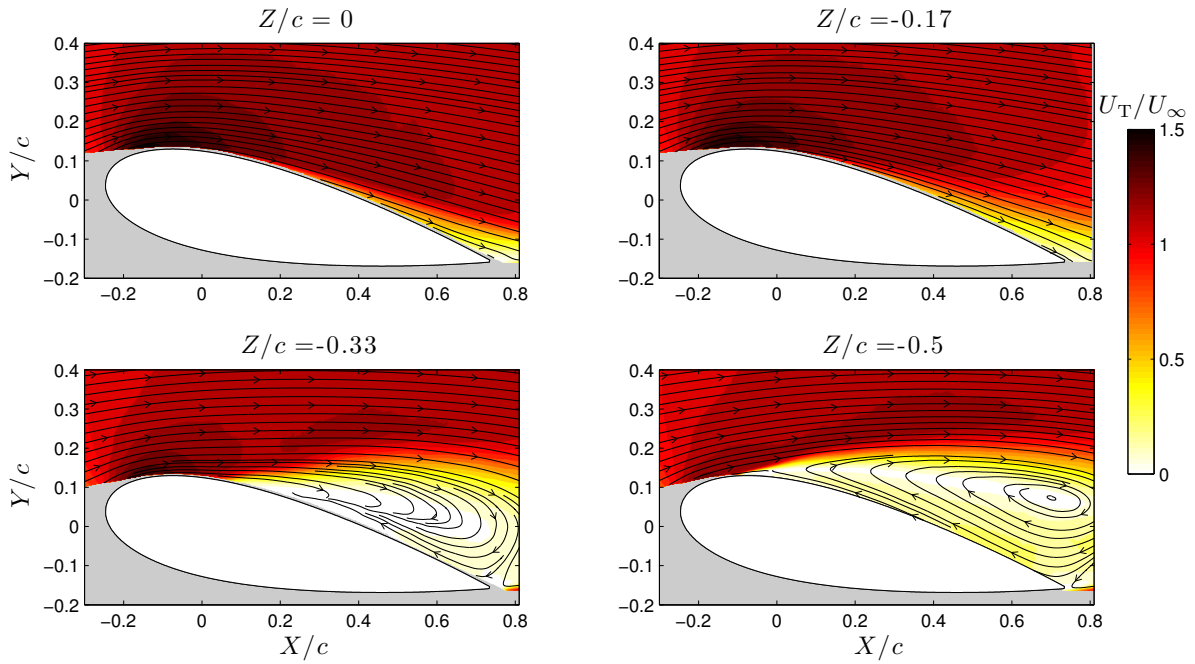

Figure 6.5: Contours of mean total velocity in the XY plane at $C_B = 1$ and $F^+ = 58$ over $-0.5 \leq Z/c \leq 0$.

$Z/c \leq -0.33$ where the flow separates without reattaching. These results demonstrate that even at the low blowing ratio case where a LSB occurs at midpsan due to control, the flow is relatively uniform in the spanwise direction over $-0.17 \leq Z/c \leq 0.17$.

6.3 Summary

Surface flow visualization techniques and planar PIV measurements at different spanwise locations were used to determine the extent to which edge effects were present due to control with the long, but finite synthetic jet slot. The attached flow with control at different F^+ and C_B demonstrated three-dimensionality in the form of a contraction of its spanwise extent from just downstream of the slot towards the trailing edge. Oil visualization revealed that as C_B was increased from 1 to 2.5, the contraction of the attached flow decreased and the flow became attached over a larger spanwise extent. When considering the global effect of control on the flow, the results demonstrate that increasing the blowing ratio increases the size of the reattached flow region and would therefore increase lift and decrease drag for the entire airfoil model. This has implications for measurement techniques that quantify lift/drag improvements at midspan versus those that measure the global forces. In the context of the present investigation, the fact that

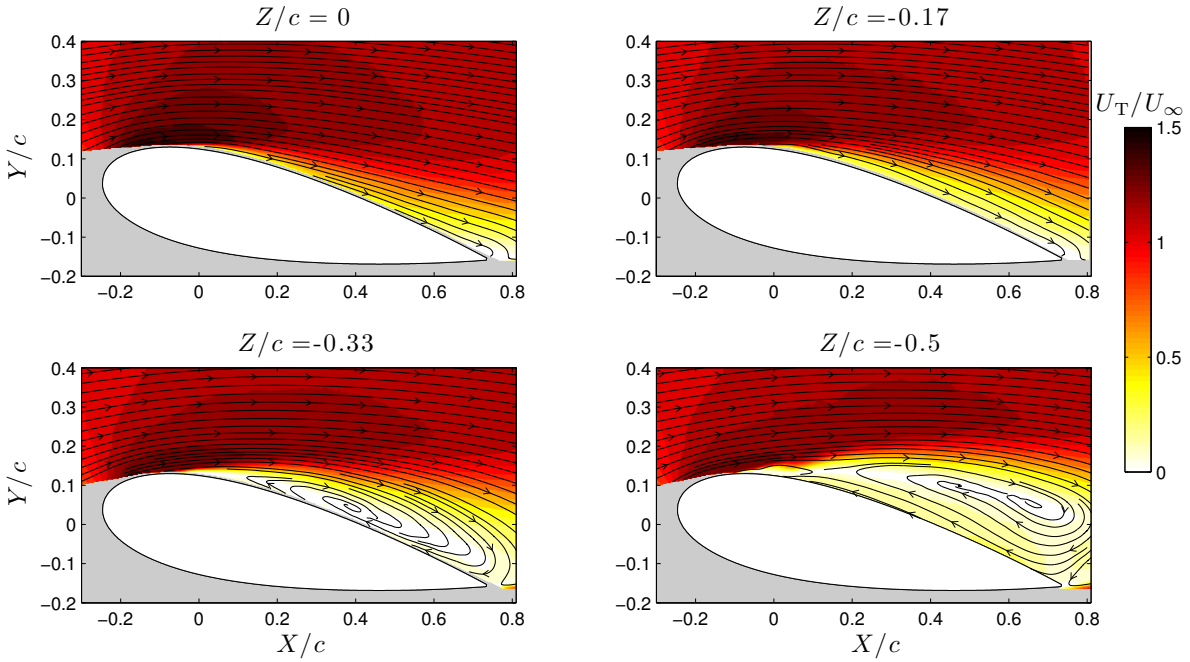

Figure 6.6: Contours of mean total velocity in the XY plane at $C_B = 1$ and $F^+ = 1$ over $-0.5 \leq Z/c \leq 0$.

the synthetic jet covers approximately $0.33b$ of the model span and provides spanwise uniform forcing leads a region over which the spanwise variation in the controlled flow is small. Edge effects were found to be significant over approximately $|Z|/c > 0.2$, which is also equivalent to $|Z|/L > 0.2$. Thus, the measurements at midspan discussed in Chapter 5 are relevant over the central 40% span covered by the synthetic jet slot. It is assumed that the flow in this region is representative of a model having control over the entire span (i.e. $L = b$).

Chapter 7

Conclusions and Recommendations

7.1 Conclusions

The control of boundary layer separation on a NACA 0025 airfoil at $Re_c = 100,000$ and $\alpha = 12^\circ$ using a synthetic jet actuator was investigated using wind tunnel experiments. A fixed Reynolds number and angle-of-attack corresponding to post-stall separated flow were selected to focus on the effects of control parameters. The control parameters of interest were the excitation amplitude, C_μ, frequency, F^+, and the slot location relative to separation, x_j^*. The effect of slot location on the controlled flow, with a particular focus on the forcing location relative to separation and maintaining constant injection angle, had previously received little attention in the literature, with a notable absence of detailed experimental studies.

Prior to the control experiments, considerable effort was spent in characterizing the baseline flow. This included not only a detailed study of the flow at midspan, but also the two-dimensionality of the baseline flow. Due to the inherent sensitivity of low Reynolds number airfoil experiments to model/facility related factors, spanwise uniformity of the flow was not taken for granted. In particular, the presence of gaps between the model ends and the tunnel walls was compared to the use of end plates. Velocity measurements in the wake with gaps present showed that not only was the flow non-uniform along the span, it was asymmetric about midspan. The fact that even small gaps of $0.003c$ caused substantial spanwise variations in the flow, and noticeably affected C_L at midspan, confirmed the necessity of end plates. With end plates fixed to the model ends, the baseline flow was symmetric about midspan and the deviation of U in the wake relative to midspan was within 4% over approximately $|Z|/c \leq 0.5$ (i.e. the central third of the model span). Furthermore, the spanwise variation of integral boundary layer parameters were found to be primarily within $\pm 5\%$ at $x/c = 0.1$. The flow at midspan was studied

using a combination of velocity measurements by hot-wire and PIV. From boundary layer velocity profiles obtained over $x/c = 0.2$ – 0.9, the results showed close agreement in δ from each measurement technique. Despite relatively large regions of reversed flow measured incorrectly by hot-wire, the trend in δ^* was very similar but was underestimated by the hot-wire velocity, however significant differences in both the magnitude and trend were observed for θ. An important aspect for the control experiments was accurately determining the mean separation point, since the synthetic jet slot was varied relative to this location. This was accomplished using several different techniques: estimating the beginning of the plateau in C_p, location $\partial U_\mathrm{s}/\partial y = 0$ from fits to boundary layer profiles, and extrapolating the location of the mean dividing streamlines. Close agreement between these different techniques gave confidence in the separation point determined as $x_\mathrm{s}/c = 0.13$. The final aspect related to the baseline flow was determining the frequencies associated with the shear layer and wake instabilities. Velocity spectra in the wake and in the boundary layer along the airfoil chord were used to identify $f_\mathrm{w}^+ = 1$ and $10 \leq f_\mathrm{sl}^+ \leq 26$. The transition from laminar to turbulent flow in the boundary layer followed the expected behaviour where a band of unstable frequencies emerged downstream of separation and were amplified spatially.

An equally important detail of the control experiments was the characterization of the synthetic jet velocity at the slot exit plane. Bench-top measurements of the synthetic jet velocity at the jet centerline, and along the major axis of the slot were performed using hot-wire. The frequency response of $\overline{U_\mathrm{j}}$ showed a maxima at $f_\mathrm{e} = 1000$ Hz, where $\overline{U_\mathrm{j}} = 16$ m/s could be achieved by varying the input voltage amplitude. This frequency was selected as the ideal operating frequency of the SJA as it led not only to an acceptable maximum $\overline{U_\mathrm{j}}$, but also a relatively uniform velocity profile along the major axis of the high aspect ratio slot ($d = 0.5$ mm and $L = 294$ mm). An initial design that sought to maximize $\overline{U_\mathrm{j}}$ by having the cavity Helmholtz frequency and piezoelectric diaphragm natural frequency close in magnitude showed a highly non-uniform velocity profile along the slot length. The final design alleviated this issue by having $f_\mathrm{H} = 1200$ Hz and $f_\mathrm{D} \approx 2100$ Hz, therefore the synthetic jet could operate near Helmholtz resonance and avoid the issues associated with resonance of the piezo diaphragms. Over the length of the slot, $\overline{U_\mathrm{j}}$ was found to vary within $\pm 15\%$ of the mean, while the velocity phase varied within $\pm 10^\circ$. This provided confidence for the airfoil control experiments that approximately uniform forcing was being applied to the two-dimensional baseline flow. In the context of these control experiments, forcing at 1000 Hz was equivalent to $F^+ = 58$, which was considered 'high-frequency' control. To force at frequencies in the range of f_w^+ and f_sl^+ with large enough C_B, the carrier sine wave at 1000 Hz was burst-modulated at

lower frequencies. The effect of modulation with constant 50% duty on the jet velocity with varying modulation frequency and voltage amplitude was characterized to ensure accurate determination of $\overline{U_{\mathrm{j}}}$.

The effect of control on C_D and C_L was studied for varying C_{B} at $F^+ = 1$, 2, 14 and 58, and at four slot locations symmetric about separation: x_{j}^*=-4.3%, -1.3%, 1.3% and 4.3%. The results demonstrated that for both C_D and C_L, a saturation in the control benefits was observed once a certain blowing ratio was exceeded. In the intermediate range where C_D and C_L were decreased and increased, respectively, prior to plateauing, surface pressure distributions indicated that this was due to the formation of a laminar separation bubble on the suction surface. Increasing C_{B} to the threshold value led to fully attached flow, and therefore further increasing C_{B} did not further improve C_D or C_L substantially. Both in terms of threshold C_{B} and C_L/C_D, it was observed that forcing at $F^+ = 14$, which corresponds to the range of f_{sl}^+, was most effective. Measurements for an extended number of F^+ values showed that for both pre- and post-saturation control, forcing in the range of f_{sl}^+ led to the greatest drag reduction, while forcing at f_w^+ ($F^+ = 1$) led to the greatest lift increase. The effectiveness of control was found to increase as the slot location moved upstream for both low- and high-frequency control. That is, threshold C_{B} decreased and C_L/C_D increased as the slot moved towards the leading edge. Unlike the conventional notion that forcing should be applied as close to separation as possible, these results suggest that some location upstream of separation is most effective.

The general effect of increasing C_{B} at a given F^+ on the mean flow was to decrease the thickness of the boundary layer, thereby improving C_L and C_D. A trend showing decreasing C_D with F^+ increasing from 1 to 14 at $C_{\mathrm{B}} = 0.1$ (pre-saturation) for $x_{\mathrm{j}}^* = -1.3\%$ was found to be consistent with the inverse trend in δ^* near the trailing edge. At the same blowing ratio, significantly larger magnitudes of Reynolds shear stress were observed in the boundary layer at $F^+ = 1$ and 2 compared with $F^+ = 14$. Increasing to $C_{\mathrm{B}} = 1$ led to a decrease in $\overline{uv}$ for each F^+ throughout the boundary layer.

The effect of slot location on the boundary layer was considered for $F^+ = 1$ and 58 at two values of C_{B} relative to the threshold: $C_{\mathrm{B}}/C_{\mathrm{B}}^* = 1$ and 2. At $C_{\mathrm{B}}/C_{\mathrm{B}}^* = 1$, noticeable differences were observed between $x_{\mathrm{j}}^* < 0$ (upstream forcing) and $x_{\mathrm{j}}^* > 0$ (downstream forcing) at each F^+. Generally, the downstream forcing locations led to a substantially thicker boundary layer over $x/c > 0.4$. Forcing upstream of separation led to turbulent velocity profiles near the trailing edge that were more energetic near the wall (i.e. larger near wall velocities). At $C_{\mathrm{B}}/C_{\mathrm{B}}^* = 2$, the slot location had very little effect on the mean flow in the boundary layer, and thus C_D and C_L. An ancillary investigation into the

three-dimensionality of the mean flow subject to control was performed using surface flow visualization and PIV. Both the qualitative and quantitative results demonstrated significant edge effects due to the finite slot length covering $|Z|/c \leq 0.49$, however the spanwise variation in the flow was found to be small over $|Z|/c < 0.2$ (40% of the slot length).

Phase-locked PIV measurements were used to study the dynamics of the controlled flow at $F^+ = 1$ and $F^+ = 14$. At a relatively low blowing ratio $C_\mathrm{B} = 0.1$, control at $F^+ = 1$ caused large vortices to convect over the suction surface in an approximately streamwise trajectory (i.e. moving gradually away from the airfoil surface). Forcing at $F^+ = 14$ produced a larger number of much smaller vortices relative to $F^+ = 1$. These vortices followed a trajectory close to the airfoil surface, leading to a thinner boundary layer in the time-averaged sense. Increasing to $C_\mathrm{B} = 1$ led to distorted vortices closer to the surface at $F^+ = 1$, while at $F^+ = 14$ the behaviour was similar to $C_\mathrm{B} = 0.1$ but considerably weaker vortices were produced. From both velocity spectra, and a decomposition of fluctuations into coherent and turbulent components, the controlled flow at $F^+ = 58$ was found to be essentially steady with time, unlike $F^+ = 1$ where the flow experiences large scale unsteadiness. At $C_\mathrm{B}/C_\mathrm{B}^* = 1$ for both $F^+ = 1$ and 58, forcing at $x_\mathrm{j}^* = 4.3\%$ caused a broad peak in turbulent fluctuations centered at approximately $y = 0.5\delta$ to develop, unlike $x_\mathrm{j}^* = -4.3\%$ where a near wall peak was present. Increasing to $C_\mathrm{B}/C_\mathrm{B}^* = 2$ caused coherent fluctuations at $F^+ = 1$ to persist with greater magnitude along the airfoil chord. Turbulent fluctuations because spread out relatively evenly over a large portion of the boundary layer height at $x/c > 0.5$ for $F^+ = 58$. Similar to the mean velocity profiles, the difference in velocity fluctuation magnitudes between upstream and downstream forcing at the larger relative blowing ratio was minimal. When forcing at large blowing ratio, the performance benefits that can be gained by optimizing the slot location become suppressed by the high amplitude excitation.

7.2 Recommendations for future work

The parameter space for the control of laminar boundary layer separation on an airfoil at low Reynolds number is prohibitively large for a single experimental study when considering parameters related both to the control and to the experimental conditions. The work in this thesis focused on three main control parameters for 2D forcing with fixed Reynolds number and angle-of-attack. The insight gained from this work should be used to investigate the effects of Re_c and α, with particular focus on how these parameters may affect the observed relationship between slot location and control effectiveness. Although

these two parameters are important to investigate, having one fixed while varying the other (e.g., fixed Re_c and varying α) will change the separation point and maintaining similar x_j^* would require an experimental setup with greater slot location modularity. Additional experimental conditions that could be considered include airfoil geometry (e.g., maximum thickness, camber, etc.) and freestream turbulence intensity. In terms of parameters related to control that should be explored, of particular interest is comparing 2D and 3D forcing. For 3D forcing, this introduces a potentially large number of variables related to the actuator geometry, such as the use of an array of slots or orifices, amplitude or phase modulation between individual slots/orifices, etc. A logical first step would be to compare 2D forcing from a single slot to an array of spanwise oriented slots, where the spacing between slots could be varied. Creating three-dimensional controlled flow presents a significant challenge experimentally, as measurements could no longer be confined to a single streamwise-transverse plane at midspan. Similarly, it would no longer be appropriate to measure section lift and drag, but rather the global lift and drag forces must be measured. This also implies that for the results to be meaningful, control must be applied over the entire spanwise extent of the model. Creating an array of synthetic jets with much lower aspect ratio slots is less of a challenge than a single high aspect ratio slot (like in the current study), although calibrating and ensuring each individual SJA operates at the same amplitude and phase is non-trivial.

Appendix A

Feedback Sensing

Expanding the open-loop control discussed in this thesis to closed-loop requires sensing in addition to the actuation provided by the synthetic jet. The quantity measured by the sensor(s) may be a primary quantity, such as velocity, wall shear stress or pressure, or a derived quantity such as lift or drag. This appendix chapter discusses preliminary work towards closed-loop control, specifically the choice of a quantity to be measured for feedback sensing and the associated issues for the present experiments. With the quantity to be measured and the type of sensor selected, dynamic calibration was required for which an apparatus was designed and tested. The final section will present example results of unsteady pressure measurements for baseline and open-loop control cases using the implemented sensors that were dynamically calibrated.

A.1 Sensor selection and experimental challenges

In the application of a lifting body such as an airfoil, a typical closed-loop objective function may seek the maximization of C_L/C_D or C_L subject to some penalty associated with the energy input of the actuator (e.g. [73]). The feedback sensing for this type of closed-loop controller could be realized by implementing a load cell that allows the direct measurement of lift and drag. The present experimental configuration presents several issues that preclude such a feedback sensing strategy. A load cell measures the lift and drag forces acting on the entire body, however actuation is not applied over the entire spanwise extent of the model. Thus even in an ideal case where the spanwise region covered by the synthetic jet slot experiences quasi-2D controlled flow (which is not the case, as shown in Chapter 6), the global aerodynamic loads would be affected by the regions of uncontrolled flow. If one considers a different experimental setup where the actuator covers the entire spanwise extent of the model, or where three-dimensional forc-

ing is desired (e.g., a series of spanwise or streamwise oriented slots), the low freestream dynamic pressure presents a practical difficulty for force measurement. The section drag coefficient for the current experiments at $Re_c = 100,000$ and $\alpha = 12°$, where the flow is stalled, is $C_{Do} = 0.105$, which decreases to a minimum of approximately $C_D = 0.02$ under optimum control conditions. If the global drag coefficient were equal to the section drag coefficient at midpsan (i.e. if the controlled flow were spanwise uniform over the entire span of the model), the drag force on the model would vary from 0.45 N to 0.09 N. The lift force would be moderately larger, covering a range 0.57 – 2.3 N. For commercially available load cells or even custom designed sensors, the accurate measurement of these forces (particularly the drag force) presents a considerable challenge and in many cases, the signal-to-noise ratio may be prohibitively low. Furthermore, this does not consider the magnitude of the lift and drag fluctuations, which would likely be even smaller. An alternative to measuring the lift force directly is to evaluate the section lift coefficient C_L using the surface pressure distribution according to equation (3.1). If the surface pressure over the entire surface were measured instantaneously, this would provide the means to compute the instantaneous lift coefficient.

The use of surface pressure measurements for the evaluation of the unsteady lift coefficient was evaluated for the present experiments using results from the open-loop control discussed in Chapter 5. Figure A.1(a) shows the change in the mean lift coefficient ($\Delta C_L = C_L - C_{Lo}$) as a function of the change in pressure coefficient ($\Delta C_{p,\mathrm{u}} = C_{p,\mathrm{u}} - C_{p,\mathrm{u}_o}$, where C_{p,u_o} corresponds to the pressure coefficient of the baseline flow) at $x/c = [0.09, 0.17, 0.27, 0.37]$ on the suction surface for control at $F^+ = 1$ and increasing C_B. The results show that at the more upstream locations, $x/c = 0.09$ and 0.17, the lift coefficient follows a trend that is approximately linear with $C_{p,\mathrm{u}}$ as C_B increases. Included in the figure is a linear fit to the $x/c = 0.09$ data using a fit that obeys the constraint $\Delta C_L = 0$ when $\Delta C_{p,\mathrm{u}} = 0$. Good agreement to the data is observed for $\Delta C_L = -0.33\Delta C_{p,\mathrm{u}}$. Once C_L saturates and changes only by relatively small amounts, $C_{p,\mathrm{u}}$ becomes approximately constant, which is reflected by the cluster of points at the end of the curves shown in Figure A.1(a). At $x/c = 0.27$, the change in $C_{p,\mathrm{u}}$ is small and shows no useful relationship to C_L. This effect is exacerbated at $x/c = 0.37$, where $C_{p,\mathrm{u}}$ is effectively constant despite the changes to the flow due to the forcing. The change in $C_{p,\mathrm{u}}$ at $x/c = 0.09$ is compared directly to the change in C_L in Figure A.1(b). The results demonstrate that the trend in static pressure on the suction surface matches very closely with the trend in C_L, with some departure occurring post-saturation. This follows from the fact that $x/c = 0.09$ is very near the suction peak in C_p (see Figure 5.5), which has a dominant effect on C_L due to the pressure difference between the upper and lower surfaces being largest in

the chordwise region near the suction peak. A linear relationship between $C_{p,\mathrm{u}}$ near the leading edge and C_L is very useful in terms of experimental practicality, as it allows C_p at a single location to act as a surrogate measurement of the section lift coefficient. Rather than measuring the unsteady pressure over the entire surface and integrating to obtain C_L, which would require an array of sensors, a single sensor can be used to estimate the changes in C_L due to control for use in a closed-loop strategy.

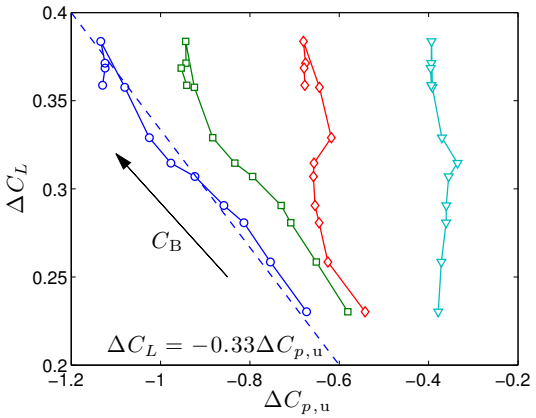

(a) ΔC_L as a function of $\Delta C_{p,\mathrm{u}}$ at various x/c locations with increasing C_B. ($\circ$) $x/c = 0.09$, ($\square$) $x/c = 0.17$, ($\diamond$) $x/c = 0.27$, ($\triangledown$) $x/c = 0.37$. Dashed line is a linear fit to the $x/c = 0.09$ data.

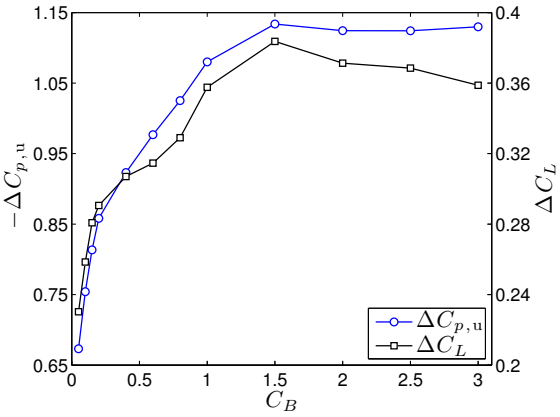

(b) Change in $C_{p,\mathrm{u}}$ at $x/c = 0.09$ compared to the change in C_L with increasing C_B.

Figure A.1: Evaluation of the use of C_p at a single location on the suction surface to estimate C_L. Open-loop control results at $F^+ = 1$ and $x_\mathrm{j}^* = -1.3\%$ are presented.

Accurate measurement of unsteady surface pressure is made difficult by two factors: hydrodynamic fluctuations that are low in both frequency and amplitude, and the available measurement devices. Since the magnitude of the pressure fluctuations on the suction surface is not known *a priori*, results from a similar experiment at $Re_c = 100,000$ on a NACA 0018 airfoil by Boutilier and Yarusevych [13] were used as reference. The authors employed an array of microphones to measure pressure fluctuations along the airfoil chord, the RMS magnitudes of which are given for $\alpha = 10°$ and $15°$ in Figure A.2. The former angle-of-attack corresponds to a LSB over a portion of the suction surface, while the latter corresponds to stalled flow. When the flow is stalled, p'_rms/q_∞ is less than 0.05, and a peak of $p'_\mathrm{rms}/q_\infty = 0.2$ occurs in the separation bubble at $\alpha = 10°$. The dimensional range of p'_rms for $q_\infty = 16$ Pa (i.e., the freestream dynamic pressure for the present experiments) is less than 3.2 Pa, with the majority of the pressure fluctuations for each case being less than 1 Pa RMS. Once control is applied and the flow is fully attached (and possibly unsteady if forcing at $F^+ \approx 1$), larger magnitude fluctuations are

expected. However, the ability to accurately resolve the pressure fluctuations of the baseline flow above the noise floor of the sensor is also necessary. The second issue inherent to the flow is that the lower limit of characteristic frequencies associated with the flow, $f_w^+ = 1$, which also corresponds to a useful control frequency $F^+ = 1$, is at a relatively low frequency of 17 Hz. Therefore, an appropriate sensor must be able to measure relatively slow pressure fluctuations.

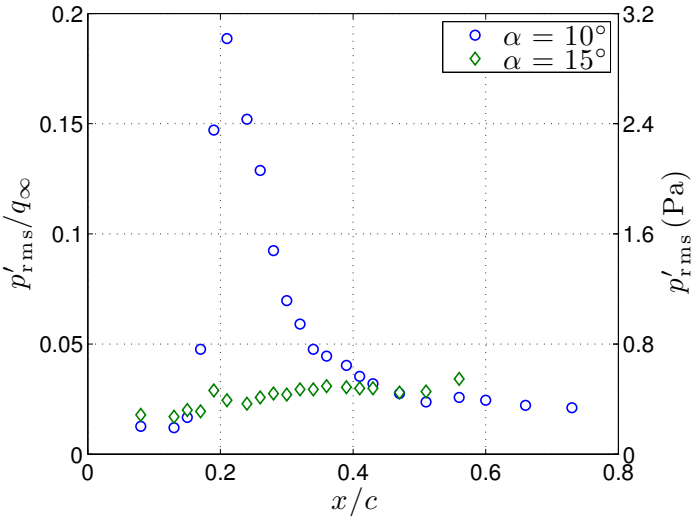

Figure A.2: RMS surface pressure distribution on a NACA 0018 airfoil at $Re_c = 100,000$, data adapted from Boutilier and Yarusevych [13]. A LSB is present at $\alpha = 10°$ and the flow is stalled at $\alpha = 15°$ The vertical scale on the right uses $q_\infty = 16$ Pa, which corresponds to the current experiments.

The difficulty arises when a sensor must be selected to measure unsteady surface pressure under these conditions. Microphones are an obvious choice for measuring pressure fluctuations, however they do not measure the DC pressure and small electret microphones that could be implemented inside a model are not intended for low frequency measurements. As such, their magnitude response decreases sharply at low frequency, typically in the range < 50 Hz. Dynamic pressure transducers are ideal as they have a frequency response that is flat from DC up to typically $\mathcal{O}(10)$ kHz, however commercially available devices (e.g., *Kulite*) do not provide sufficient signal-to-noise for such low amplitude pressure fluctuations. The full scale range of such sensors is typically too large even for the measurement of the mean pressure. For example, consider the *Kulite* model CCQ-062, for which the lowest available full-scale range is 34.5 kPa. The accuracy of this sensor is $\pm 0.5\%$ of full-scale, which is equivalent to ± 172 Pa. Thus, the range $-1.5 \leq C_p \leq 1$ on the airfoil surface results in pressures well below the static accuracy of

the sensor. Although the noise level is not provided, an input of 1 Pa RMS to the sensor would result in an output of only 3 μV RMS. Achieving a reasonable signal-to-noise ratio for the current application is therefore highly unlikely. Fuertes et al. [34] suggested a method that combines a microphone and a conventional differential pressure transducer (DPT) to measure the fluctuating and mean components of pressure, respectively. A pressure tap at the surface is connected to the DPT by a long length of tubing, and near the surface a microphone is connected to the tubing using a T-junction. This technique requires stationarity of the measured signal and dynamic calibration to account for both the microphones low frequency response and its position within the tubing. An alternative to this method is to only use a DPT for unsteady pressure measurement. These sensors have the advantage of being readily available with full-scale ranges suitable for low speed wind tunnel experiments. Such sensors are intended for the measurement of mean differential pressures, and as such generally have unknown dynamic characteristics. In addition to this, the geometry of the sensor itself and the tubing that is required for connection to the surface distorts pressure fluctuations, as described by Bergh and Tijdeman [8]. Dynamic calibration is therefore required to determine the frequency response of the DPT/tubing system. The experimentally measured transfer function or an analytically fit transfer function could be used to correct measured pressure signals [52; 69; 79], however this is not applicable in the context of closed-loop control since a significant delay would be introduced. An alternative is to optimize the tubing geometry [46] to produce a response that is flat from DC up to the largest frequency deemed necessary so that minimal signal correction is required.

A.2 Dynamic calibration

The most common types of equipment used for dynamic calibration of pressure transducers are aperiodic devices; shock tubes and fast opening pressure chambers. These comparative calibration devices expose the transducer and a reference sensor to a pressure step function. While these devices are suitable for a wide range of frequencies, they typically operate with large static pressures and large pressure step amplitudes (on the order of kPa to MPa) [21; 79]. More appropriate for the calibration of low-range DPTs is a periodic device where either the volume or the mass inside a cavity is varied with time, thereby creating pressure fluctuations. Pressure fluctuations are typically created using an audio speaker to form one wall of a sealed cavity, which creates volume and pressure fluctuations inside the cavity. The devised calibration apparatus operates on the same principal, however a piezoelectric disk is used rather than a speaker. A piezoelectric disk

may avoid some of the issues inherent to a loudspeaker, such as a natural frequency at relatively low frequency, and a decrease in gain at frequencies below this. It is expected that a piezoelectric diaphragm can more reliably create the necessary low amplitude pressure fluctuations over the entire frequency range of interest, where frequencies near $f_w = 17$ Hz and $f_{sl} = 170 - 450$ Hz are particularly important.

The dynamic calibration apparatus is shown in Figure A.3. Pressure fluctuations are created in a small cylindrical cavity with 30 mm diameter and 3.5 mm height by a piezoelectric disk that is clamped around its edge and forms one wall of the cavity. The piezoelectic disk has a natural frequency of approximately 2500 Hz. Input signals to the piezo disk were created using the same equipment described in Section 2.5. Pressure inside the cavity is measured both by the DPT to be calibrated and a *GRAS* 40BP 1/4" externally polarized pressure microphone with rear venting. This microphone, which served as the reference, has a sensitivity of 1.6 mV/Pa and a flat response within ±1 dB over 10 Hz – 25 kHz. The microphone was connected to the cavity with its diaphragm flush with the cavity wall (the protective grid was removed) using a sealed fitting. The rear vent port was exposed to atmosphere.

An *All Sensors* 1 INCH-D-4V differential pressure transducer with ±249 Pa range was selected as an appropriate sensor for use in the wind tunnel experiments. This DPT was selected to due its small size (approximately $12 \times 20 \times 30$ mm^3) and suitable full-scale range. The sensor is small enough that it can be easily installed inside the airfoil model, thereby allowing minimization of the tubing length required for connection to a surface pressure tap. In the calibration setup, the pressure tap geometry was equivalent to that of the airfoil model (0.5 mm diameter, 2 mm long). The manufacturer supplied static calibration of the DPT was verified by measuring q_∞ in the wind tunnel and the *MKS* transducer with 0.3% of-reading accuracy (see Section 2.5) served as reference.

The input signal used to drive the piezo disk was a logarithmic sweep over $f = 10 - 2000$ Hz. The lower frequency limit represents the limit of the reference microphone. The upper limit was set at $f = 2000$ Hz, corresponding to an acoustic wavelength of 170 mm, which is an order of magnitude larger than the largest linear dimension of the cavity. Therefore, it was assumed that the pressure at the tap and microphone diaphragm was equal over the swept frequency range. The input signal from the function generator, microphone output, and DPT output were sampled simultaneously at 5 kHz. An example for a typical calibration is shown in Figure A.4, where p_c and p_r are the fluctuating pressure signals of the DPT being calibrated the reference microphone, respectively. The pressure fluctuation magnitude inside the cavity was $p_{r,rms} \approx 50$ Pa, which was the nominal fluctuation level used for all calibrations. The use of the logarithmic frequency

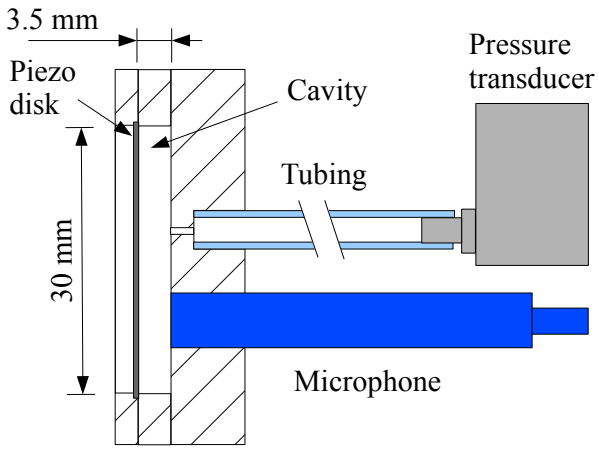

Figure A.3: Cross-sectional schematic of the dynamic pressure calibration apparatus.

sweeps allows better visual interpretation of the results using the time series in the low frequency range.

The length of the calibration sample was selected such that $N_r = 100$ independent non-overlapping records (equivalent to the number of sweeps) each containing 2^{13} data points were acquired, giving a spectral resolution of 0.6 Hz. Spectra and cross-spectra of the signals were computed using a Hamming window and 50% overlap between records. The frequency response (or transfer function) of the DPT was computed from the pressure spectra as:

$$H = \frac{P_{p_c p_r}}{P_{p_c p_c}}, \tag{A.1}$$

where $P_{p_c p_r}$ is the cross-spectral density of the two signals. The gain and phase of the response are given by $|H|$ and $\angle H$, respectively. In this case, $|H| = 1$ corresponds to the DPT sensitivity being equivalent to the DC sensitivity obtained from the static calibration (0.8 mV/Pa). An initial frequency response for the *All Sensors* DPT with a 25 mm length of 1.6 mm inner diameter (ID) tubing is shown in Figure A.5. The calibration apparatus produces a smooth frequency response that primarily shows the expected behaviour for this system; a resonant peak associated with the tubing/transducer geometry followed by the attenuation of fluctuations at larger frequencies. However, an unexpected rise in both gain and phase is observed at low frequency. Since the flat portion of the gain response between approximately $30 \leq f \leq 200$ Hz is at $|H| = 1$, the rise in gain below 30 Hz suggests there is a second resonant peak at some very low frequency < 10 Hz, since $|H|$ must return to 1 at DC. An amplification at such low frequency in addition to the resonant peak at 675 Hz is not expected based on models of the tubing/transducer

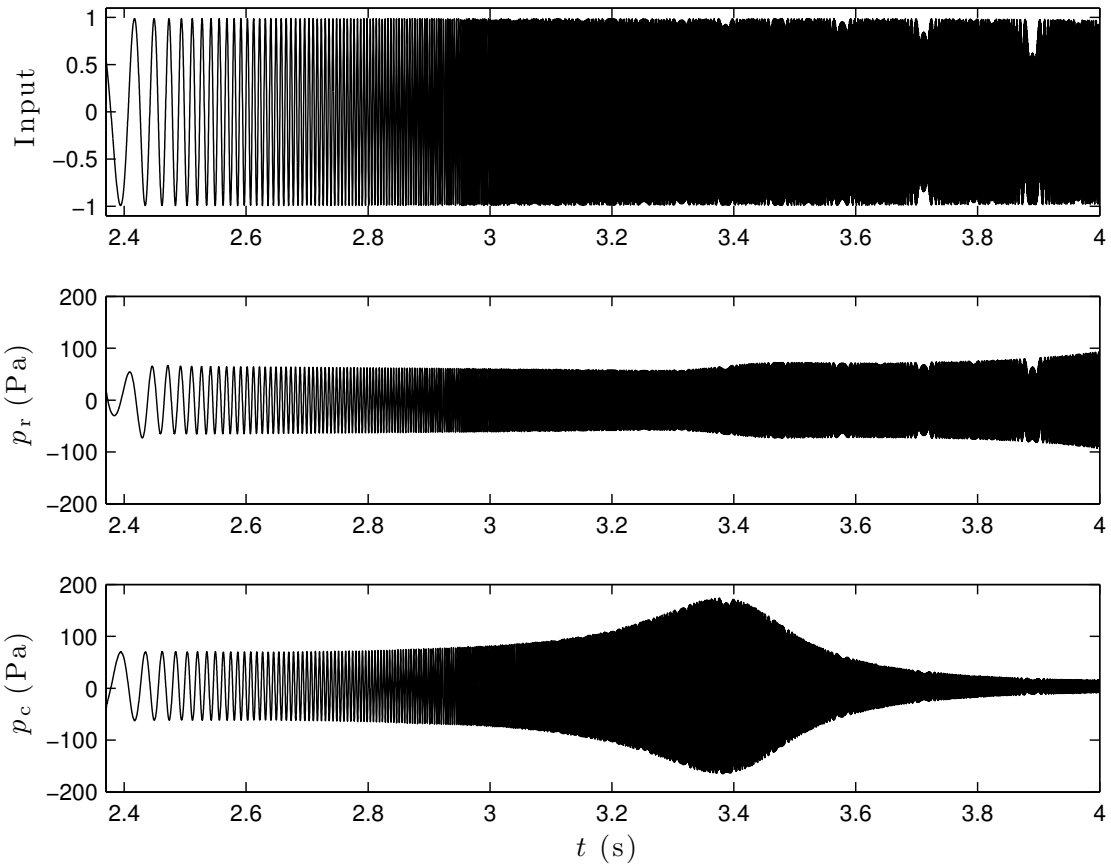

Figure A.4: Time-series segments from a typical dynamic calibration showing one frequency sweep.

system [8]. Figure A.6 shows the power spectra of the microphone and DPT signals over the calibration range $10 \leq f \leq 2000$ Hz. Over the majority of this frequency range, the power spectrum of the microphone is relatively flat and indicates that the fluctuating pressure amplitude does not vary considerably. A sharp decrease in the microphone power spectrum is observed below approximately 20 Hz, where it falls below that of the DPT. This suggests that either these low frequency fluctuations are being correctly measured by the microphone and amplified by the DPT, or measured correctly by the DPT and attenuated by the microphone. The time series in Figure A.4 show that p_c is approximately constant in amplitude at the beginning of the frequency sweep, while p_r shows a decrease in amplitude. Although frequencies down to 10 Hz are within the ± 1 dB range of the microphones frequency response, the issue is likely due to pressure fluctuations transmitted to the rear of the microphone diaphragm through the vent port. The air resistance within the small vent port is sufficient to prevent acoustic waves from entering

the microphone cavity for most frequencies, however it is likely that low frequency waves emanating from the vibrating piezo disk are acting on the rear of the diaphragm.

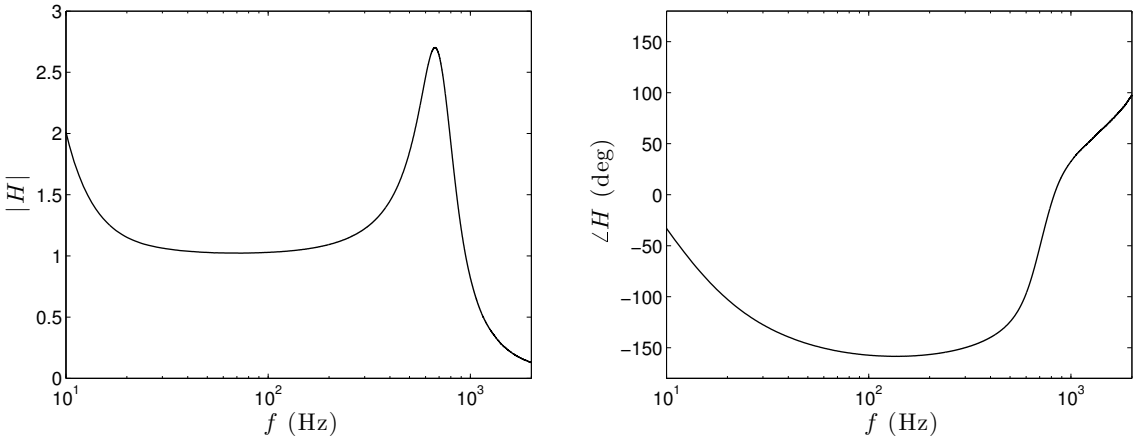

Figure A.5: Typical dynamic calibration with a 25 mm length of 1.6 mm ID tubing used as connection to the pressure tap.

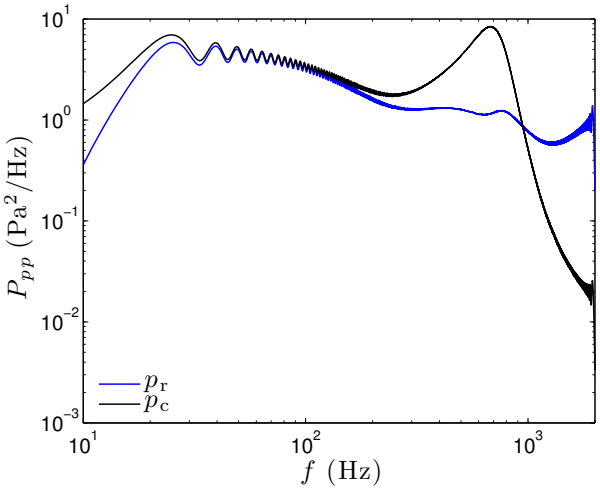

Figure A.6: Power spectra of the microphone and DPT signals corresponding to the frequency response shown in Figure A.5.

Additional evidence for this distortion of the microphone signal can be gained from a measurement of the pressure tap/tubing system frequency response. In this measurement, the DPT at the end of the tubing was replaced with a second microphone identical to the reference microphone. This measurement was done to confirm that the peak at 675 Hz corresponds to resonance caused by the tubing. The frequency response gain and

power spectra of the signals are shown in Figure A.7 (note that the sweep was only performed up to 1000 Hz in this case). In this case, the gain is flat below the resonant peak due to the power spectra of the two microphones being equivalent in this range. This confirms that the peak at 675 Hz is due to tubing resonance, and also shows that both microphones are affected in the same way at low frequency. A number of additional tests were performed in an attempt to conclusively prove that this behaviour was due to low frequency waves affecting the rear side of the microphone diaphragm, including isolating the rear side of the piezo disk in a large, sealed PVC tube. However, this yielded the same results. Another possible cause is vibration of the microphone, since it is rigidly connected to the apparatus with the vibrating piezo, but this could not be tested in a meaningful manner. Based on existing knowledge in the literature of the frequency response for a tubing/DPT system that is expected and has been shown experimentally, it was concluded that the issue must be related to the reference microphone. As such, subsequently shown frequency responses have been corrected to be flat in the range below resonance.

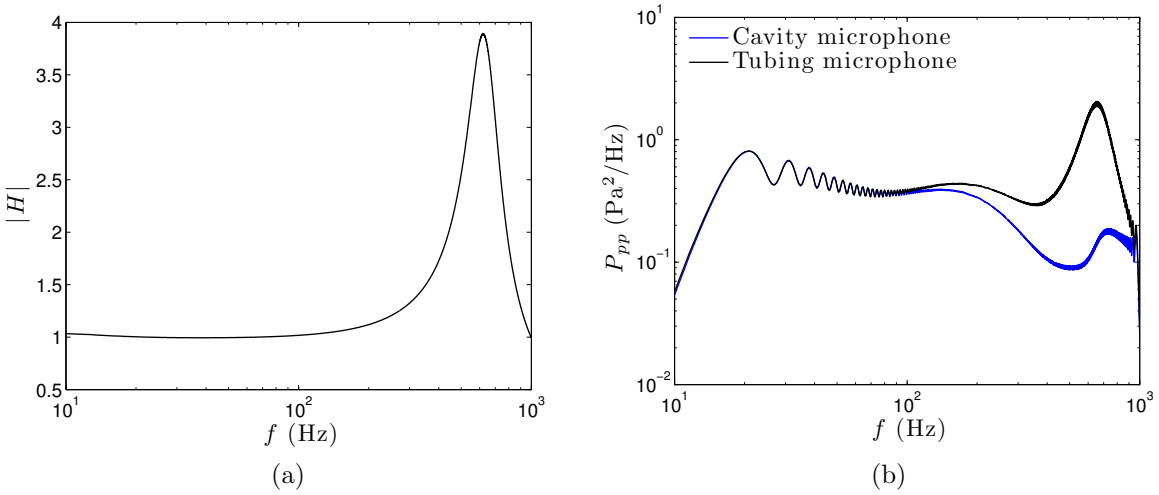

Figure A.7: (a) Gain response of the tubing using a second identical microphone in place of the DPT. (b) Power spectra of the microphone signals.

The quality of the calibration can be assessed by several metrics: the signal-to-noise ratio, S/N, of each signal, and the coherence between the two signals. For the signal-to-noise ratio, noise signals were measured in a quiet environment with no excitation of the piezoelectric disk. Figure A.8(a) shows S/N of each signal for the same calibration in Figure A.5. The results demonstrate that S/N for the microphone and DPT are at least 40 dB and 30 dB, respectively, and thus each sensor is measuring well above its noise

floor. The coherence, defined as

$$\gamma_{p_c p_r} = \frac{|P_{p_c p_r}|^2}{P_{p_c p_c} P_{p_r p_r}}, \tag{A.2}$$

demonstrates the linear relationship between the pressure measured by the microphone and the DPT, where unity coherence indicates a perfect linear relationship. The coherence is an important indicator of calibration quality since the random error in the frequency response is a function of $\gamma_{p_c p_r}$ [6], *viz.*

$$\epsilon = \sqrt{\frac{1 - \gamma_{p_1 p_2}}{2\gamma_{p_1 p_2} N_r}}, \tag{A.3}$$

where ϵ is the relative error in gain and also the absolute standard deviation in phase given in radians. Therefore, the random error in the frequency response will be small even with few records for ensemble averaging for a calibration with $\gamma_{p_c p_r}(f) \approx 1$. Equation (A.3) is defined for spectra computed using rectangular, non-overlapping windows and serves only as an approximation of the random error for the present methodology (i.e., Hamming windows with 50% overlap). As shown in Figure A.8(b), the coherence is 1 over most of the frequency range with a minimum value of $\gamma_{p_c p_r} = 0.987$. From equation (A.3), the random errors in gain and phase are less than 1% and 1°, respectively, over $10 \leq f \leq 2000$ Hz. It is of particular importance that despite the issue associated with the reference microphone at frequencies below ~ 30 Hz, accurate calibration at low frequency is possible with this apparatus. Calibration with low error is achieved even in the frequency range above 1000 Hz where the pressure signal measured by the DPT is strongly attenuated. It is important to note that this is not only due to the calibration apparatus, but is also a result of a sufficient S/N in both the DPT being calibrated and the reference microphone.

The goal of the unsteady pressure measurement system was to achieve a flat frequency response from DC up to the largest frequency possible, and at least 300 Hz, such that there would be no need for signal correction in post-processing. For a given DPT, the resonant peak can be altered in both frequency and magnitude by changing the geometry of the tubing of the pressure tap. In general, theory dictates that when the length-to-diameter ratio of the tubing is large, decreasing tubing length of increasing tubing diameter have a similar effect of increasing the resonant frequency [8]. Physical constraints within the airfoil model limited the minimum tubing length to 25 mm, thus the assumption of a very large length-to-diameter ratio was not valid for feasible tubing diameters. To determine the effect of tubing diameter on the frequency response for a fixed length of 25 mm, three

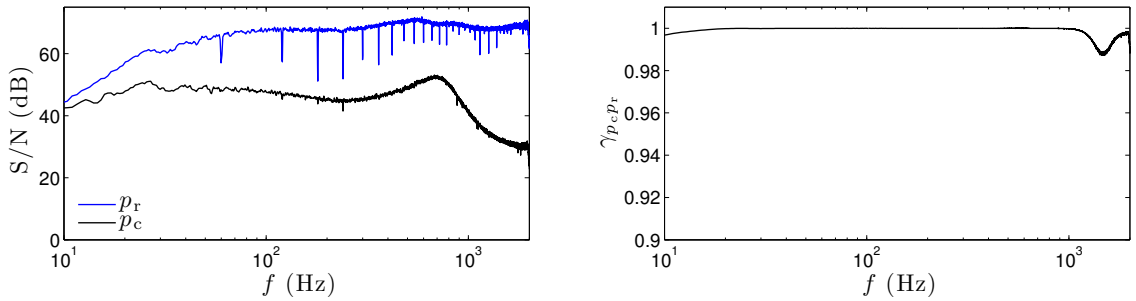

Figure A.8: Signal-to-noise and spectral coherence for the same calibration as Figure A.5.

different tubing IDs were compared: 0.8 mm, 1.6 mm and 3.2 mm. The gain portion of the frequency responses shown in Figure A.9 demonstrate that even for length-to-diameter ratios from approximately 31 to 8, the resonant peak increases both in frequency and magnitude with increasing ID. Within 10%, the gain can be considered flat up to 180 Hz, 235 Hz and 310 Hz for 0.8 mm, 1.6 mm and 3.2 mm ID, respectively. Therefore, the 3.2 mm ID tubing was selected. This was the largest diameter tested, as a larger diameter would present practical issues for the tubing connection in the airfoil model.

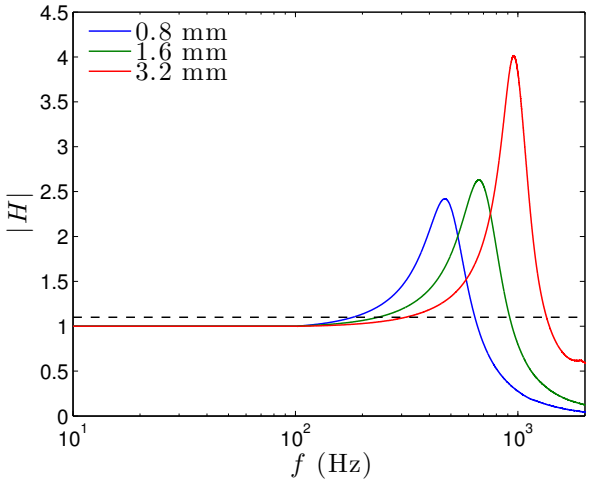

Figure A.9: Gain responses for a 25 mm tube length and varying inner diameter. The dashed line indicates $|H| = 1.1$.

A.3 Wind tunnel measurements

The dynamic calibration discussed in the previous section was used to determine the frequency response of the tubing/DPT system, and select tubing geometry to produce an acceptable response. An issue that remains for the use of such a sensor in a closed-loop control system is the large resonant peak at 955 Hz. Because of this resonance, pressure fluctuations in the bandwidth $300 \leq f \leq 1300$ Hz will be substantially amplified. This is particularly problematic since the carrier frequency of the synthetic jet is at 1000 Hz, thus there will be non-negligible energy content near this frequency. A low-pass filter is desired to suppress this resonant peak so that the measured signal is not dominated by fluctuations at $f \approx 1000$ Hz. A simple first-order resistor-capacitor filter provides high-frequency attenuation at -20 dB/decade, which was found to be insufficient in suppressing the peak, therefore a second-order Butterworth filter with a -40 dB/decade attenuation was designed. Figure A.10 compares the unaltered frequency response to the filtered response using a Butterworth filter with a cut-off frequency of 450 Hz. As indicated by the dashed lines, the peak is attenuated and the filtered response gain varies primarily within ±10% of the DC value up to 1000 Hz. The filter also provides a DC gain of approximately 1.6. Although this filter causes non-linear phase variations over a larger bandwidth than the raw signal, the greater concern in the context of real-time control is a flat gain response and attenuation of the resonant peak.

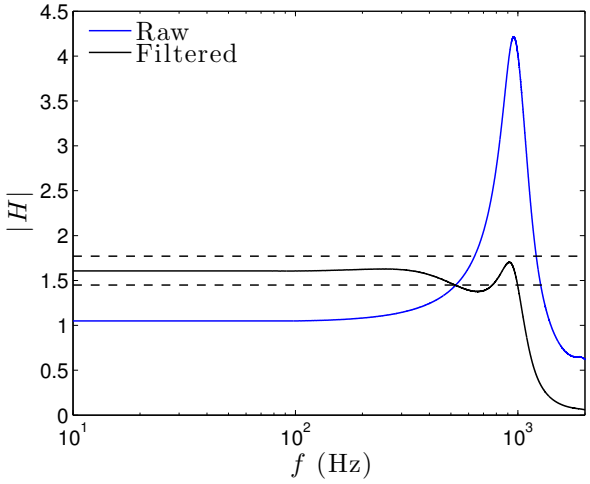

Figure A.10: Comparison of the DPT gain response with and without low-pass filtering. The dashed lines indicate ±10% of the filtered DC gain, $|H| = 1.6$.

Two of the *All Sensors* DPTs were installed inside the airfoil model: one at $x/c = 0.09$ to track changes in C_L (as discussed in Section A.1), and a second positioned at

a downstream location to capture the dynamics of the controlled flow. An appropriate chord location for this second sensor would be one that experiences coherent surface pressure fluctuations of substantial magnitude. In order to estimate the variation in pressure fluctuation magnitude along the chord, it was assumed that surface pressure fluctuations are related to vorticity fluctuations. The phase-averaged vorticity was used to define a 'swirl strength' parameter, *viz.*

$$\langle S \rangle = \frac{c}{U_\infty} \int_0^\infty |\langle \omega \rangle| \, \mathrm{d}(y/c), \tag{A.4}$$

which quantifies the magnitude of coherent vorticity fluctuations along a line perpendicular to the surface. The RMS magnitude of this quantity is shown in Figure A.11 for $F^+ = 1$ and two values of C_B. The swirl strength at $F^+ = 1$ is considered since the controlled flow is dominated by large scale unsteadiness when forcing near f_w^+, unlike forcing in the range of f_sl^+ at $F^+ = 14$ (Section 5.3). At each blowing ratio, but particularly for $C_\mathrm{B} = 0.1$, there are minima present in $\langle S \rangle_\mathrm{rms}$. Since a smooth trend should be expected, these sharp decreases in $\langle S \rangle_\mathrm{rms}$ are likely the result of limited phase resolution. Considering the phase-locked velocity field was only measured every 45° and the vortices at $F^+ = 1$ and $C_\mathrm{B} = 0.1$ travel from their inception point to the trailing edge over 270°, there are x/c locations where the passage of the vortex core was not captured. Thus, $\langle \omega \rangle$ and subsequently, $\langle S \rangle$, are underestimated at certain locations. This effect is not as severe at $C_\mathrm{B} = 1$ where the vortex convection speed is slower. To observe the general trend in $\langle S \rangle_\mathrm{rms}$, a third-order polynomial was fit to the data excluding points near the minima. The results demonstrate an increase in $\langle S \rangle_\mathrm{rms}$ up to approximately $x/c = 0.5$, followed by what is likely a plateau. Based on this analysis and physical constraints, the chord location of the second pressure sensor was selected as $x/c = 0.55$.

Figure A.12(a) shows pressure spectra from the sensors at $x/c = 0.09$ and 0.55 for the baseline flow at $\alpha = 12°$ and $Re_c = 100,000$. Also included in Figure A.12(b) are velocity spectra in the boundary layer at similar chord locations, $x/c = 0.1$ and 0.55. Compared with the velocity spectra, the pressure spectra show the expected shapes corresponding to laminar flow at $x/c = 0.09$ and turbulent flow at $x/c = 0.55$. The low frequency range prior to decay that contains the majority of the signal energy is several decades above the sensor noise floor ($\sim 7 \times 10^{-5}$ Pa^2/Hz) at each location. However, several low frequency peaks at 8.5 Hz and 15 Hz are present in the pressure spectra that do not appear in the velocity spectra (as discussed in Section 3.4, the peaks at 12 Hz and 46 Hz in $P_{u_\mathrm{t}u_\mathrm{t}}$ are due to traverse vibration). These peaks are observed in the velocity noise floor spectrum, which was measured at the centerline of the test section with no model in the tunnel at $U_\infty = 5$ m/s. The fact that the peaks are observed in the pressure spectra

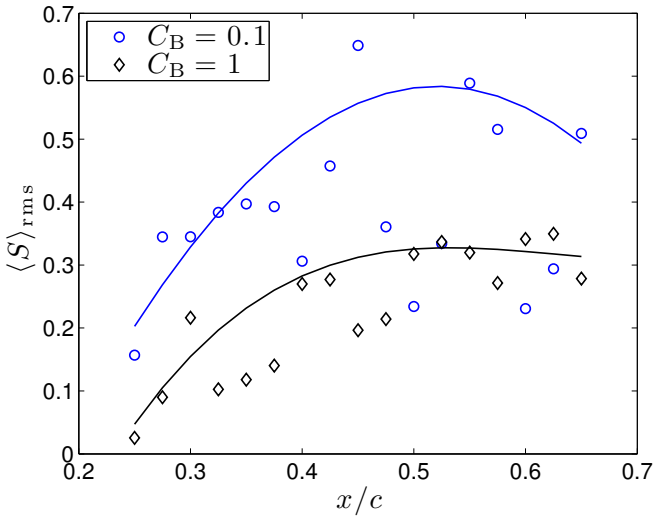

Figure A.11: Swirl strength RMS magnitude variation along the airfoil chord with forcing at $F^+ = 1$ and $x_j^* = -1.3\%$. The lines show third-order polynomial fits to the data.

and the background velocity spectrum suggests that they are not physical to the flow over the airfoil, but rather are due to acoustic background noise. This conclusion was further supported by pressure spectra measured at different Reynolds number, which also showed peaks at 8.5 Hz and 15 Hz. Known sources of acoustic resonance in closed-loop wind tunnels are longitudinal, or 'organ-pipe', modes related to the length of the tunnel circuit. Given a speed of sound in air of 340 m/s, the frequency corresponding to a wavelength equivalent to the tunnel circuit length, approximately 45 m, is 7.6 Hz. The proximity of this frequency to 8.5 Hz gave additional confidence in concluding that the peaks at 8.5 Hz and 15 Hz were due to longitudinal modes related to the tunnel length, and half-length.

Acoustic resonance of the tunnel is generally undesirable, but it is particularly problematic in the context of experiments at $Re_c = 100,00$, as $f^+ = 1$ corresponds to 17 Hz. This places the resonant modes in close proximity to frequencies of importance, and the ideal course of action would be to eliminate the resonant behaviour. A feature common to many closed-loop tunnels is ventilation slots at the downstream end of the test section, or beginning of the diffuser, to establish atmospheric pressure in the test section. This feature was not present on this wind tunnel, thus it was surmised that adding these slots may disrupt longitudinal pressure waves and eliminate resonance. The baseline pressure spectra after ventilation slots were added at the diffuser entrance are shown in Figure A.13(a). The lower resonant mode at 8.5 Hz ($f^+ = 0.49$) was eliminated, however the resonant mode associated with the tunnel half-length at 15 Hz ($f^+ = 0.85$)

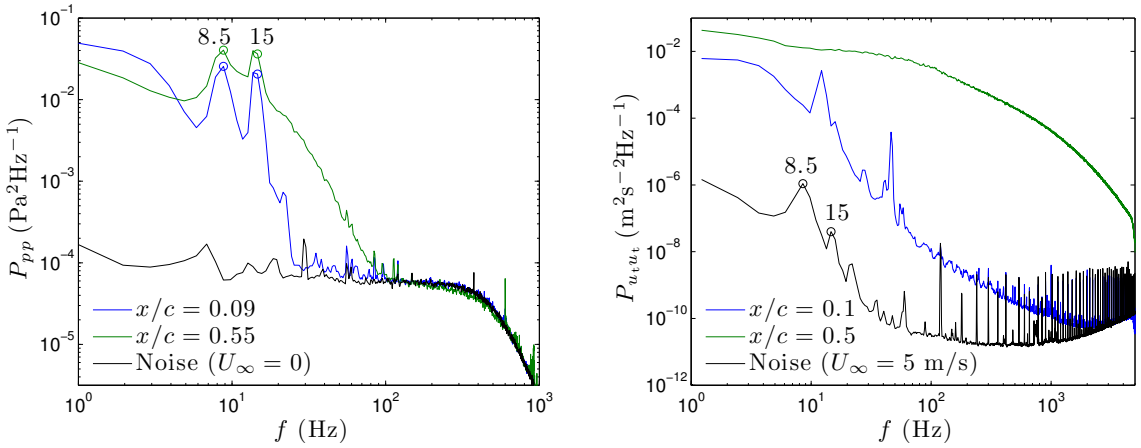

(a) Surface pressure spectra.

(b) Boundary layer velocity spectra.

Figure A.12: Pressure and velocity spectra at/near $x/c = 0.1$ and 0.5 for the baseline flow. The pressure noise floor represents the noise floor of the sensors themselves, while the velocity noise floor is that of the wind tunnel at $U_\infty = 5$ m/s (equivalent to $Re_c = 100,000$).

was unaffected. This resonant mode is likely associated with acoustic reflections from the turning vanes at the tunnel corners immediately upstream and downstream of the test section. Unfortunately, eliminating this source of acoustic resonance would be difficult and likely require substantial tunnel modifications. The issue with this resonant mode is demonstrated in Figure A.13(b), which shows pressure spectra for control at $F^+ = 1$ and $C_B = 1$. The $f^+ = 0.85$ peak is in close proximity to the peak at $f^+ = 1$ due to forcing in each spectra, and dominates over this peak at $x/c = 0.09$. The spectra also demonstrate that the frequency content near $f^+ = 58$, the forcing signal carrier frequency, is large relative to the $f^+ = \mathcal{O}(1)$ peak and the broadband spectrum level. As shown by the velocity spectra in Figures 5.23(a) and 5.24(a), there are hydrodynamic fluctuations at the carrier frequency, but the energy near $f^+ = 58$ is not dominant. The difference in the pressure spectra is likely due to the contribution of acoustic noise at the carrier frequency, as the synthetic jet is loud during operation. If these high frequency fluctuations prove problematic for closed-loop control purposes, an additional low-pass filter with a higher cut-off frequency could be implemented.

Mitigating the peak at 15 Hz presents a greater challenge since it is within the frequency range of interest. A technique that is well suited for this application is optimal least-squares filtering. As described by Naguib et al. [61], this technique can be used to correct time series and remove facility related noise sources. The method relies of the use of a reference measurement placed in the flow some distance away from the

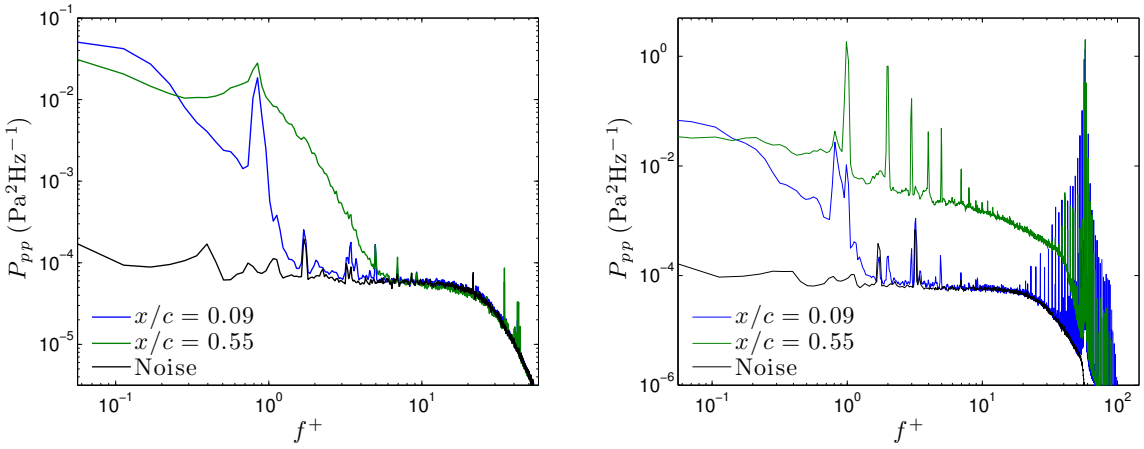

(a) Baseline

(b) $F^+ = 1$ and $C_B = 1$

Figure A.13: Pressure spectra after adding ventilation slots to the wind tunnel.

measurement location(s). Both the reference and the sensors whose signals are being corrected will measure the noise, with the influence of the noise at each location ideally being the same. Since the reference is located a significant distance away, fluctuations pertinent to the flow will not be measured. That is, the only part of the reference and measurement signals that should be correlated is the facility noise. The optimal filtering algorithm produces filter coefficients based on the cross-correlation between the reference and measurement signals, and the filter is used to extract the correlated noise signal. This technique can be implement in real-time as a finite impulse response filter. For the present experiments, this filtering technique was tested by installing one of the *GRAS* pressure microphones (described in the previous section) flush with the tunnel wall directly above the airfoil at approximately midpsan to serve as reference. Figure A.14(a) shows the pressure spectrum for the baseline flow measured by the reference microphone above 10 Hz, since this is the lower limit of the microphones ±1 dB flat response. The peak at $f^+ = 0.85$ (15 Hz) is clearly visible in the reference microphone spectrum, as well as several smaller peaks at $f^+ = 3.27$ (57 Hz) and 4.90 (85 Hz) that are also present in the pressure spectra on the airfoil surface. Using the reference signal and the signal from the sensor at $x/c = 0.09$, optimal filter coefficients were computed and the correlated noise signal was extracted (note that the results were the same if the sensor at $x/c = 0.55$ was used). The spectrum of the noise signal is also given in Figure A.14(a), which clearly shows a dominant peak at the tunnel acoustic resonance frequency. The surface pressure signals were filtered by subtracting the extracted correlated noise time series. Spectra of the filtered and uncorrected signals are shown in A.14(b). At $x/c = 0.55$, the sharp

peak at $f^+ = 0.85$ was eliminated, however their remains a relatively broad peak over approximately $0.5 < f^+ < 1$. The filter is less effective at $x/c = 0.09$, where the peak due to acoustic noise was decreased in magnitude, but not fully removed. The cause of this poor filter performance in this case is speculated to be due the shape of the power spectrum at $f^+ = 0.85$. The example of this filtering strategy by Naguib et al. [61] was for removing peaks from turbulent signals, and the artificially superimposed noise was at frequencies where the power spectrum decay rate was much lower than for the laminar spectrum at $x/c = 0.09$. For example, the noise peaks occurred in a part of the spectrum where the decay is estimated as -13 dB/decade in the work of Naguib et al., whereas the spectrum for $x/c = 0.09$ in Figure A.14(b) at $f^+ = 0.85$ decays at approximately -25 dB/decade.

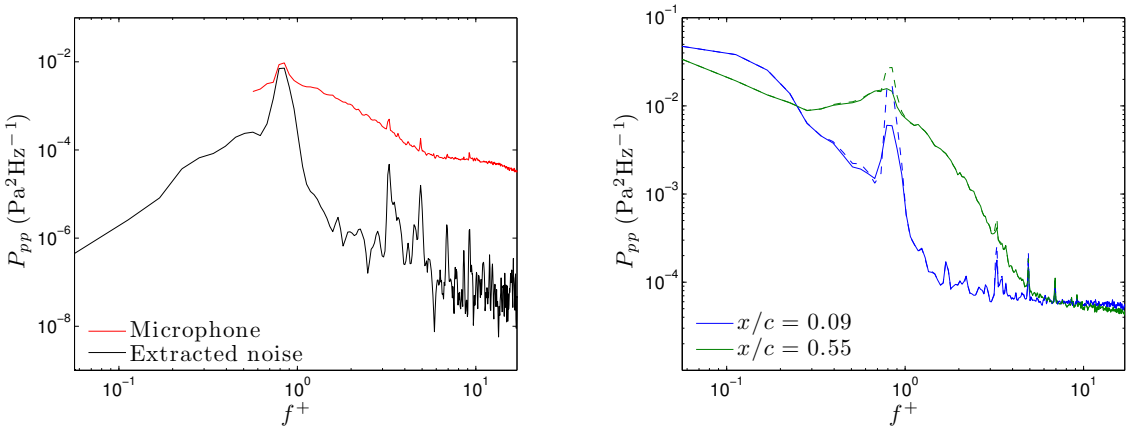

(a) Spectra of the reference microphone signal and the correlated noise extracted by the filter.

(b) Optimally filtered (solid lines) and uncorrected (dashed) surface pressure spectra.

Figure A.14: Optimal least-squares filtering of the airfoil surface pressure using a reference measurement of the test section surface pressure.

The efficacy of the filter in attenuating $f^+ = 0.85$ fluctuations in the surface pressure signals for closed-loop feedback sensing would require testing of the control system. Depending on the control algorithm, the filtered signals may allow for acceptable performance. It should also be acknowledged that the optimal least-squares filter is implemented digitally, therefore when applied in discrete time in a closed-loop system, a time delay is introduced. The time delay depends on the filter order, which in turn dictates the effectiveness of the filter. An alternative to filtering would to perform experiments at a higher Reynolds number, thereby shifting the fixed 15 Hz resonance to a lower value of f^+ further from frequencies of interest (i.e. away from $f^+ = 1$). Increasing Re_c is accompanied by a number of additional considerations, including a change in the state

of the baseline flow for fixed α, and limiting the maximum C_{B} that can be achieved with the same synthetic jet (since U_∞ increases).

A.4 Summary and recommendations

A feedback sensing strategy was developed that would be suitable for a control objective involving the maximization of C_L subject to an energy input penalty. It was shown that C_L varied linearly with the surface pressure at $x/c = 0.09$ (i.e. near the suction peak) for increasing C_{B}. This result is extremely advantageous from an experimental perspective, as it allows C_L to be estimated using a single pressure sensor. Due to experimental challenges at low Reynolds number, differential pressure transducers were selected to measure the unsteady surface pressure, which required the DPT/tubing system to be dynamically calibrated. Optimizing the tubing geometry and applying a low-pass filter led to a gain response for the DPT/tubing that was flat within approximately $\pm 10\%$ up to 1000 Hz. Implementation of these sensors at $x/c = 0.09$ and 0.55 revealed the existence of acoustic resonant modes natural to the wind tunnel. Mitigation of these peaks both by tunnel modifications and digital filtering was demonstrated, with varying degrees of effectiveness for different acoustic modes.

The development of feedback sensing for C_L meets the initially defined objective of accomplishing this initial step towards closed-loop control. This proved challenging due the low Reynolds number limiting feasible means for measuring unsteady surface pressure, and the ensuing dynamic calibration that was required to determine the frequency response of the differential pressure transducer/tubing system. Dynamic calibration of this type of low pressure sensor is not particularly common and had its own set of challenges. The intention is that the sensors with known frequency response that have been implemented in the model, and knowledge gained from the open-loop control results can be used to develop closed-loop control strategies. This topic is one with a great deal of complexity and requires its own dedicated effort.

Appendix B

Test Section Inlet Velocity Characterization

The flow uniformity over a portion the test section inlet was characterized for several freestream velocities. This type of characterization had not been done in many years, and was not documented in a way that it is readily available. The information provided here is intended to serve as a documentation of the state of the flow in the test section at the time of this thesis.

Two-component velocity measurements were performed using a cross-wire with two wire arranged at $\pm 45^\circ$ relative to the axis of the probe. The cross-wire was oriented such that the streamwise, u, and transverse, v, components of velocity were measured. In the context of these measurements, the $[x, y, z]$ coordinate system is fixed at the center of the test section inlet. Velocity was measured in the yz plane over $-250 \leq y \leq 250$ mm and $-250 \leq z \leq 250$ by traversing a single cross-wire probe in increments of $\Delta y = \Delta z = 12.5$ mm. This range was the result of several practical limitations, the primary one being measurement time. The spatial resolution over the given domain results in 1681 measurement locations and at each location, 60 second samples were acquired, giving a total time of approximately 28 hours. Long sampling time was necessary to achieve adequate convergence in RMS velocities. In addition to this, the range of motion of the traverse in the y and z directions was 500 mm. Therefore, measuring over a larger domain would require changing the setup throughout the experiment, which would add to the already substantial measurement time. The cross-wire was held approximately 1.4 m upstream of the traverse to minimize its influence at the measurement plane. The transverse linear stage, which moved in the spanwise direction during the measurements, is approximately 880 mm $\times$ 60 mm in cross section, which represents an area blockage to the test section of 5%. The blockage of the entire traverse is 12%.

The accuracy of the velocity measurements, in particular for determining the angle between U and V, relies heavily on the calibration. An *in situ* look-up table calibration approach was adopted since Burattini and Antonia [17] showed that this is more accurate than the effective angle methodology, particularly at low velocities. The cross-wire probe holder was mounted to a rotary stage that allowed the yaw angle (i.e. the angle relative to U_∞ in the xy plane) to be adjusted during calibration. Calibration was performed with the probe located at $y = 0$ and $z = 0$ over a range of yaw angles from $-6°$ to $6°$ in $2°$ increments. When the yaw angle was varied, the transverse location of the probe was adjusted to ensure it remained at $y = 0$. A static-pitot probe at $y = 0$ and a small z offset connected to the 0.3% of-reading accuracy differential pressure transducer (Section 2.5) served as a reference measurement of U_∞ for calibration, as shown in Figure B.1. Note that for these measurements, U_∞ was measured at the center of the inlet plane. At each yaw angle, the cross-wire voltages and pitot tube pressure were measured for eight discrete values of U_∞ that were above and below U_∞ for the actual measurement. This type of calibration results in a *relative* determination of the angle between U and V, $\theta = \tan^{-1}(V/U)$, since $\theta = 0°$ at $y = z = 0$ when the probe is at zero yaw angle is defined by the calibration. Due to the long measurement time, the temperature correction technique of Hultmark and Smits [49] was employed. At $U_\infty = 10$ m/s, the temperature in the test section increased by only 1.6 °C over the course of the 28 hour measurement.

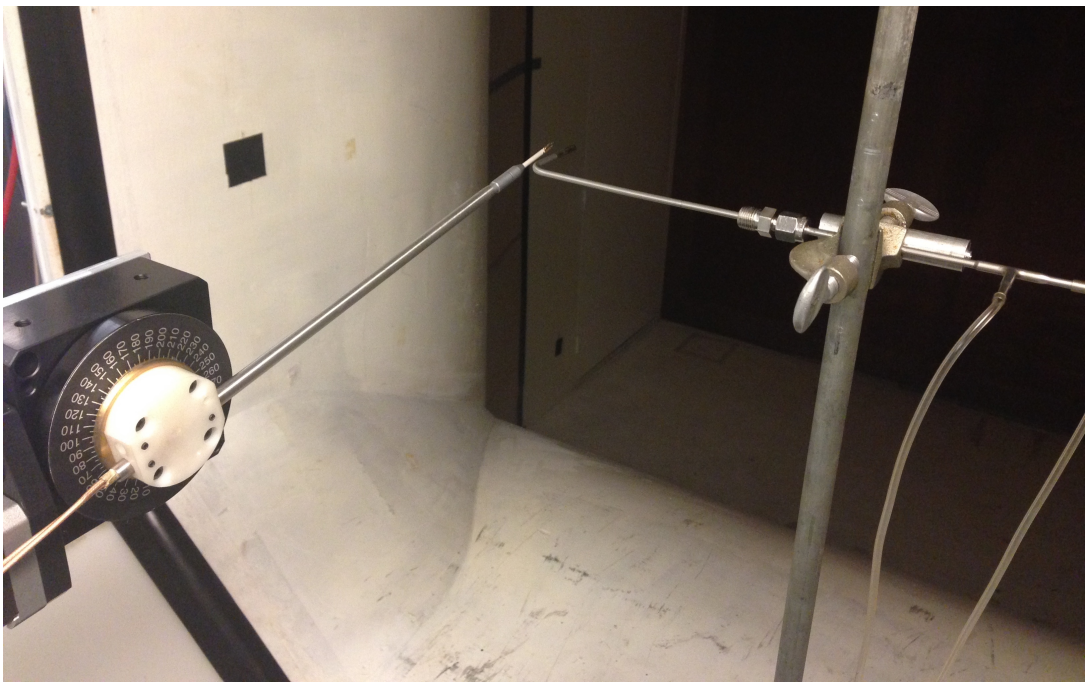

Figure B.1: Photo of the cross-wire probe during calibration.

The flow uniformity results for $U_\infty = 5$ m/s and $U_\infty = 10$ m/s are shown in Figures B.2 and B.3, respectively. The quantities shown are the relative streamwise velocity variation, $\Delta U/U_{\text{ave}} = (U - U_{\text{ave}})/U_{\text{ave}}$ where U_{ave} is the spatial average over the measurement domain, the relative mean velocity angle, $\Delta\theta = \theta - \theta(0,0)$, and the turbulence intensity, u_{rms}/U. For both values of U_∞, the results show that the variation in U is primarily within $\pm 3\%$ of the spatial average. Two regions of low velocity distributed asymmetrically about $z = 0$ are apparent, and velocity increases towards the corners on the $z = -250$ mm end of the measurement plane. The localized regions of low velocity also coincide with regions of increased turbulence intensity. At $U_\infty = 5$ m/s, u_{rms}/U varies from approximately 0.06% to 0.09%, and from 0.06% to 0.1% at $U_\infty = 10$ m/s. Figure B.2(d) also shows an example of the variation in turbulence intensity along z with error bars. The typical uncertainty in turbulence intensity is $\pm 0.005\%$ and $\pm 0.006\%$ at $U_\infty = 5$ m/s and 10 m/s, respectively. The fact that similar asymmetric patterns are evident in $\Delta U/U_{\text{ave}}$ and u_{rms}/U suggests asymmetry in the flow conditioning, possibly due to dirt accumulation on the screens. An asymmetry about the y axis is also observed in $\Delta\theta$, where $\Delta\theta$ decreases to approximately 2°–2.5° at $y = 250$ mm, but only increases to approximately 1° at $y = -250$ mm.

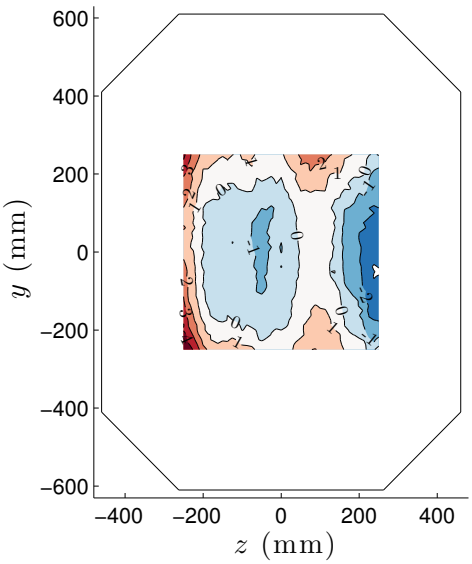

(a) $\Delta U/U_{\text{ave}}$ (%)

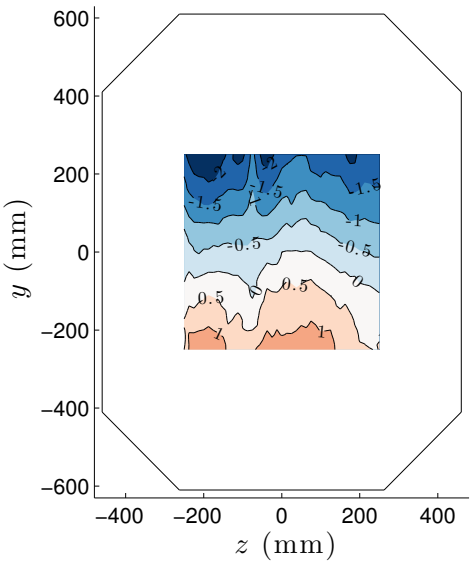

(b) $\Delta\theta$ (degrees)

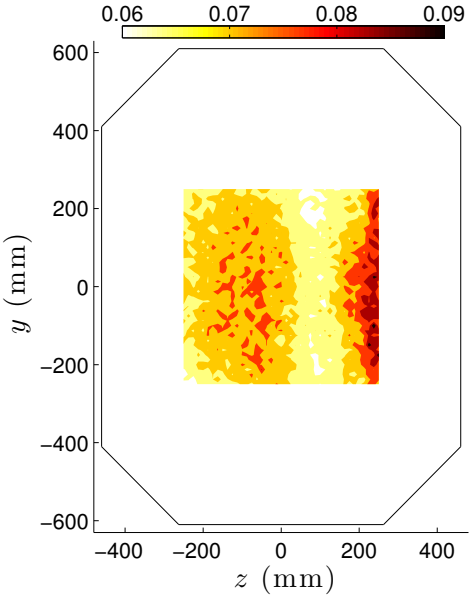

(c) Turbulence intensity (%)

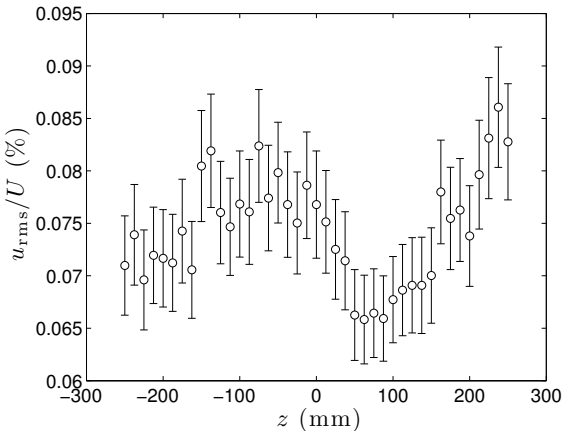

(d) Turbulence intensity at $y = 0$.

Figure B.2: Flow uniformity at the test section inlet for $U_\infty = 5$ m/s.

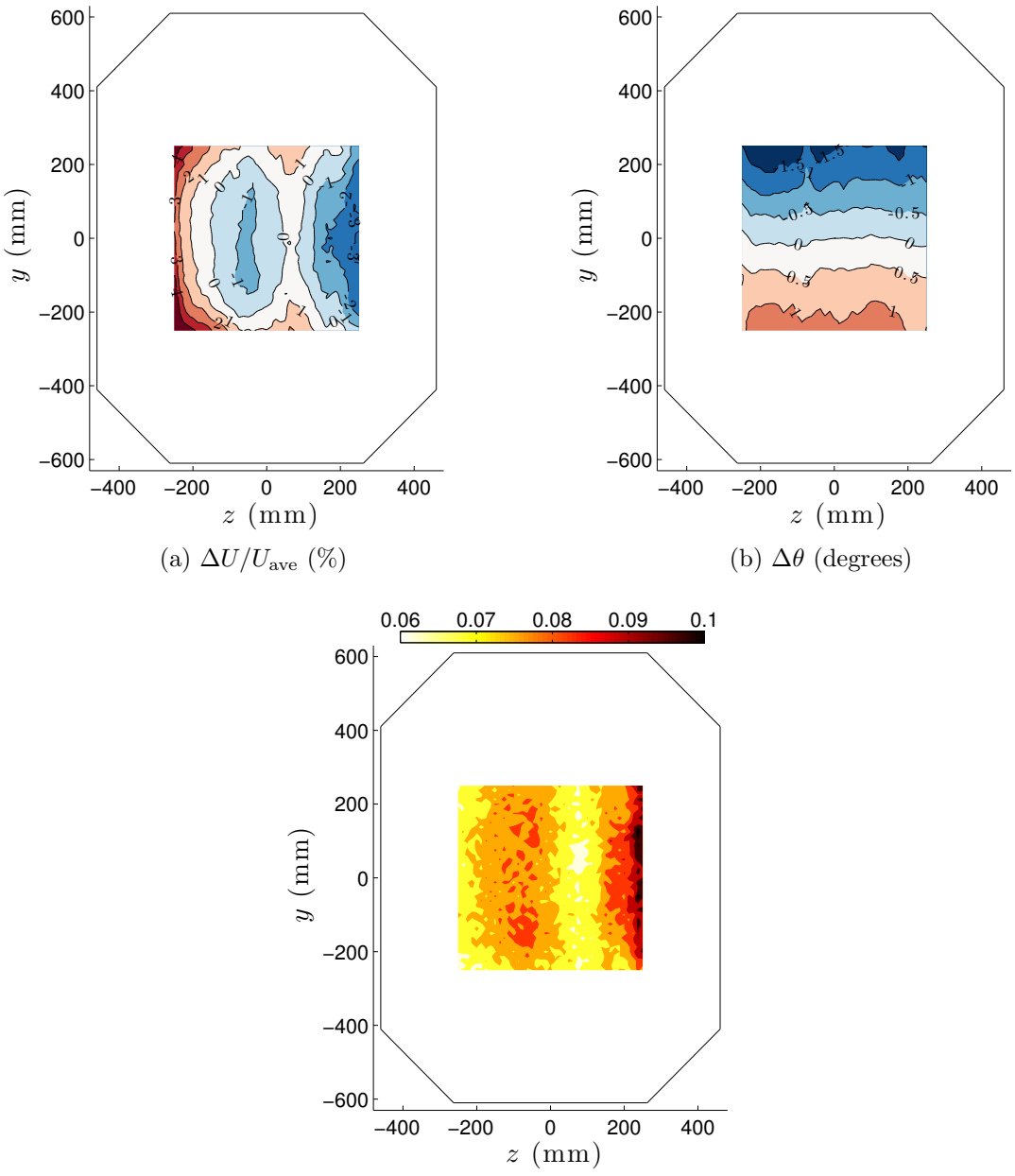

(a) $\Delta U/U_{\text{ave}}$ (%)

(b) $\Delta\theta$ (degrees)

(c) Turbulence intensity (%)

Figure B.3: Flow uniformity at the test section inlet for $U_\infty = 10$ m/s.

Bibliography

[1] Amitay, M. and A. Glezer (2002a). Controlled transients of flow reattachment over stalled airfoils. *International Journal of Heat and Fluid Flow 23*(5), 690–699.

[2] Amitay, M. and A. Glezer (2002b). Role of actuation frequency in controlled flow reattachment over a stalled airfoil. *AIAA Journal 40*(2), 209–216.

[3] Amitay, M., D. R. Smith, V. Kibens, D. E. Parekh, and A. Glezer (2001). Aerodynamic flow control over an unconventional airfoil using synthetic jet actuators. *AIAA Journal 39*(3), 361–370.

[4] Antonia, R. and S. Rajagopalan (1990). Determination of drag on a circular cylinder. *AIAA Journal 28*(10), 1833–1834.

[5] Becker, R., R. King, R. Petz, and W. Nitsche (2007). Adaptive closed-loop separation control on a high-lift configuration using extremum seeking. *AIAA journal 45*(6), 1382–1392.

[6] Bendat, J. S. and A. G. Piersol (2011). *Random data: analysis and measurement procedures*, Volume 729. John Wiley & Sons.

[7] Benedict, L. and R. Gould (1996). Towards better uncertainty estimates for turbulence statistics. *Experiments in Fluids 22*(2), 129–136.

[8] Bergh, H. and H. Tijdeman (1965). Theoretical and experimental results for the dynamic response of pressure measuring systems. Technical report, Nationaal Lucht- en Ruimtevaartlaboratorium.

[9] Bernardini, C., S. I. Benton, J.-P. Chen, and J. P. Bons (2013). Pulsed jets laminar separation control using instability exploitation. *AIAA journal 52*(1), 104–115.

[10] Bernardini, C., S. I. Benton, K. D. Hipp, and J. P. Bons (2016). Large low-frequency oscillations initiated by flow control on a poststall airfoil. *AIAA Journal 54*(1), 1616–1627.

[11] Boutilier, M. S. and S. Yarusevych (2012a). Effects of end plates and blockage on low-Reynolds-number flows over airfoils. *AIAA journal 50*(7), 1547–1559.

[12] Boutilier, M. S. and S. Yarusevych (2012b). Parametric study of separation and transition characteristics over an airfoil at low Reynolds numbers. *Experiments in fluids 52*(6), 1491–1506.

[13] Boutilier, M. S. and S. Yarusevych (2012c). Separated shear layer transition over an airfoil at a low Reynolds number. *Physics of Fluids 24*(8), 084105.

[14] Brehm, C., A. Gross, and H. F. Fasel (2013). Open-loop flow-control investigation for airfoils at low Reynolds numbers. *AIAA journal 51*(8), 1843–1860.

[15] Brendel, M. and T. J. Mueller (1988). Boundary-layer measurements on an airfoil at low Reynolds numbers. *J. Aircraft 25*(7), 612–617.

[16] Buchmann, N., C. Atkinson, and J. Soria (2013). Influence of ZNMF jet flow control on the spatio-temporal flow structure over a NACA-0015 airfoil. *Experiments in fluids 54*(3), 1–14.

[17] Burattini, P. and R. Antonia (2005). The effect of different X-wire calibration schemes on some turbulence statistics. *Experiments in fluids 38*(1), 80–89.

[18] Burgmann, S. and W. Schröder (2008). Investigation of the vortex induced unsteadiness of a separation bubble via time-resolved and scanning PIV measurements. *Experiments in fluids 45*(4), 675.

[19] Carmichael, B. (1981). *Low Reynolds number airfoil survey.* National Aeronautics and Space Administration, Langley Research Center.

[20] Cattafesta, L. N. and M. Sheplak (2011). Actuators for active flow control. *Annual Review of Fluid Mechanics 43*(1), 247–272.

[21] Damion, J. (1994). Means of dynamic calibration for pressure transducers. *Metrologia 30*(6), 743.

[22] de Luca, L., M. Girfoglio, and G. Coppola (2014). Modeling and experimental validation of the frequency response of synthetic jet actuators. *AIAA journal 52*(8), 1733–1748.

[23] Dovgal, A. V., V. V. Kozlov, and A. Michalke (1994). Laminar boundary layer separation: instability and associated phenomena. *Progress in Aerospace Science 30*, 61–94.

[24] Dovgal, V. and V. V. Kozlov (1983). Influence of acoustic perturbations on the flow structure in a boundary layer with adverse pressure gradient. *Fluid Dynamics 18*, 205–209.

[25] Feero, M. A. (2014). Active control of separation on a low Reynolds number airfoil using synthetic jet actuation. Master's thesis, University of Toronto.

[26] Feero, M. A., S. D. Goodfellow, P. Lavoie, and P. E. Sullivan (2014). Flow reattachment using synthetic jet actuation on a low-Reynolds-number airfoil. *AIAA Journal 53*(7), 2005–2014.

[27] Feero, M. A., P. Lavoie, and P. E. Sullivan (2015a). Effects of wind tunnel model end conditions on low Reynolds number airfoil studies. In *25th Canadian Congress of Applied Mechanics*.

[28] Feero, M. A., P. Lavoie, and P. E. Sullivan (2015b). Influence of cavity shape on synthetic jet performance. *Sensors and Actuators A: Physical 223*, 1–10.

[29] Feero, M. A., P. Lavoie, and P. E. Sullivan (2017a). Apparatus for the dynamic calibration of low-range differential pressure transducers. *AIAA Journal*. Manuscript submitted for publication.

[30] Feero, M. A., P. Lavoie, and P. E. Sullivan (2017b). Effect of relative forcing location on separation control with a synthetic jet. In *10th International Symposium on Turbulence and Shear Flow Phenomena*.

[31] Feero, M. A., P. Lavoie, and P. E. Sullivan (2017c). Influence of synthetic jet location on active control of an airfoil at low Reynolds number. *Experiments in Fluids 58*(8), 99.

[32] Feero, M. A., P. Lavoie, and P. E. Sullivan (2017d). Three-dimensional span effects of high-aspect ratio synthetic jet forcing for separation control on a low Reynolds number airfoil. *Journal of Visualization 20*(1), 45–51.

[33] Fitzgerald, E. J. and T. J. Mueller (1990). Measurements in a separation bubble on an airfoil using laser velocimetry. *AIAA journal 28*(4), 584–592.

[34] Fuertes, F. C., E. Cecchi, J. van Beeck, and C. Schram (2014). An inexpensive and versatile technique for wide frequency range surface pressure measurements: an application for the study of turbulent buffeting of a square cylinder. *Experiments in fluids 55*(1), 1627.

[35] Gallas, Q. (2005). *On the modeling and design of zero-net mass flux actuators*. Ph. D. thesis, University of Florida.

[36] Gallas, Q., R. Holman, T. Nishida, B. Carroll, M. Sheplak, and L. Cattafesta (2003, February). Lumped element modelling of piezoelectric-driven synthetic jet actuators. *AIAA Journal 41*(2), 240–247.

[37] George, W. K., P. D. Beuther, and J. L. Lumley (1978). Processing of random signals. In *Proceedings of the Dynamic Flow Conference 1978 on Dynamic Measurements in Unsteady Flows*, pp. 757–800. Springer.

[38] Glezer, A. (2011). Some aspects of aerodynamic flow control using synthetic-jet actuation. *Philosophical Transactions of the Royal Society A: Mathematical, Physical and Engineering Sciences 369*(1940), 1476–1494.

[39] Glezer, A., M. Amitay, and A. M. Honohan (2005). Aspects of low-and high-frequency actuation for aerodynamic flow control. *AIAA Journal 43*(7), 1501–1511.

[40] Goodfellow, S. D. (2010). Active flow control using synthetic jet actuation. Master's thesis, University of Toronto.

[41] Greenblatt, D., B. Nishri, A. Darabi, and I. Wygnanski (1999). Some factors affecting stall control with particular emphasis on dynamic stall. In *30th Fluid Dynamics Conference*, pp. 3504.

[42] Greenblatt, D., K. B. Paschal, Y. Chung-Sheng, and J. Harris (2006). Experimental investigation of separation control part 2: zero mass-flux oscillatory blowing. *AIAA journal 44*(12), 2831–2845.

[43] Greenblatt, D. and I. Wygnanski (2003). Effect of leading-edge curvature on airfoil separation control. *Journal of Aircraft 40*(3), 473–481.

[44] Greenblatt, D. and I. J. Wygnanski (2000). The control of flow separation by periodic excitation. *Progress in Aerospace Sciences 36*(7), 487–545.

[45] Holman, R., Y. Utturkar, R. Mittal, B. L. Smith, and L. Cattafesta (2005). Formation criterion for synthetic jets. *AIAA journal 43*(10), 2110–2116.

[46] Holmes, J. and R. Lewis (1987). Optimization of dynamic-pressure-measurement systems. i. single point measurements. *Journal of Wind Engineering and Industrial Aerodynamics 25*(3), 249–273.

[47] Hsiao, F.-B., J.-Y. Shyu, and C.-F. Liu (1990). Control of wall-separated flow by internal acoustic excitation. *AIAA Journal 28*(8), 1440–1446.

[48] Hu, H. and Z. Yang (2008). An experimental study of the laminar flow separation on a low-Reynolds-number airfoil. *Journal of Fluids Engineering 130*(5), 051101.

[49] Hultmark, M. and A. J. Smits (2010). Temperature corrections for constant temperature and constant current hot-wire anemometers. *Measurement Science and Technology 21*(10), 105404.

[50] Hunt, J. C., A. A. Wray, and P. Moin (1988). Eddies, streams, and convergence zones in turbulent flows.

[51] Hussain, A. and W. Reynolds (1970). The mechanics of an organized wave in turbulent shear flow. *Journal of Fluid Mechanics 41*(02), 241–258.

[52] Irwin, H., K. Cooper, and R. Girard (1979). Correction of distortion effects caused by tubing systems in measurements of fluctuating pressures. *Journal of Wind Engineering and Industrial Aerodynamics 5*(1-2), 93–107.

[53] Jørgensen, F. E. (2001). *How to measure turbulence with hot-wire anemometers: a practical guide*. Dantec dynamics.

[54] Keane, R. D. and R. J. Adrian (1990). Optimization of particle image velocimeters. i. double pulsed systems. *Measurement science and technology 1*(11), 1202.

[55] Lissaman, P. B. S. (1983). Low-Reynolds-number airfoils. *Annual Review of Fluid Mechanics 15*, 223–239.

[56] Mabe, J. H., F. T. Calkins, B. Wesley, R. Woszidlo, L. Taubert, and I. Wygnanski (2009). Single dielectric barrier discharge plasma actuators for improved airfoil performance. *Journal of Aircraft 46*(3), 847–855.

[57] Marchman, J. (1987). Aerodynamic testing at low Reynolds numbers. *Journal of Aircraft 24*(2), 107–114.

[58] Margalit, S., D. Greenblatt, A. Seifert, and I. Wygnanski (2005). Delta wing stall and roll control using segmented piezoelectric fluidic actuators. *Journal of Aircraft 42*(3), 698–709.

[59] Mueller, T. J. (1985). Low Reynolds number vehicles. Technical report, DTIC Document.

[60] Mueller, T. J. and S. M. Batil (1982). Experimental studies of separation on a two-dimensional airfoil at low Reynolds numbers. *AIAA Journal 20*(4), 457–463.

[61] Naguib, A., S. Gravante, and C. Wark (1996). Extraction of turbulent wall-pressure time-series using an optimal filtering scheme. *Experiments in Fluids 22*(1), 14–22.

[62] Olson, D. A., A. W. Katz, A. M. Naguib, M. M. Koochesfahani, D. P. Rizzetta, and M. R. Visbal (2013). On the challenges in experimental characterization of flow separation over airfoils at low Reynolds number. *Experiments in fluids 54*(2), 1470.

[63] O'Meara, M. and T. Mueller (1987). Laminar separation bubble characteristics on an airfoil at low Reynolds numbers. *AIAA journal 25*(8), 1033–1041.

[64] Packard, N. O., M. P. Thake Jr, C. H. Bonilla, K. Gompertz, and J. P. Bons (2013). Active control of flow separation on a laminar airfoil. *AIAA journal 51*(5), 1032–1041.

[65] Pinier, J. T., J. M. Ausseur, M. N. Glauser, and H. Higuchi (2007). Proportional closed-loop feedback control of flow separation. *AIAA Journal 45*(1), 181–190.

[66] Post, M. L. and T. C. Corke (2004). Separation control on high angle of attack airfoil using plasma actuators. *AIAA journal 42*(11), 2177–2184.

[67] Sahni, O., J. Wood, K. E. Jansen, and M. Amitay (2011). Three-dimensional interactions between a finite-span synthetic jet and a crossflow. *Journal of Fluid Mechanics 671*, 254–287.

[68] Seifert, A., A. Darabi, and I. Wyganski (1996). Delay of airfoil stall by periodic excitation. *Journal of Aircraft 33*(4), 691–698.

[69] Semaan, R. and P. Scholz (2012). Pressure correction schemes and the use of the wiener deconvolution method in pneumatic systems with short tubes. *Experiments in fluids 53*(3), 829–837.

[70] Shuster, J. M. and D. R. Smith (2007). Experimental study of the formation and scaling of a round synthetic jet. *Physics of fluids 19*(4), 045109.

[71] Smith, B. L. and A. Glezer (1998). The formation and evolution of synthetic jets. *Physics of fluids 10*, 2281.

[72] Tavoularis, S. (2005). *Measurement in fluid mechanics*. Cambridge University Press.

[73] Tian, Y., L. Cattafesta, and R. Mittal (2006). Adaptive control of separated flow. In *44th AIAA aerospace Sciences meeting and Exhibit*, pp. 1401.

[74] Timmins, B. H., B. W. Wilson, B. L. Smith, and P. P. Vlachos (2012). A method for automatic estimation of instantaneous local uncertainty in particle image velocimetry measurements. *Experiments in fluids 53*(4), 1133–1147.

[75] Tropea, C., A. L. Yarin, and J. F. Foss (2007). *Springer handbook of experimental fluid mechanics*, Volume 1. Springer Science & Business Media.

[76] Tuck, A. and J. Soria (2008). Separation control on a NACA 0015 airfoil using a 2D micro ZNMF jet. *Aircraft Engineering and Aerospace Technology 80*(2), 175–180.

[77] van Dam, C. P. (1999). Recent experience with different methods of drag prediction. *Progress in Aerospace Sciences 35*(8), 751–798.

[78] van Oudheusden, B. W., F. Scarano, E. W. Roosenboom, E. W. Casimiri, and L. J. Souverein (2007). Evaluation of integral forces and pressure fields from planar velocimetry data for incompressible and compressible flows. *Experiments in Fluids 43*(2-3), 153–162.

[79] Whitmore, S. A. and M. D. Wilson (2011). Wiener deconvolution for reconstruction of pneumatically attenuated pressure signals. *AIAA journal 49*(5), 890–897.

[80] Wilson, B. M. and B. L. Smith (2013). Taylor-series and Monte-Carlo-method uncertainty estimation of the width of a probability distribution based on varying bias and random error. *Measurement Science and Technology 24*(3), 035301.

[81] Wu, J.-Z., X.-Y. Lu, A. G. Denny, M. Fan, and J.-M. Wu (1998). Post-stall flow control on an airfoil by local unsteady forcing. *Journal of Fluid Mechanics 371*(1), 21–58.

[82] Yarusevych, S. (2006). *Investigation of airfoil boundary layer and turbulent wake development at low Reynolds numbers*. Ph. D. thesis, University of Toronto.

[83] Yarusevych, S. and M. Kotsonis (2017). Steady and transient response of a laminar separation bubble to controlled disturbances. *Journal of Fluid Mechanics 813*, 955–990.

[84] Yarusevych, S., P. E. Sullivan, and J. G. Kawall (2006). Coherent structures in an airfoil boundary layer and wake at low Reynolds numbers. *Physics of Fluids 18*(4), 044101.

[85] Yarusevych, S., P. E. Sullivan, and J. G. Kawall (2009). On vortex shedding from an airfoil in low-Reynolds-number flows. *Journal of Fluid Mechanics 632*, 245–271.

[86] Yavuzkurt, S. (1984). A guide to uncertainty analysis of hot-wire data. *ASME Transactions Journal of Fluids Engineering 106*, 181–186.

[87] Zilli, J., D. Sutton, and P. Lavoie (2017). Effect of freestream turbulence on laminar separation bubbles and flow transition on an SD7003 airfoil at low Reynolds numbers. In *55th AIAA Aerospace Sciences Meeting*, pp. 0302.